

A HYBRID HYDROFORMING AND MECHANICAL BONDING
PROCESS FOR FUEL CELL BIPOLAR PLATES

by

Sasawat Mahabunphachai

A dissertation submitted in partial fulfillment
of the requirements for the degree of
Doctor of Philosophy
(Mechanical Engineering)
in The University of Michigan
2008

Doctoral Committee:

Professor Jun Ni, Chair
Professor Elijah Kannatey-Asibu Jr.
Professor Albert J. Shih
Professor Lumin Wang

© Sasawat Mahabunphachai

All rights reserved

2008

To my parents and sister

ACKNOWLEDGEMENTS

I would like to take this opportunity to thank the Royal Thai Government for their continuous financial support during my study in the US. Also, I am very grateful and thankful for having very understanding and encouraging research advisors, Professor Muammer Koç and Professor Jun Ni, to guide me through my Ph.D. study. Without their continuous guidance and encouragements, this research work would not be possible. I would also like to thank all my Ph.D. committee members for their time and feedbacks for this study. Thank to all my friends and staffs at the WuMRC at the University of Michigan and at the CPF at the Virginia Commonwealth University for their morale supports and useful suggestions to my research work. Finally, I would like to thank to my parents and sister for being so patient with me and giving me their best supports throughout the course of my study.

TABLE OF CONTENTS

DEDICATION.....	ii
ACKNOWLEDGEMENTS	iii
LIST OF FIGURES	vii
LIST OF TABLES	xi
CHAPTER 1 : INTRODUCTION.....	1
1.1 Research Motivation and Background.....	1
1.2 Research Objectives.....	10
1.3 Dissertation Organization	13
CHAPTER 2 : STATE OF THE ART REVIEW	15
2.1 Introduction.....	15
2.2 Fuel Cell Technology.....	15
2.3 Background on Microforming	19
2.4 Size Effects in Microforming Processes	22
2.5 Modeling of Size Effects on Flow Stress.....	30
2.6 Microforming Processes	32
2.6.1 Micro-forging.....	32
2.6.2 Micro-embossing/coining	35
2.6.3 Micro-extrusion.....	39
2.6.4 Micro-bending.....	42
2.6.5 Micro-deep Drawing	44
2.6.6 Micro-hydroforming	49
2.7 Pressure Welding	51
2.7.1 Mechanisms of Bond Formation.....	52
2.7.2 Theoretical Models for Calculating Bond Strength	53
2.8 Numerical Modeling of Micro-scale Deformation	58
2.9 Summary and Research Issues.....	61

CHAPTER 3 : INVESTIGATION OF SIZE EFFECTS ON MATERIAL BEHAVIOR OF THIN SHEET METALS USING HYDRAULIC BULGE TESTING.....	64
3.1 Introduction.....	64
3.2 Grain, Specimen, and Feature Size Effects.....	65
3.3 Experimental Setup and Procedure.....	70
3.3.1 Material Preparation.....	70
3.3.2 Hydraulic Bulge Test Setup.....	73
3.3.3 Determination of the Flow Curve.....	76
3.4 Results and Discussion.....	79
3.5 Qualitative Model Explaining the Size Effects.....	87
3.6 Quantitative Model Explaining the Size Effects.....	92
3.7 Summary and Conclusions.....	95
CHAPTER 4 : HYDROFORMING OF MICRO-CHANNEL ARRAYS – PROCESS CHARACTERIAZATION AND CHANNEL DESIGN GUIDELINES	98
4.1 Introduction.....	98
4.2 Experimental Setup.....	100
4.3 Experimental Results and Discussion.....	102
4.4 FE Models and Validation.....	106
4.5 Parametric Study.....	112
4.5.1 Single-channel Hydroforming.....	114
4.5.2 Multi-channel Hydroforming.....	117
4.6 Summary and Conclusions.....	119
CHAPTER 5 : CHARACTERIZATION OF PRESSURE WELDING PROCESS OF THIN SHEET METALS IN COLD AND WARM TEMPERATURE CONDITIONS.....	122
5.1 Introduction.....	122
5.2 Experimental Setup and Procedure.....	127
5.3 Results and Discussion.....	131
5.3.1 Effect of Surface Condition on P_{min} and Bond Strength.....	131
5.3.2 Effect of Material Type and Initial Blank Thickness on P_{min}	132
5.3.3 Effect of Indenter Size on P_{min}	134
5.3.4 Effect of Welding Pressure on Bond Strength.....	134
5.3.5 Effect of Welding Temperature on Bond Strength.....	135
5.3.6 Microstructure of Bond Formation.....	137
5.4 Summary and Conclusions.....	139
CHAPTER 6 : NUMERICAL AND EXPERIMENTAL INVESTIGATIONS OF THE HYBRID MANUFACTURING PROCESS	141
6.1 Introduction.....	141

6.2 Literature Review on Micro-channel and Flow Field Configuration	142
6.3 FE Modeling of the Hybrid Process.....	146
6.3.1 Pressure Welding Criteria.....	147
6.3.2 Material Flow Curves at Elevated Temperatures.....	148
6.3.3 FE Models – 2D Isothermal Simulations.....	154
6.3.4 Hybrid Process Characterization.....	156
6.4 Hybrid Process Development	159
6.5 Summary and Conclusions	164
CHAPTER 7 : CONCLUSIONS AND FUTURE WORK.....	167
7.1 Contributions.....	167
7.2 Recommendation for Future Work.....	175
BIBLIOGRAPHY.....	178

LIST OF FIGURES

Figure 1-1: Cost breakdown for (a) fuel cell sub-system, and (b) fuel cell stack [<i>Garland, 2002</i>]	2
Figure 1-2: Basic structure of a bipolar plate.....	3
Figure 1-3: Single bipolar plate of (a) machined graphite [<i>Graftech Co.</i>], (b) stamped stainless steel sheet [<i>GenCell Corp.</i>], (c) photo etched stainless steel/titanium plate [<i>Tech-etch, Inc.</i>], (d) molded polymer-carbon composite [<i>Middelmann, 2003</i>], and (e) molded carbon-carbon material [<i>Besmann, 2003</i>].....	6
Figure 1-4: Conceptualized hybrid manufacturing process [<i>Koç and Mahabunphachai, 2007</i>]	11
Figure 2-1: Efficiencies of the fuel cell electrical vehicles (FCEV) and the optimized internal combustion engine vehicles (ICEV) as function of vehicle use [<i>Weule, 1995</i>]	16
Figure 2-2: Schematic of a PEMFC operation principle [<i>Tech-etch, Inc.</i>]	16
Figure 2-3: Major differences of fuel cell types	17
Figure 2-4: Stack configuration and components of a typical PEMFC [source: <i>www.power-technology.com</i>]	19
Figure 2-5: A microforming system.....	21
Figure 2-6: Feature size effect observed through tensile testing of thin sheet metals [<i>Kals, 2000; Raulea, 2001</i>].....	23
Figure 2-7: Grain size effect on bending force in bending experiment [<i>Kals, 2000; Raulea, 2001</i>]	24
Figure 2-8: Large variations in the case of single grain deformation [<i>Raulea, 2001</i>]	25
Figure 2-9: Feature size effects in bulk forming [<i>Engel, 2002</i>].....	25
Figure 2-10: Surface layer model in (a) sheet metal [after <i>Kals, 2000</i>], and (b) bulk metal [<i>Geiger, 2001</i>]	26
Figure 2-11: Strain anisotropy of CuNi18Zn20 versus length scale λ [<i>Kals, 2000</i>].....	27
Figure 2-12: Double cup experiment [<i>Geiger, 2001</i>].....	28
Figure 2-13: Effect of open and closed lubricant pockets on friction [<i>Geiger, 2001</i>]	29
Figure 2-14: Relationship between parameters α and β and the n ratio where D is the characteristic length and d is the grain size [<i>Kim, 2007</i>]	32
Figure 2-15: Micro-pyramids and micro-gear forged with Si die [<i>Saotome, 1994</i>]	33
Figure 2-16: Flow stress and standard deviation of flow stress at different temperatures [<i>Engel, 2003</i>].....	34
Figure 2-17: Average hardness gradient (AHG) and universal hardness (HU0.03) [<i>Engel, 2003</i>]	35
Figure 2-18: SEM images of (a) etched Si die, and (b) embossed gratings with groove depth of 2.5 μm [<i>Otto, 2000</i>]	36

Figure 2-19: Silicon die with (a) complex structure, and (b) straight channel structure [Bohm, 2001].....	37
Figure 2-20: Detail of complex structure after cold embossing [Bohm, 2001]	38
Figure 2-21: Embossed straight channel structure with a gap with of 1 μm on Al99.5 sheet with material grain size $> 3 \mu\text{m}$ [Bohm, 2001]	39
Figure 2-22: Forward rod – backward cup extrusion: effect of microstructure [Geiger, 2001; Engel, 2002].....	40
Figure 2-23: Backward can extruded part, SEM picture and cross sectional micrograph [Engel, 2003].....	40
Figure 2-24: A forward-extruded micro-gear shaft – La60Al20Ni10Co5Cu5 amorphous alloy, gear module = 50 μm , number of teeth =10 [Otto, 2000]	41
Figure 2-25: Force-displacement response for extrusion of micropins with different initial grain size [Cao, 2004].....	42
Figure 2-26: Bending forces and yield strength in bending tests [Geiger, 2001]	43
Figure 2-27: Strain distribution from bending experiment: (a) fine grain, and (b) coarse grain [Geiger, 2001].....	44
Figure 2-28: Micro-deep drawing results, $t = 0.1 \text{ mm}$ [Saotome, 2001]	45
Figure 2-29: The ratio $P_{\text{exp}}/P_{\text{cal}}$ for various conditions [Saotome, 2001]	46
Figure 2-30: Micro deep drawing cups drawn with punch diameters from 8 to 1mm [Witulski, 2004].....	47
Figure 2-31: Comparison of macro and micro deep drawing cups [Vollertsen, 2004]	48
Figure 2-32: Comparison of the effects of lubricant [Vollertsen, 2004]	48
Figure 2-33: Friction coefficient value at the flange (μ_1) and die radius (μ_2) with lubricant 2 g/mm^2 [Vollertsen, 2004].....	49
Figure 2-34: Hydroformed micro-channels on ultra thin copper foil [Joo, 2004].....	50
Figure 2-35: Effect of inter channel distance on thickness distribution of the copper foil [Joo, 2004].....	50
Figure 2-36: Applicability of cold pressure welding for different metal combinations [Thomas, 1993]	52
Figure 2-37: Bonding mechanism for scratch-brushed surfaces [Bay, 1986].....	53
Figure 2-38: Contaminant layers combined, fractured as one, and stayed at the interface [Wright, 1978].....	55
Figure 2-39: The possible schemes of the fracture of the surface layers [Lukaschkin, 1996].....	57
Figure 2-40: Schematic of strain rate and spatial size scale effects on computing and the regions where local and non-local continuum theories are applicable [Horstemeyer, 2001].....	60
Figure 3-1: Effect of N on material flow stress under different testing conditions	69
Figure 3-2: Grain vs. specimen size effect on the flow stress as a function of N	69
Figure 3-3: Heat treating process – (a) heating profiles, and (b) heating furnace	71
Figure 3-4: Grain size and N values of SS304 blanks, 51 μm -thick.....	72
Figure 3-5: Grain size variations.....	72
Figure 3-6: Bulge test setup	74
Figure 3-7: Laser measurement system (Keyence LK-G37 laser sensor)	74
Figure 3-8: Repeatability test of the bulge setup and measurement approach	75
Figure 3-9: Schematic diagram of the bulge setup	76

Figure 3-10: Methodology for determination of the material flow curve in hydraulic bulge testing.....	78
Figure 3-11: Bulged samples of SS304 ($t_0 = 51 \mu\text{m}$) for different grain sizes (d) and bulge diameters (D_c).....	80
Figure 3-12: Plots of P vs. h/a for different D_c and d sizes.....	81
Figure 3-13: Equivalent stress-strain plots for different D_c and d sizes – experimental measurements and curve fit using Power law ($\sigma = K\varepsilon^n$).....	81
Figure 3-14: Effect of (a) specimen/grain size (N), and (b) feature/specimen size (M) on material flow stress at two strain levels ($\varepsilon = 0.1$ and 0.3).....	84
Figure 3-15: Comparison of flow stress calculations with and without strain-hardening effect (n) for different M and d sizes at $\varepsilon = 0.2$	86
Figure 3-16: Surface layer model [after <i>Kals, 1996</i>].....	87
Figure 3-17: Section on a bulge sample.....	88
Figure 3-18: Relationships between N and α	89
Figure 3-19: Grain boundary length per unit volume for different N and M combinations.....	92
Figure 3-20: Flow curves comparison between experiment and proposed model.....	93
Figure 3-21: Flow stress comparison between bulge test results [<i>Michel, 2003</i>] and proposed model for different N and M combinations.....	95
Figure 4-1: Micro-feature arrays on thin metallic sheet for PEMFC fabricated by.....	99
Figure 4-2: Hydroforming process apparatus.....	101
Figure 4-3: Die inserts: 1-channel, 3-channel, and 6-channel dies.....	101
Figure 4-4: Laser measurement system (Keyence LK-G37 laser sensor).....	102
Figure 4-5: Samples of hydroformed micro-channels on SS304, 0.051mm-thick. (a) single-channel specimen, (b) 3-channel specimen, and (c) 6-channel specimen.....	103
Figure 4-6: Micro-channel profiles of 1-channel (top), 3-channel (middle), and 6-channel (bottom) specimens.....	105
Figure 4-7: Effect of material grain size on the micro-channel formability.....	106
Figure 4-8: Simulation set up.....	108
Figure 4-9: Simulation results for channel height prediction from different material flow curves and models.....	110
Figure 4-10: A typical channel profile for 3-channel specimens with lower channel height at the center.....	111
Figure 4-11: FEA result comparison using $\sigma = K\varepsilon^n$ with $K = 1,400 \text{ MPa}$ and $n = 0.12$..	112
Figure 4-12: Studied parameters in the FE simulations.....	114
Figure 4-13: Effect of channel width (W) and strain-hardening (n) on maximum aspect ratio (AR).....	115
Figure 4-14: Effect of corner radius (R_d), draft angle (α), and strain-hardening (n) on maximum aspect ratio (AR).....	116
Figure 4-15: Effect of channel spacing (W_{int}) and channel number on the channel height and thickness distribution.....	118
Figure 5-1: Experimental apparatus.....	128
Figure 5-2: Calculation of weld area.....	129
Figure 5-3: Tensile test of bonded specimens under (a) shear, and (b) normal loading .	130
Figure 5-4: Effect of surface conditions on the minimum welding pressure and bond strength under shear loading.....	132

Figure 5-5: Effect of material type and thickness on the minimum welding pressure and its variation.....	133
Figure 5-6: Effect of indenter size on the minimum welding pressure.....	134
Figure 5-7: Effect of welding pressure on the bond strength under normal pull tests....	135
Figure 5-8: Effect of welding temperature on thickness reduction and bond strength...	137
Figure 5-9: Optical microscope images at the bonding sites for (a) Al3003 and (b) Ni201 at room temperature, and SEM images for (c) Ni200 and (d) SS304 at elevated temperature levels	138
Figure 6-1: Different channel shapes	144
Figure 6-2: Selected micro-channel array design of double bipolar plates	146
Figure 6-3: Effect of welding temperature on thickness reduction and bond strength...	148
Figure 6-4: Warm hydraulic bulge testing setup.....	151
Figure 6-5: Schematic diagram of the warm bulge test setup.....	152
Figure 6-6: Typical dome height profiles for different strain rate levels	153
Figure 6-7: Flow curves of thin SS304 sheet (51 μm -thick) at different temperature levels	154
Figure 6-8: FE Models of the hybrid process	155
Figure 6-9: Pressure and velocity profiles	156
Figure 6-10: Axisymmetric model of the hybrid process	157
Figure 6-11: Effects of pressure and die velocity profiles	158
Figure 6-12: Development of hybrid die – setup	159
Figure 6-13: Die assembly	161
Figure 6-14: Die components.....	161
Figure 6-15: Experiment setup.....	162
Figure 6-16: A typical pressure profile used in the test	162
Figure 6-17: (a) hydroformed channels on SS304, 51 μm -thick, and (b) channel profile at 82MPa.....	163

LIST OF TABLES

Table 3-1: Type of size effects and characteristic parameters.....	67
Table 3-2: K and n values for SS304 with $t_0 = 51 \mu\text{m}$	83
Table 3-3: K and n values without considering strain-hardening effect	86
Table 3-4: Calculation of internal grain boundary length per unit volume ($\text{GB}_l/\text{Volume}$)	91
Table 4-1: Micro-channel geometries on different die inserts	102
Table 4-2: Material constants for different flow curves.....	107
Table 4-3: Study cases of single-channel in FEA	114
Table 5-1: Threshold deformation of some metals that can be cold welded [<i>Sowter, 1949;</i> <i>Donelan, 1959; Pendrous, 1984</i>].....	124
Table 5-2: Material properties.....	130
Table 6-1: Optimal channel geometries for maximum hydrogen consumption at anode [<i>Kumar, 2003</i>]	144
Table 6-2: Material properties at elevated temperatures.....	154
Table 6-3: DOE matrix for simulation runs.....	156

CHAPTER 1: INTRODUCTION

1.1 Research Motivation and Background

Despite proven advantages such as high efficiency, quiet operations, and near-zero emissions, fuel cells are not yet cost competitive when compared to the existing power generation technologies, especially in the transportation applications. Compared to internal combustion engines, fuel cell power is 4-10 times more expensive (\$30-\$50/kW vs. \$200-\$300/kW) in its current status. In the stationary power applications, the target cost for competitive fuel cells is an installed cost of less than \$1,500/kW. In the current conditions, the installed cost is above \$5,000/kW. The current cost of fuel cells is a major barrier for commercialization [*Bar-On, 2002; Lipman, 2004*]. Extensive research and development efforts are necessary to address the materials and manufacturing related technical issues to bring the cost of fuel cells down to competitive levels, since around 60-70% of the fuel cell cost is in materials and manufacturing [*Bar-on, 2002; Blunk, 2003; Kumar, 2003; Middelman, 2003; Lipman, 2004*]. A cost breakdown for proton exchange membrane, also known as polymer electrolyte membrane or PEM, fuel cell system is depicted in Figure 1-1.

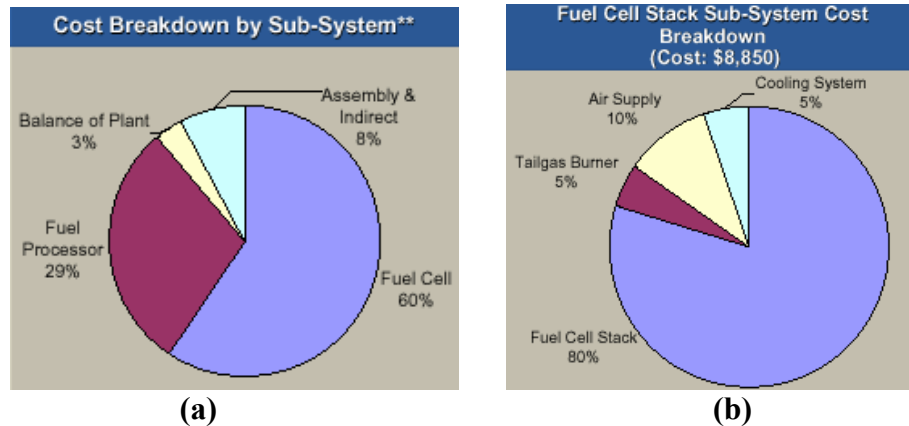


Figure 1-1: Cost breakdown for (a) fuel cell sub-system, and (b) fuel cell stack [Garland, 2002]

Among different components of the fuel cells, the bipolar plates stand as the high weight-, high volume-, and high cost-component (i.e., 60-80% of stack weight and 30-45% of stack cost [Hermann, 2005; Li, 2005]). The bipolar plates have complicated micro-channel arrays in the range of 100-500 micrometers in depth and width on both sides for effective distribution of hydrogen and oxygen gases, and inside cooling channels to sustain the operation temperature within 80-90°C for efficient performance (i.e., 0.6-0.7 Volt/cell), Figure 1-2. The bipolar plates have also stringent requirements for electrical conductivity, corrosion resistance, weight, thickness, handling, etc.. Therefore, the material selection and manufacturing method of the bipolar plates are important research and development issues to achieve high power density at reduced cost. The functions of the bipolar plates include:

- (a) distribute the reactants in the cell package,
- (b) remove the by-product water and residual gases from the cell package,
- (c) conduct of electrons to support electrochemical reaction, and
- (d) transfer heat from the cell package.

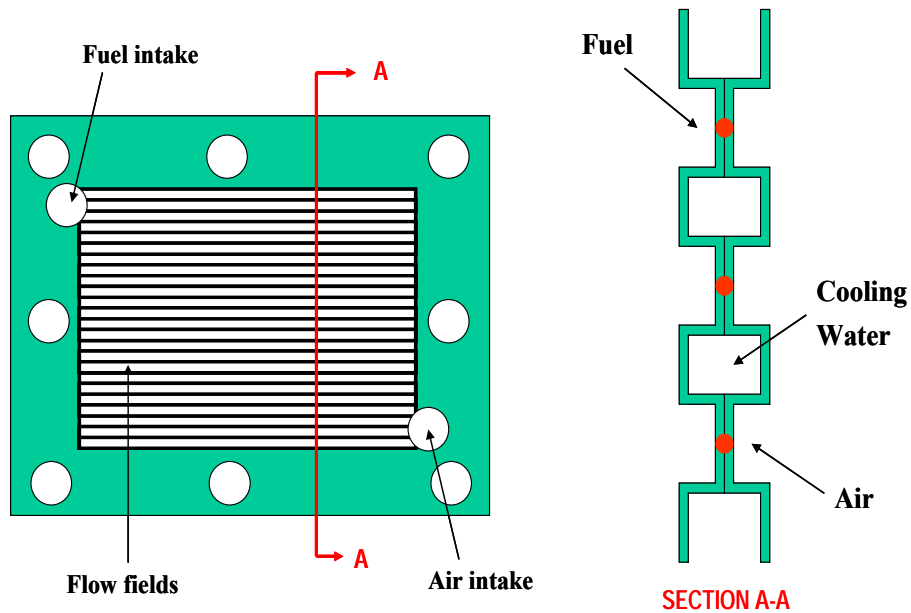


Figure 1-2: Basic structure of a bipolar plate

In addition, the bipolar plate needs to meet the following requirements [*DOE Goals by 2010*]:

- (1) Thin (< 1 mm),
- (2) Light-weight (< 1 kg/kW),
- (3) High corrosion resistance ($< 1 \mu\text{A}/\text{cm}^2$),
- (4) Channels inside for cooling water passage,
- (5) Channels on both sides for H_2 and O_2 distribution (flow fields),
- (6) Low gas permeability ($< 2 \times 10^{-6} \text{ cm}^3/\text{s}\cdot\text{cm}^2$),
- (7) Low electrical resistance (ohmic loss $< 10 \text{ m}\Omega\cdot\text{cm}^2$),
- (8) High heat conductivity (small temperature gradient),
- (9) Tough (> 4 MPa) and flexible (3-5% deflection at mid-span) to reduce handling damage,
- (10) Durable (good electrochemical stability, min. 5,000 hours for automotive use),

(11) Low cost (\$6/kW), and

(12) High dimensional accuracy (plate to plate and within the plate variation) for uniform contact resistance to enhance fuel cell performance.

All of these operational and functional requirements make the cost-effective design and manufacturing of bipolar plates a challenging research topic in addition to other research issues in fuel cells such as membrane, coating, catalyst, sealing, etc. developments. The selection of material and geometry, and the development of fabrication methods for bipolar plates are ongoing research activities at various institutes and companies worldwide.

In the past few years, the material selection and fabrication methods for the bipolar plates in proton exchange membrane fuel cells (PEMFCs) for vehicle applications have gradually evolved and narrowed to the following candidates:

(1) machined graphite plates [*Scholta, 1999; Mehta, 2003*],

(2) stamped or photo etched metal plates with and without coatings, [*Allen, 2000; Blunk, 2003; Wang, 2003*]

(3) molded polymer-carbon composite – a GM proprietary technology [*Blunk, 2003*], and

(4) molded carbon-carbon material – developed at Oak Ridge National Lab and licensed to Porvair [*Butcher, 2002; Bessman, 2003*].

Samples of different types of bipolar plates are shown in Figure 1-3. Graphite bipolar plates have been the choice of earlier pilot applications and tests because of the excellent chemical stability of graphite to survive in the fuel cell environment and the excellent electrical conductivity to minimize the ohmic loss due to the contact resistance.

However, because of (a) high material and manufacturing (machining) costs, (b) poor mechanical properties (low strength and flexibility), and (c) high porosity levels (leading to high permeability), the commercial use of graphite materials in fuel cells is found to be impractical in their current status of processing, manufacturing and use [*Scholta, 1999; Mehta, 2003; Middelman, 2003; Cunningham, 2006; Jayakumar, 2006*]. Metallic and composite bipolar plates, on the other hand, offer several advantages over the conventional graphite plates; thus they found to be viable alternative options in PEMFCs [*Abdelhamid, 2002; Wind, 2002; Besmann, 2003; Wang, 2003; Cunningham, 2006*]. The cost of bipolar plates is estimated to be only 15-30% of the stack cost with the use of metal or composite bipolar plates as compared to 60-70% with the use of graphite bipolar plates [*Cho, 2004*].

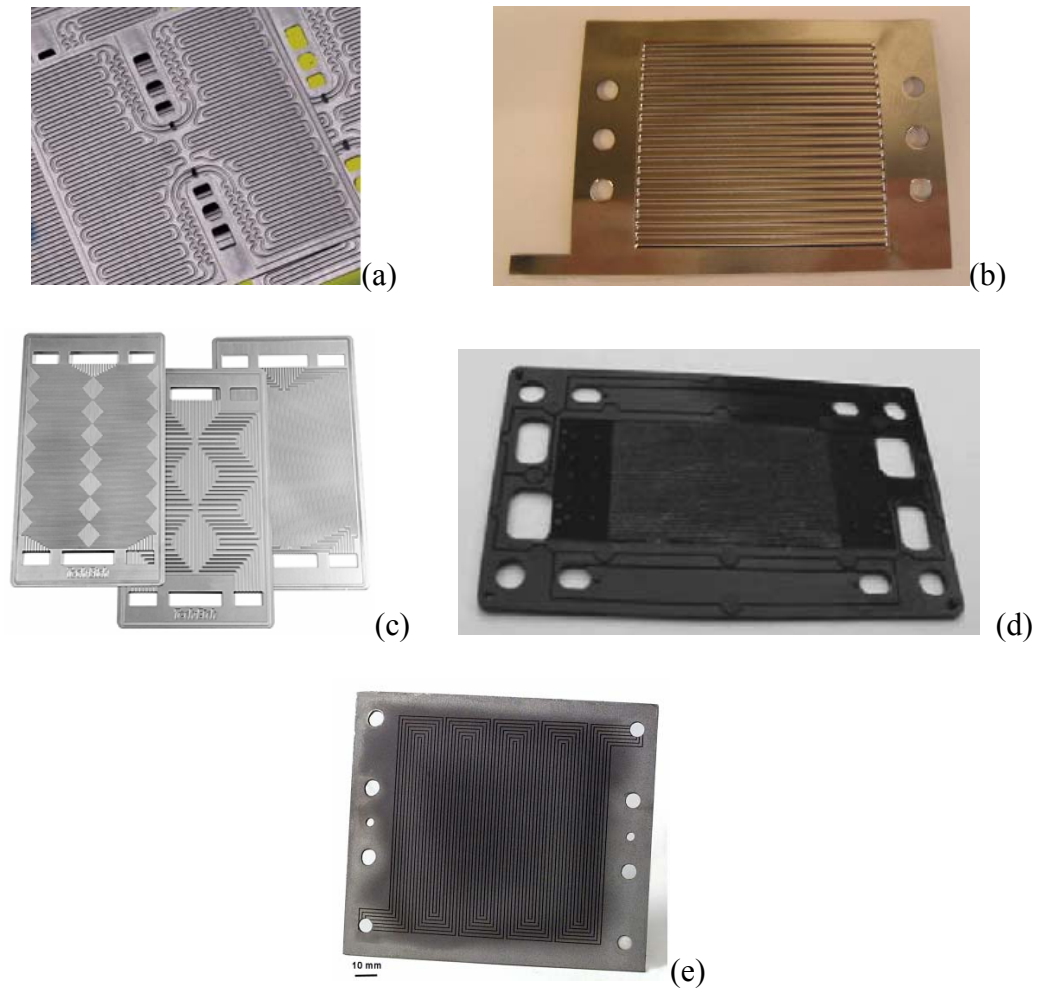


Figure 1-3: Single bipolar plate of (a) machined graphite [Graftech Co.], (b) stamped stainless steel sheet [GenCell Corp.], (c) photo etched stainless steel/titanium plate [Tech-etch, Inc.], (d) molded polymer-carbon composite [Middelman, 2003], and (e) molded carbon-carbon material [Besmann, 2003]

Polymer-graphite composite bipolar plates, generally composed of resins (thermoplastic or thermosetting polymer) and fillers (graphite), with or without fiber reinforcement, have been demonstrated in many studies to provide a similar performance to the traditional graphite plates (e.g., high corrosion resistance, low contact resistance, and lightweight) with several advantages in terms of low material and manufacturing (molding) costs, more freedom in flow-field design, and short cycle-time (10 seconds) for mass production [Middelman, 2003; Cho, 2004; Oh, 2004]. However, one major

drawback of this technology comes from the low electrical conductivity of the polymer resins. Various research efforts were performed to increase the bulk conductivity of this type of bipolar plates to meet the target of 100 S/cm [DOE goal by 2010]. These efforts to increase the electrical conductivity include the alignment process, the use of conductive-tier layer (CTL) method [Blunk, 2003], the variation of the graphite content and powder size [Kuan, 2004], the use of metal plate as the base of the polymer-graphite composite (developed at Los Alamos National Laboratory) [Hermann, 2005], and the use of metal coating [Oh, 2004]. Another issue concerning the composite bipolar plates is the low stack volumetric power density which is limited by the plate thickness that cannot be reduced below 1 mm by compression molding process (current composite plates are around 2-3 mm-thick). In addition, it is very difficult to obtain accurate dimensions of the final plates from the molding process, and these dimensional variations in turn inevitably degrade the overall performance of the fuel cell stack. Injection molding was proposed for better dimensional accuracy and short cycle time, but this technique has a higher mold wear and a limitation on the maximum thickness [Middelman, 2003]. There are also concerns about the decrease in strength and stiffness of the polymer composite plates when operating at elevated temperature levels inside the PEMFCs [Cunningham, 2006]. Depending on the type of composites, the cost of these plates has been reported to be between \$5.4-\$40/kW [Middelman, 2003; Oh, 2004] or \$2.7-\$13.5/kg [Heinzel, 2004], and the initial and long-term operation performance was shown to be comparable to that of the graphite plates [Cho, 2004; Oh, 2004].

Carbon/carbon composite bipolar plates, developed at Oak Ridge National Lab [Besmann, 2003], are reported to have high electrical conductivity, high strength, lightweight, and low permeability. These plates are produced by slurry molding of carbon fibers into preform structures, molding features into a green body, and using chemical vapor infiltration (CVI) to strengthen the composite material, increase the conductivity, and densify the surface to make it impermeable. However, the complexity and the cost of the CVI process make this option inappropriate for the mass production [Middelman, 2003; Cunningham, 2006].

In the recent years, metallic (mostly stainless steel) bipolar plates have received considerable attention because of their low-cost, excellent mechanical, electrical, and thermal properties, and good manufacturability. Existing manufacturing methods of the metallic bipolar plates include stamping of stainless steel sheets as shown in Figure 1-3b, and photo etching of stainless steel or titanium plates as shown in Figure 1-3c. However, the stainless steel bipolar plates are prone to corrosion and dissolution in the hazardous environment inside of the fuel cell which may lead to a possibility of metal ions damaging the membrane electrode assembly (MEA) [Hermann, 2005; Cunningham, 2006]. Therefore, a thin layer of coating is necessary to achieve the corrosion resistance target and to extend the fuel cell life [Allen, 2000; Wind, 2002; Gladczuk, 2003; Li, 2003; Cunningham, 2006]. Gold coating on SS316L plates has been demonstrated to provide similar performance to the graphite plates [Wind, 2002]. Thermal expansion of the base metals and the coating should be selected to be as close to each other as possible to avoid the formation of micro-pores/cracks. In addition, the coating should be applied in a defect-free fashion to avoid the original problem of membrane poisoning [Hermann,

2005]. Recently, Brady et al. has developed a preferential thermal nitridation process to form pinhole free CrN/Cr₂N coating on Ni-Cr alloy [Brady, 2006]. Another vital issue is the interfacial contact resistance (ohmic losses) between the metallic bipolar plate and the carbon paper [Lai, 2004]. This resistance is increased due to the formation of the passive film that reduces the overall power output. The formation of these films varies depending on the elemental composition of the stainless steel alloy. The chromium content is also found to have a favorable influence on the anodic behavior [Bar-on, 2002; Cunningham, 2002; Metha, 2003; Wang, 2003].

Up to date, metallic and composite bipolar plates are the two competing technologies for the commercialization of the PEMFCs in the near future with the polymer composite bipolar plates showing a slight potential edge over the metal plates due to the fact that some of the composite plates are now available in the market [Hermann, 2005]. However, with the advancement in the surface coating technologies and suitable coating materials, metallic bipolar plates are expected to outperform the composite bipolar plates in the future because of their superior electrical and mechanical properties, leading to higher power efficiency, density, and durability. In this study, a novel manufacturing process is proposed as an alternative fabrication method of the metallic bipolar plates using initially flat thin stainless steel 304 sheets. The proposed process combined hydroforming of micro-channels with in-die mechanical bonding process to create double bipolar plates in one-step and one-die operation. The details of the hybrid process are presented in the following section.

1.2 Research Objectives

The objective of this research is to develop an innovative manufacturing process to further increase the volumetric power density and reduce the material and manufacturing cost of bipolar plates in a single step and single die operation using hydroforming of thin sheet metal blanks combined with mechanical joining to form micro-channels on both sides and mechanically join them at various contact spots to create internal cooling channels. Such combined use of hydraulic forming loads and in-process mechanical joining will:

- (a) enable integrated forming of micro-channels on both surfaces (as anode and cathode) and at the middle (as cooling channels),
 - (b) reduce the process steps,
 - (c) reduce variation in dimensional tolerances and surface finish,
 - (d) increase the product quality,
 - (e) increase the performance of fuel cells by ensuring consistent contact resistance,
- and
- (f) reduce the overall stack cost.

The hybrid process is depicted in Figure 1-4, and can be explained as follows: two sheet metal blanks are placed between the upper and lower die halves, which have the intricate shape of micro-channels to be imprinted on the blanks. The dies are pushed against each other at the edges (i.e., periphery) of the sheet metal to provide sealing. Then, high pressure fluid is supplied between the blanks. The internal pressure forces the blanks to deform into the shape of the dies. Once the forming into complex micro-channels is completed or near completed, the upper and lower dies are further pressed

against each other to generate a mechanical joint between two contacting surfaces of the sheet blanks to form the final shape of the bipolar plate. Finished bipolar plates with precisely formed internal cooling channels as well as micro-channels on anode and cathode sides would not only reduce the assembly operations, but also make the handling of the plates during assembly easier and safer, and lead to much less variation.

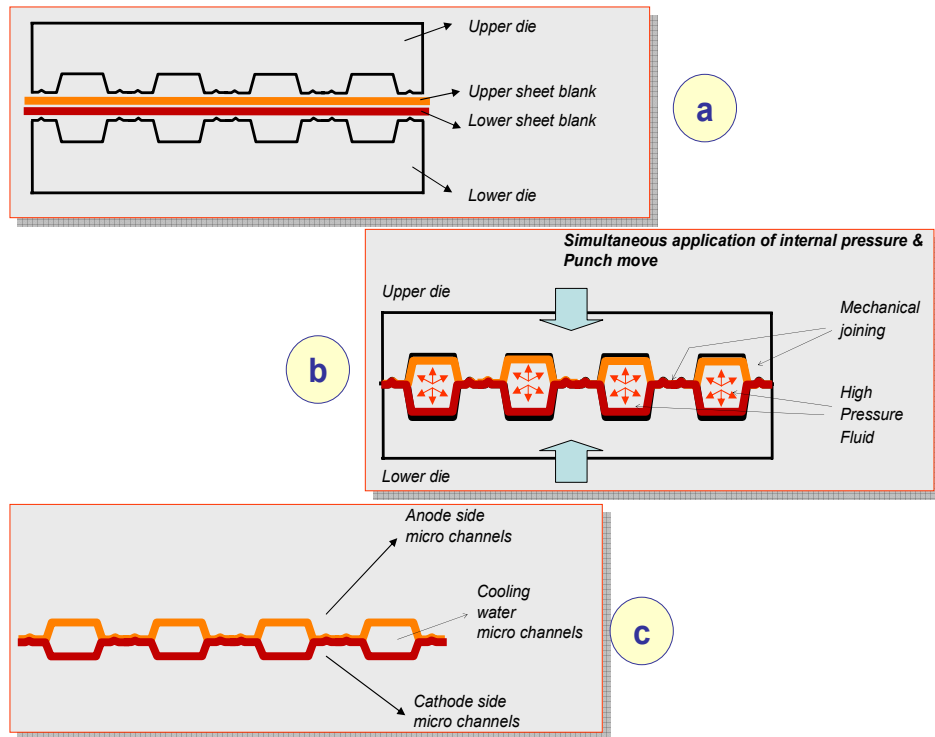


Figure 1-4: Conceptualized hybrid manufacturing process [Koç and Mahabunphachai, 2007]

In contrast to the existing methods of bipolar plate manufacturing, the novel hybrid process proposed in this study is expected to result in thin, lightweight, flexible bipolar plates with internal cooling channels, and flow fields (micro-channels) net-shape formed on both sides (anode and cathode) in one step and one die operation, eliminating handling, separate welding, assembly and sealing processes. Thus, the dimensional tolerance and contact resistance will be improved leading to superior performance due to

reduced variations in eventual assembly of the stacks and consistent contact resistance properties. Efficient material utilization can also be achieved with this manufacturing technique. Total thickness of the bipolar plates in the existing methods can go up to 4 mm. Using this technique, thin blank sheet materials can be formed into integrated bipolar plates with a total thickness of less than 1 mm. As a result, it will be possible to improve the power density up to the required levels of 1 kW/kg [*DOE goal 2010*], while reducing the stack cost and increasing the service life. The closest technology to the proposed one has been developed by Allen et al. [*Allen, 2000; Allen, 2004*], where additional stamping steps are taken to form channels at both sides and middle as explained in their various publications and patents.

In order to accurately design, develop, and validate the conceptualized novel hybrid process, the following scientific challenges are identified for in-depth investigations:

- (1) Understanding of the miniaturization effects on material behavior of thin sheet metals at the micro-levels (i.e., “size effects” on material response),
- (2) Understanding of the deformation mechanics involved in the forming of micro-scale features (channels, grooves) under complex loading conditions such as the one in hydroforming,
- (3) Understanding of the micro-mechanical bonding/joining that will be created during the proposed method and its characterization (i.e., effect of process conditions on the bond quality),
- (4) Understanding of the effects of micro-channel geometries on the channel formability and design limitations from the manufacturability perspective, and

(5) Development of predictive process models using an FEA tool for evaluation of producibility and effect of process parameters and their synchronization on the manufacturability incorporating the size effects on material modeling, the design of the micro-channel arrays, and the bonding criteria, etc..

1.3 Dissertation Organization

The remainder of this dissertation is divided into seven chapters. Chapter 2 presents a review of the state of the art for fuel cell technology, size effects in microforming processes, numerical tools/analyses for microforming processes, and pressure welding technologies of metal alloys. Chapter 3 introduces a material characterization study of thin sheet metals under hydraulic bulge testing conditions, focusing on the size effects (grain vs. feature sizes) on the material response. A systematic approach for determining the flow curve of thin sheet metals in bulge testing is discussed and proposed. New material models are qualitatively and quantitatively developed to explain the changes in the material flow curve caused by the size effects. In Chapter 4, micro-channel hydroforming experiments using thin sheet of stainless steel 304 are performed. Both material grain size and feature (channel) size effects on the micro-channel formability are investigated. FE models of the micro-channel hydroforming process are developed, validated, and used to conduct a parametric study to establish design guidelines for the micro-channels. Chapter 5 presents experimental investigations of different effects of material and process parameter on the minimum welding pressure and the bond quality in pressure welding of thin sheet metals in both cold and warm conditions. The mechanisms of the bond formation are also studied using microstructure analyses. In Chapter 6, FE models of the hybrid process are

developed based on the understanding and findings in the previous chapters to include the size effects on the material behavior, the suggested micro-channel design from the parametric study, and the required process conditions to bond thin blanks of stainless steel. The FE models are used to study the process producibility and effect of process parameters (i.e., forming pressure and punch stroke/speed) on the manufacturability. The development of the hybrid process in a single-die and single-step operation is also discussed at the end of this chapter, showing promising results. Finally, research summary and scientific contributions of this study are presented in Chapter 7 along with suggested future work.

CHAPTER 2: STATE OF THE ART REVIEW

2.1 Introduction

A state of the art review is presented in this chapter on different technologies that are relevant to the development of the proposed manufacturing process of the fuel cell bipolar plates as discussed in the previous chapter. The survey provides background on fuel cells and microforming technologies as well as discusses the so-called “size effects” on the material behavior in different microforming processes. Results from previous research attempts in scaling down the well established forming technology from conventional scale to micro-scale are also presented. A review of pressure welding technologies is also included to better understand the joining mechanisms and the expected weld quality.

2.2 Fuel Cell Technology

A fuel cell is an electrochemical device in which the energy of a chemical reaction is converted directly into electricity. Oxygen from the air and hydrogen fuel, which can be obtained from fuels such as natural gas, methanol, or petroleum, electrochemically combine in the fuel cell to produce electricity. Since the fuel is converted directly to

electricity, the efficiency at which a fuel cell converts hydrogen into electricity is higher than internal combustion engines, extracting more electricity from the same amount of fuel, Figure 2-1. As long as a fuel cell is supplied with hydrogen and oxygen, it will continuously generate electricity. The fuel cell itself has no moving parts - making it a quiet and reliable source of power. Heat and pure water vapor are the only by-products from the fuel cells electrochemical reaction, Figure 2-2.

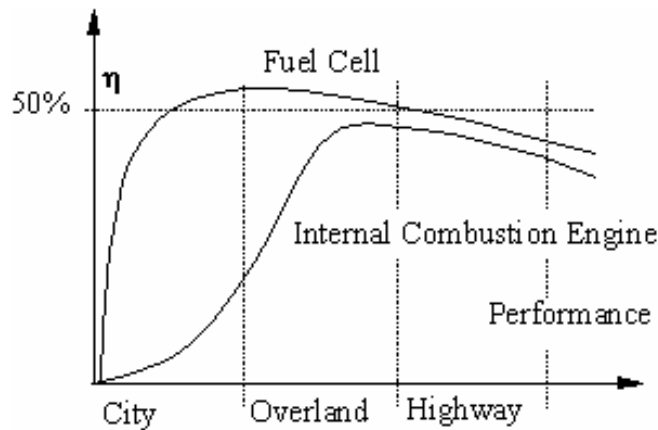


Figure 2-1: Efficiencies of the fuel cell electrical vehicles (FCEV) and the optimized internal combustion engine vehicles (ICEV) as function of vehicle use [Weule, 1995]

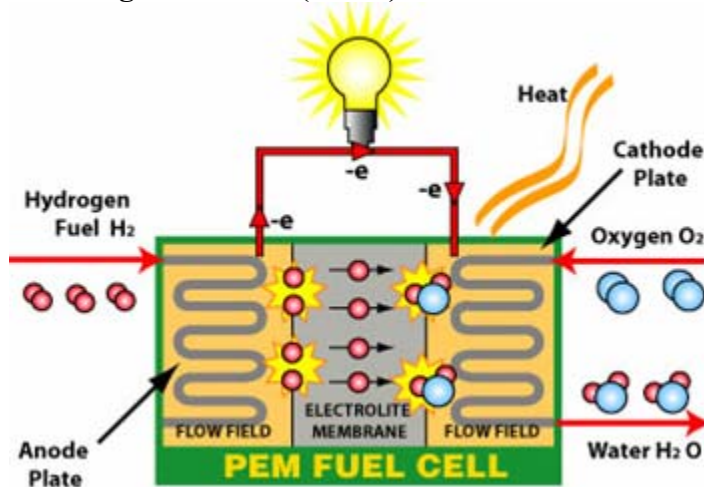


Figure 2-2: Schematic of a PEMFC operation principle [Tech-etch, Inc.]

Five main categories of fuel cells, classified by the type of the electrolyte, are listed in the order of their operating temperature as follows:

- 1) Proton exchange membrane or polymer electrolyte fuel cell (PEMFC, PEFC),
- 2) Alkaline fuel cell (AFC),
- 3) Phosphoric acid fuel cell (PAFC),
- 4) Molten carbonate fuel cell (MCFC), and
- 5) Solid oxide fuel cell (SOFC).

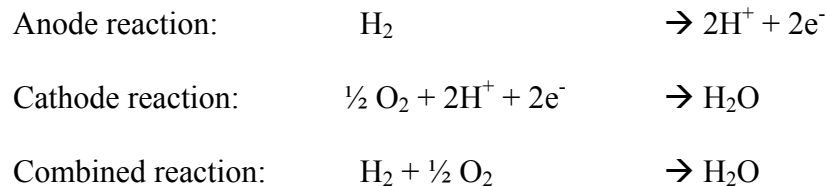
PEMFC and SOFC use a solid phase membrane as the cell separator and electrolyte, while the other three are liquid electrolytes. The solid membrane is less complex than other types of fuel cell systems in terms of sealing, assembly, and handling. A summary of the major differences of fuel cell types is given in Figure 2-3.

	PEMFC	AFC	PAFC	MCFC	SOFC
Operating Temperature	60-100°C	65-260°C	150-210°C	600-1000°C	600-1000°C
Electrolyte	Ion Exchange Membranes	Mobilized or Immobilized Potassium Hydroxide	Immobilized Liquid Phosphoric Acid	Immobilized Liquid Molten Carbonate	Ceramic
Charge Carrier	H ⁺	OH ⁻	H ⁺	CO ₃ ⁻²	O ⁻²
External Reformer for CH ₄	Yes	Yes	Yes	No	No
Catalyst	Platinum	Platinum	Platinum	Nickel	Perovskites
Prime Cell Components	Carbon-based	Carbon-based	Graphite-based	Stainless-based	Ceramic
Product Water Management	Evaporative	Evaporative	Evaporative	Gaseous Product	Gaseous Product
Gaseous/Liquid Water formation	Cathode	Anode	Cathode	Anode	Anode
Fuel	Pure H ₂ (tolerates CO ₂)	Pure H ₂	Pure H ₂ (tolerates CO ₂ , 1.5% CO)	H ₂ , CO, CH ₄ , other hydrocarbons (tolerates CO ₂)	H ₂ , CO, CH ₄ , other hydrocarbons (tolerates CO ₂)
Electrical Efficiency	25-35%	32-60%	35-45%	40-60%	45-65%

Figure 2-3: Major differences of fuel cell types

Since PEMFCs operate at relatively low temperatures (80°C) and can vary their output quickly to meet shifts in power demand, they are suited in transportation applications for quick startups. PEMFCs can also be used in light-duty vehicles, buildings, and much smaller applications such as replacements for rechargeable batteries.

The critical component of the PEMFC consists of two electrodes, the anode and the cathode, separated by a polymer membrane electrolyte as depicted in Figure 2-4. Each of the electrodes is coated on one side with a thin catalyst layer. The electrodes, catalyst and membrane together form the membrane electrode assembly (MEA). A single fuel cell consists of a membrane electrode assembly and two flow field plates. Single cells are combined into a fuel cell stack to produce the desired level of electrical power. Gases (hydrogen and air) are supplied to the electrodes on either side of the PEM through channels formed in the flow field plates. Hydrogen flows through the channels to the anode where the catalyst promotes its separation into protons (positive hydrogen ions) and electrons. The protons migrate through the membrane electrolyte to the cathode. The free electrons are captured as useful electricity through an external circuit, and combine with the protons and oxygen to produce water vapor on the cathode side. On the opposite side of the PEM, oxygen from air flows through the channels to the cathode where it attracts the hydrogen protons through the PEM. In this type of fuel cell, the PEM electrolyte must allow hydrogen protons to pass through, but prohibit the passage of electrons and heavier gases. The chemical reactions for PEMFC are summarized as follow:



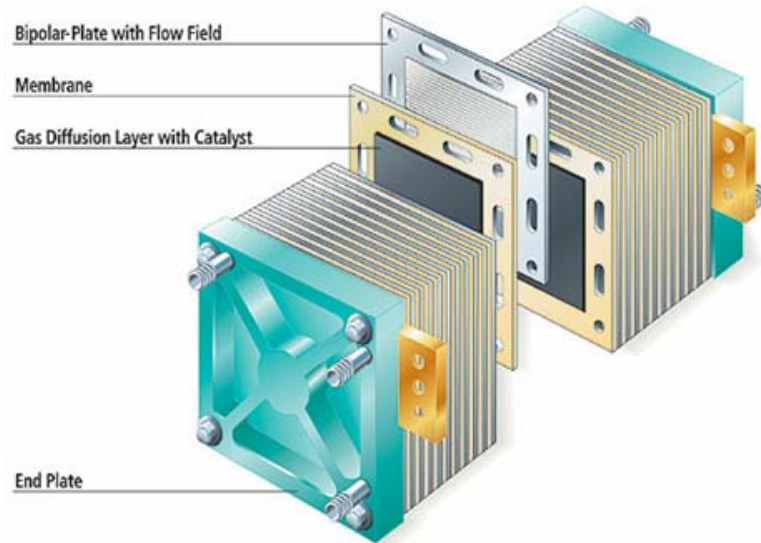


Figure 2-4: Stack configuration and components of a typical PEMFC
 [source: www.power-technology.com]

One of the major features of the bipolar plates is the micro-channels/grooves. Microforming technology has a great potential for manufacturing of these micro-channels/grooves considering its process simplicity and high production rate. A state of the art review on microforming technology is given in the following section.

2.3 Background on Microforming

Microforming is defined as the production of metallic parts by forming with at least two part dimensions in the sub-millimeter range [Geiger, 2001]. When a forming process is scaled down from conventional scale to the sub-millimeter range, some aspects of the workpiece remain unchanged, such as the microstructure and the surface topology. This causes the ratio between the dimensions of the part and parameters of the microstructure or surface to change, and is commonly referred to as the “size effects.”

The trend toward further miniaturization, in particular in the field of electronics,

consumer products, energy generation and storage, medical devices, and micro systems technology (MST), will persist as long as consumers still seek for compact devices with heavily integrated functions. Metal forming processes are well known for their high production rate, minimized material waste, near-net-shapes, excellent mechanical properties, and close tolerances. These advantages make the metal forming suitable for manufacturing of micro features, especially where a high volume-low cost production is desired [Engel, 2002; Vollertsen, 2004]. However, the well established metal forming technology at macro-scale cannot be simply applied in the micro-levels due to the so-called “size-effects” on the material behavior. At the micro level, the processes are characterized by only a few grains located in the deformed area; thus, the material can no longer be considered as a homogeneous continuum. Instead, the material flow is controlled by individual grains, respectively by their size and orientation [Engel, 2003]. As a result, conventional material properties are no longer valid for accurate analysis at this level. Furthermore, the deformation mechanism changes abruptly with large variations in the response of material as the ratio of grain size to the feature size decreases. Surface interaction and friction force become more prominent as the ratio of the surface area to volume increases [Tiesler, 2000; Vollertsen, 2004]. These issues must be addressed as we try to understand the “size effects.” In addition, the forming process is coupled with the material behavior; and thus, will also be influenced as we attempt to scale down the part dimensions. Some additional size effects concerning the forming process are forming forces, spring-back, friction, and scatter of the results.

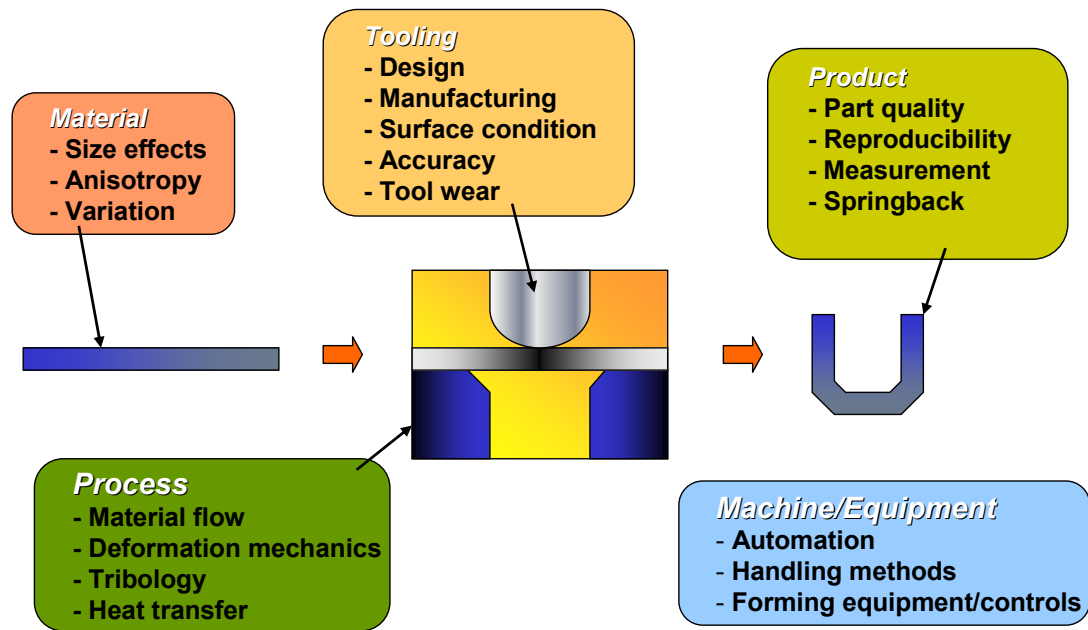


Figure 2-5: A microforming system

A microforming system is comprised of five major categories: material, process, tooling, machine/equipment, and product, Figure 2-5. In all these areas, the effect of size is the dominant factor. Another problem lies in the design and manufacturing of the tools (i.e., dies, inner molds). Small and complex geometries needed for the tools are difficult to achieve, especially when close tolerances and an adequate surface quality are desired. Special tool manufacturing techniques are required to overcome these difficulties. Carefully selected tool material and simple shaped/modular tools can help reduce the cost of tool making and the degree of difficulty regarding the tool manufacturing, and increase the tool life.

One challenge for micro-machines is the required precision at a high speed production. In general, positioning of the micro-parts during the production process requires an accuracy of a few micrometers to sub-micrometers, depending on the part type and ultimate use. In addition, since the part size is extremely small and the part

weight is too low, handling and holding of micro-parts becomes very difficult due to adhesive forces (van der Waals, electrostatic, and surface tension). Therefore, special handling and work holding equipment need to be developed to overcome these difficulties in placing, positioning, and assembly of the micro-parts. Also, the clearance or backlash, between die and punch that could be negligible at the conventional scale, can be a problem when the total required stroke to form the micro-part and clearance lie in the range of a few hundred micrometers [Geiger, 2001]. Another challenge concerns an accurate monitoring system of the process parameters during the forming process and a special measuring and inspecting technique of the final micro-parts. Automation systems at the micro-levels are another challenge that will eventually need to be studied and developed for the high volume-low cost production process.

2.4 Size Effects in Microforming Processes

In general, size effects (i.e., ratio of grain size to the characteristic part size) concern in particular the material behavior and surface interaction, which are relevant for all forming processes. Based on the *similarity theory* proposed by Geiger et al. [Geiger, 1997], when all dimensions of the specimen and tools are multiplied by a geometrical scale factor λ , and the time scale is fixed to one, the strain, strain rate, and strain distribution will be scaled down by the same scale factor λ . Postulating the similarity theory in elastic and plastic material behavior, stress and stress distribution should also be size invariant, that is, the same stress and strain curve should be obtained for different values of the geometrical scaling factor λ . Nevertheless, while this theory may be able to apply to the scaling-down of the process and tooling design at the macro-scale, a

number of material tests and forming experiments at the micro-level have shown the deviation in the material response (i.e., material flow stress, hardness, etc.), which violates the similarity theory. In the area of micro-scale sheet metal forming, as the material sheet thickness is reduced, a decrease in the flow stress has been observed through tensile tests on different materials such as CuAl alloy [Miyazaki, 1979], CuNi18Zn20 and CuZn15 [Kals, 2000], CuZn36 [Michel, 2003], and aluminum [Raulea, 2001], Figure 2-6. A few attempts were also carried out to investigate the effect of the specimen width on the material flow curve using the tensile test, but no significant effect has been reported [Michel, 2003; Tseng, 1990].

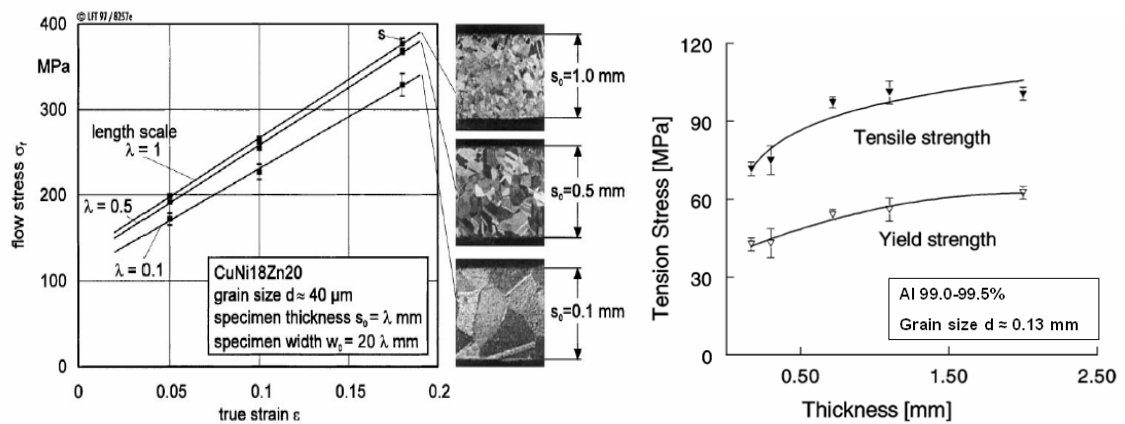


Figure 2-6: Feature size effect observed through tensile testing of thin sheet metals [Kals, 2000; Raulea, 2001]

On the other hand, an increase in the flow stress is observed when the average grain size is reduced. This result agrees with the widely accepted Hall-Petch equation which simply states that materials strengthen as the grain size decreases. However, Raulea et al. [Raulea, 2001] have pointed out that when the grain size is reduced closely to the thickness of the sheet (single grain deformation), an inverse relation between the flow stress and the grain size is observed (i.e., flow stress increases when grain size

becomes larger). This inverse relation was also reported by Kals and Eckstein in 2000, as illustrated in Figure 2-7.

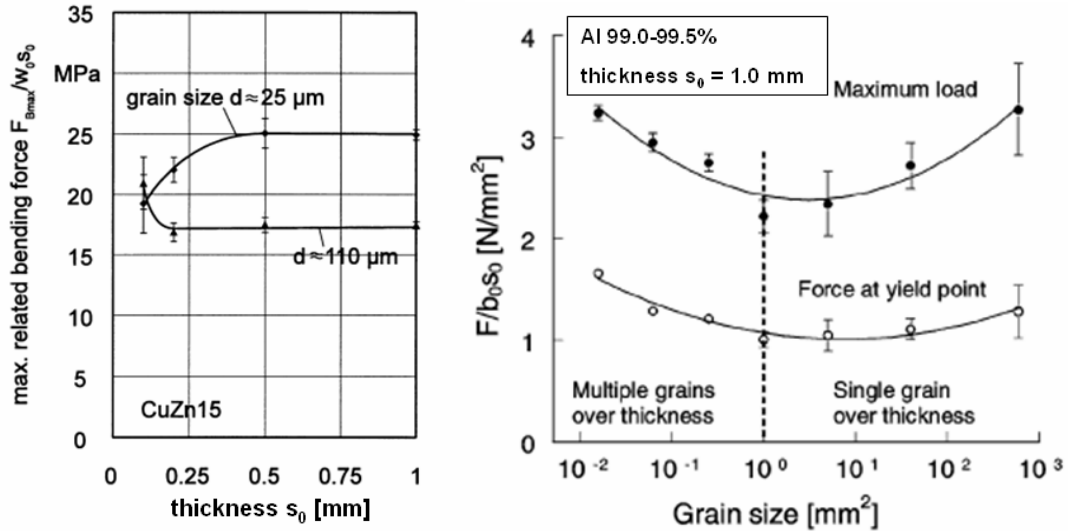


Figure 2-7: Grain size effect on bending force in bending experiment [Kals, 2000; Raulea, 2001]

Another grain size effect in the case of single grain over thickness was reported on the decrease in the repeatability of the test because the behavior of a single grain strongly depends on its orientation. This, in return, leads to the anisotropic deformation and causes large variations. Bad scattering of data is observed (Figure 2-8) when the ratio between the sheet thickness to the grain size, ϕ , is smaller than 1. In the field of bulk metal forming, upsetting tests using copper, CuZn15, and CuSn6 also showed the similar trend, that is, the flow stress decreases with increased miniaturization [Engel, 2002]. Experimental results from the upsetting test of CuZn15 round billets are shown in Figure 2-9.

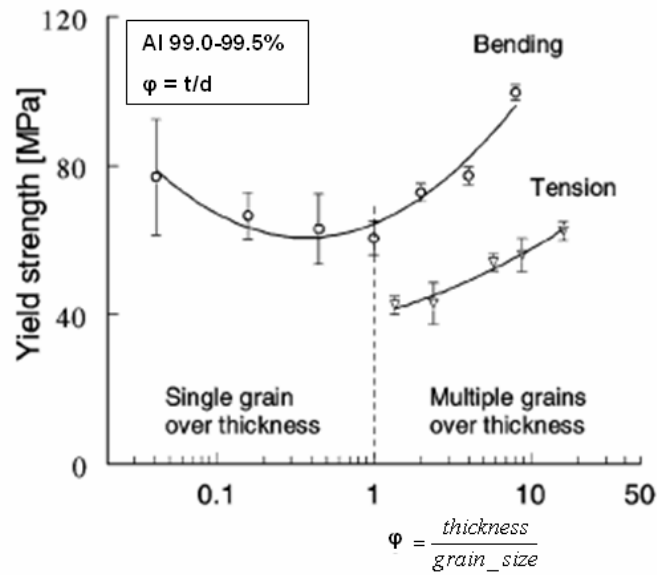


Figure 2-8: Large variations in the case of single grain deformation [Raulea, 2001]

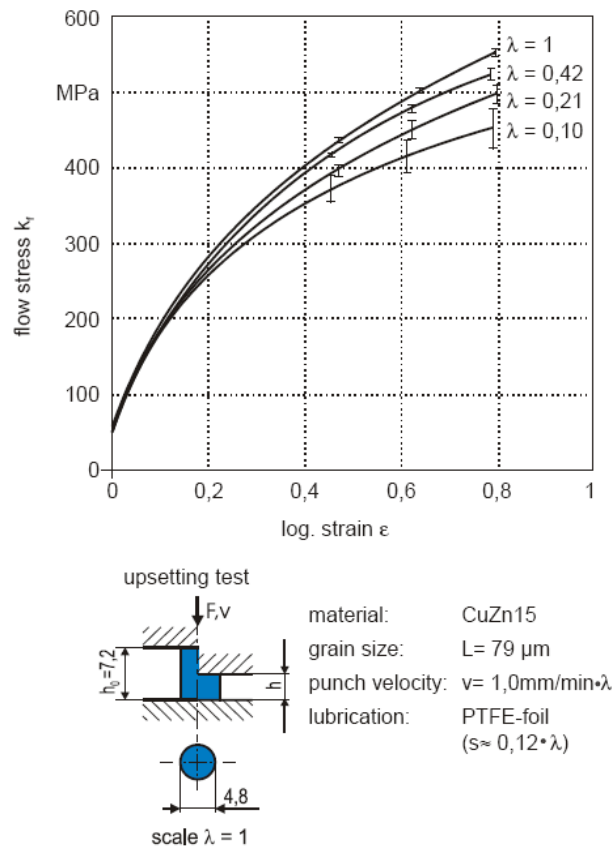


Figure 2-9: Feature size effects in bulk forming [Engel, 2002]

Miyazaki et al. [Miyazaki, 1979] as well as Engel and co-workers [Kals, 2000; Geiger, 2001; Engel, 2002; Engel, 2003] explained the variation in the material flow curve due to the size effects by using a so-called ‘surface layer model,’ proposing as follow: the dislocation movements in the grains located at the surface are less restricted than grains inside the material; therefore, these surface grains show less hardening. Since the ratio of the free surface grain to the internal grain increases with miniaturization (i.e., thickness reduction or scaling down of feature/part size), this would result in a decrease of the flow stress.

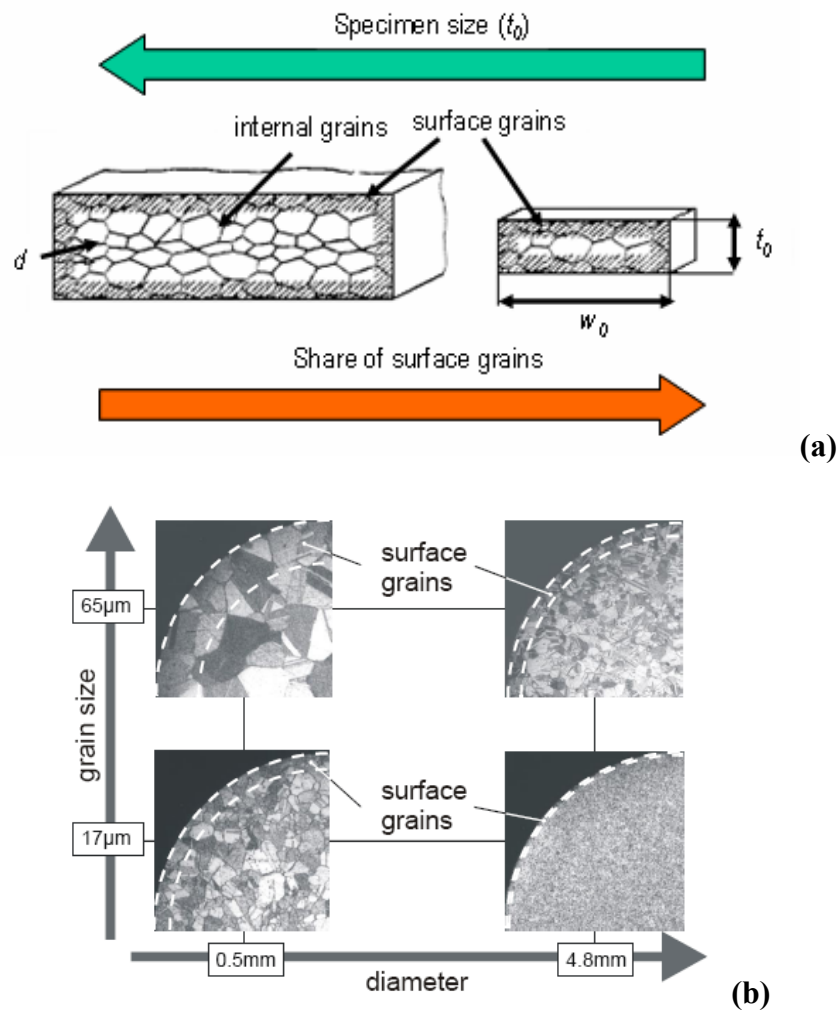


Figure 2-10: Surface layer model in (a) sheet metal [after Kals, 2000], and (b) bulk metal [Geiger, 2001]

In the same study by Kals and Eckstein [Kals, 2000], they also studied the effect of the miniaturization on the material anisotropy. In their report, the vertical anisotropy (\bar{r}) was found to decrease with decreasing sheet thickness in tensile tests as shown in Figure 2-11. This means that the forming characteristics become worse with reduction in sheet thickness which could lead to a problem especially in deep drawing application. However, the plane anisotropy, Δr , does not change significantly with scaling down of the specimen dimensions.

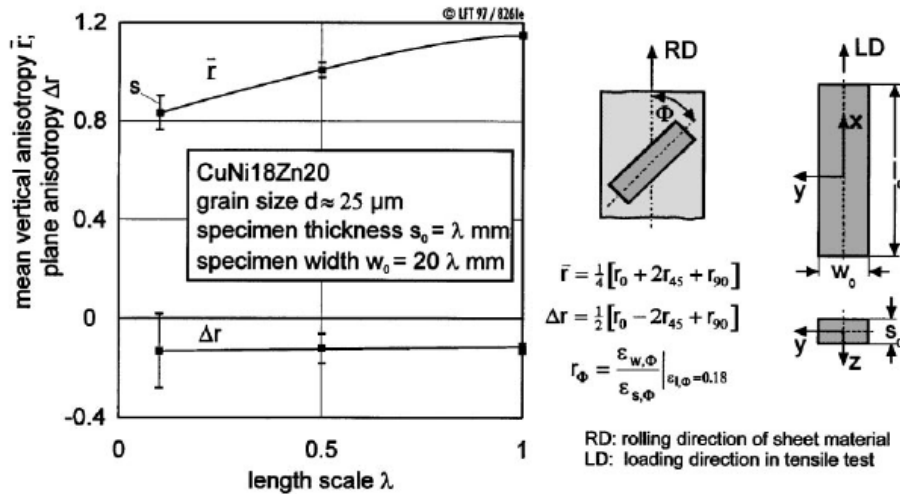


Figure 2-11: Strain anisotropy of CuNi18Zn20 versus length scale λ [Kals, 2000]

The effect of miniaturization on friction was investigated using the ring compression and double cup extrusion (DCE) tests [Engel, 2003]. The ring compression test is based on the fact that the evolution of the inner diameter of a ring during compression depends quite sensitively on friction. The results from the ring compression test showed an increase in friction with miniaturization when an oil lubricant was used. However, this trend was not observed in the case where no lubricant was applied during the ring compression test [Engel, 2002]. To extend the study of the

friction and lubrication, DCE tests were performed as shown in Figure 2-12a. The DCE test conditions are similar to the actual extrusion process because the test involves a large surface area, large strain, and high forming pressure. In the case of no friction ($m=0$), both cups are expected to form to the same height value. However, when the friction at the contact surfaces is not zero, less forming is expected at the lower cup. The difference between the formed height at the top and the bottom value can be used to indicate the magnitude of the friction. The experimental results are shown in Figure 2-12b. It can be seen that friction increases with a decrease in specimen size.

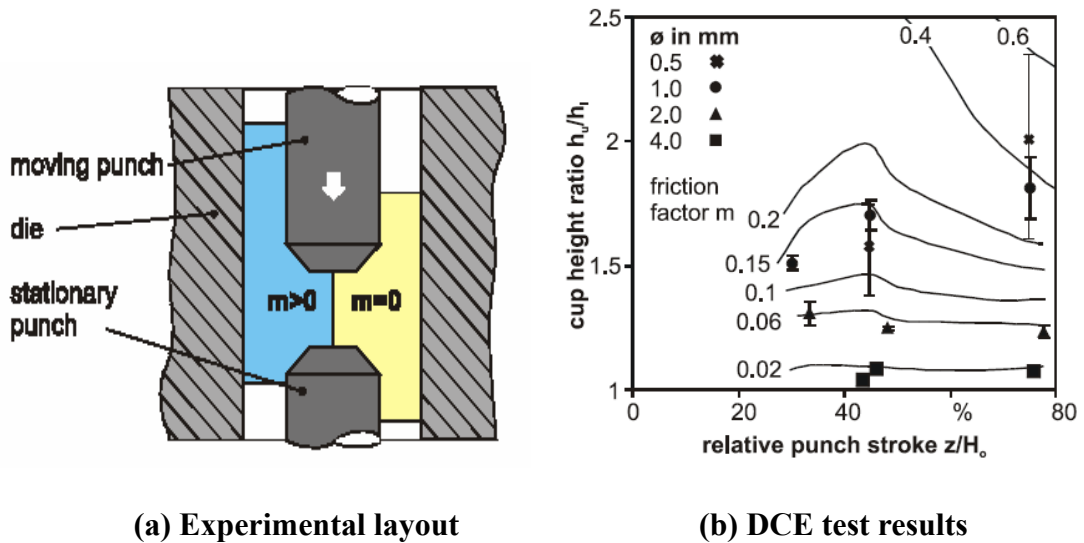


Figure 2-12: Double cup experiment [Geiger, 2001]

The increase of friction in both ring compression and DCE tests is explained by the model of “open and closed lubricant pockets,” Figure 2-13a. Roughness valleys that have a connection to the edge of the surface cannot keep the lubricant. These “open lubricant pockets” fail to distribute the load, resulting in higher friction. On the other hand, closed lubricant pockets trap the lubricant which helps transmit the load, and thus reducing the normal pressure on the asperities. By reducing the size, the ratio of open to

closed lubricant pockets increases as illustrated in Figure 2-13b; thus, resulting in an increase in friction forces. Another proof of the open and closed lubricant pockets model is the use of solid lubricant instead of fluid lubricant. In this case, the mechanism postulated by the open and closed lubricant pockets model is invalid and consequently size effects do not occur [Tiesler, 2000].

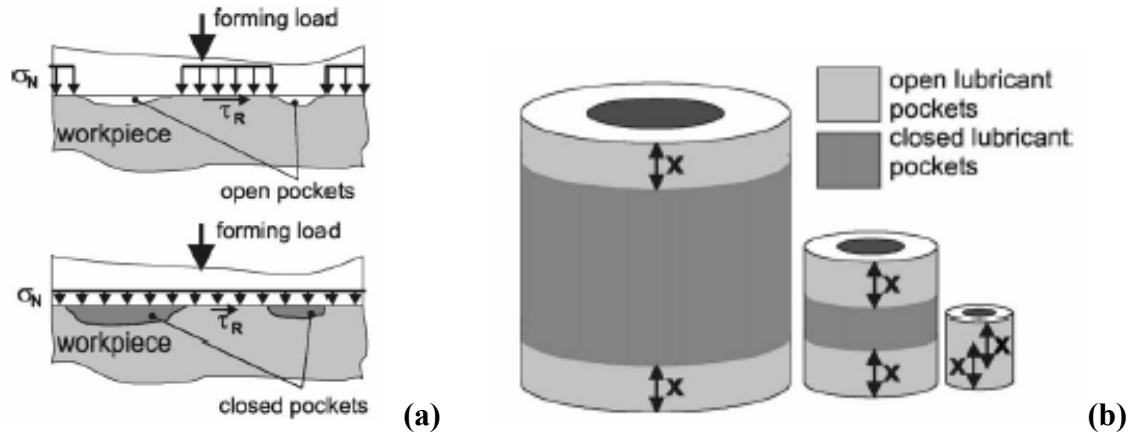


Figure 2-13: Effect of open and closed lubricant pockets on friction [Geiger, 2001]

Another effect that has been observed in many studies in the literature is the increase of scatter with miniaturization. This deviation might be different from part to part due to the random character of microstructure constellation. In microforming, the local deformation will be heavily influenced by the grain size and orientation. Thus, it is obvious that specimens with different grain arrangements will require different forming forces [Engel, 2003].

Despite the fact that the size effects on the material response have been intensively studied in the past decade, surprisingly, up to date there is still no governing equation that could accurately predict the magnitude of these size effects on the material response and behavior, and only qualitative models (e.g., the surface layer model, the open and closed lubricant pockets model) have been put forward to explain the observed

phenomena from the experimental tests. Accurate modeling of the material behavior at the micro-scale is a crucial issue that needs to be understood and addressed before the computational tool (FEA) could be used to advance the microforming technology to the next level. A review of material models that have been proposed with an attempt to explain and include the size effects (i.e., grain vs. feature/specimen size) on the material behavior is presented in the following section.

2.5 Modeling of Size Effects on Flow Stress

In general, the flow stress is used to characterize and represent the material behavior in metal forming since it directly affects the forming forces, tool stress, local flow behavior and thus, filling of the die cavity. For the grain size effect, the most widely accepted theory relating the flow stress and the grain size is the Hall-Petch equation [Hall, 1951; Petch, 1953], which is given as:

$$\sigma(\varepsilon) = \sigma_0(\varepsilon) + \frac{k(\varepsilon)}{\sqrt{d}} \quad (2-1)$$

where $\sigma_0(\varepsilon)$ and $k(\varepsilon)$ are constants at a specific strain (ε), and d is the grain size. The first term, $\sigma_0(\varepsilon)$, is known as the friction stress required to move individual dislocations in the micro-yielded slip band pile-ups confined to isolated grains, where $k(\varepsilon)$ in the second term measures the locally intensified stress needed to propagate general yielding across the polycrystal grain boundaries [Armstrong, 1983].

As for the feature size effect, surprisingly, only qualitative explanations were given by Engel and co-workers using the ‘surface layer model’ as discussed above, while the quantitative model is still lacking. As far as the author knows, only two attempts were recently carried out to study the effect of the feature size on the flow stress and

modify the constitutive relations of the material by taking into account the size effects. The first model proposed by Michel and Picart [*Michel, 2003*] was derived based on the regression analysis of the experimental data from tensile tests of brass sheet (CuZn36) with different thicknesses and grain sizes. By introducing a scaling function, $F(\lambda, \bar{\varepsilon})$, to the Swift model, $\sigma_k = K(\varepsilon_0 + \bar{\varepsilon})^n$, the model was given as follows:

$$\bar{\sigma} = \sigma_k F(\lambda, \bar{\varepsilon}) = [K(\varepsilon_0 + \bar{\varepsilon})^n] \cdot [1 - \exp((-a\lambda + b)(-c\varepsilon + d))] \quad (2-2)$$

where K , ε_0 , and n could be obtained from material testing at macro scale and a , b , c , and d are material parameters calculated based on the results of material testing at micro scale. λ in this model represents the thickness of the sheet.

The second model, proposed by Kim et al. [*Kim, 2007*], introduced two new parameters (α and β) to modify the Hall-Petch equation based on the fundamental understanding of single- and poly-crystals deformation. Kim's model was given as follows:

$$\sigma(\varepsilon) = M^\alpha \tau_R(\varepsilon) + \frac{k(\varepsilon)}{\sqrt{d}} \beta \quad (2-3)$$

where $M^\alpha \geq 2$, $\alpha \leq 1$, $0 \leq \beta \leq 1$, and $\beta = 0$ for single crystal and $\alpha = \beta = 1$ for polycrystal. M is the orientation factor to account for slips systems, and τ_R is the resolved shear stress as suggested by Armstrong [*Armstrong, 1983*]. The relationship between the new parameters, α and β , and the ratio of the characteristic length of the workpiece to the grain size, n , is given in Figure 2-14. The simulated results carried out by Kim et al. showed very good agreement with various set of experiments reported in previous literature.

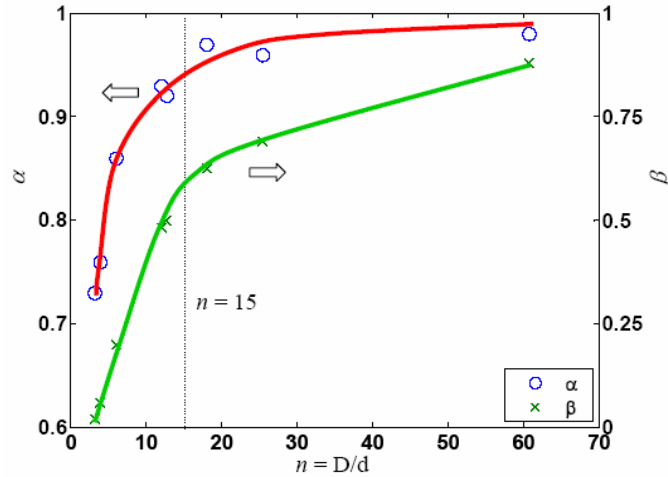
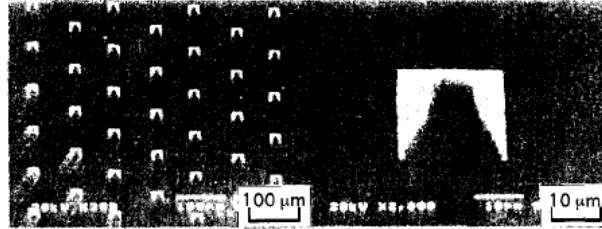


Figure 2-14: Relationship between parameters α and β and the n ratio where D is the characteristic length and d is the grain size [Kim, 2007]

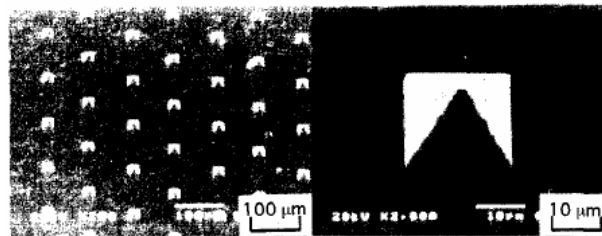
2.6 Microforming Processes

2.6.1 Micro-forging

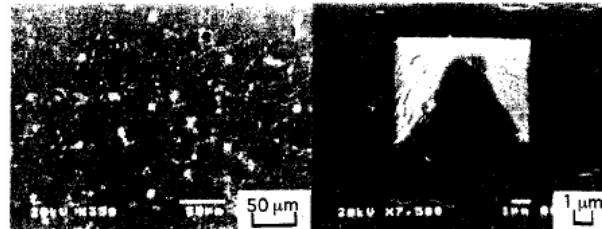
Micro-forging process feasibility and characteristics has been investigated using V-grooved micro-dies of (100) silicon on superplastic material and amorphous alloys in supercooled liquid state by Saotome et al. [Saotome, 1994 and 2002]. The micro-dies were fabricated using photolithography and anisotropic etching techniques with the V-groove width between 0.1 μm and 20 μm . The experimental results show good microformability of both superplastic material and amorphous alloys in the supercooled liquid state under very low stresses in comparison with a conventional plastic deformation. Micro-pyramids and micro-gear of superplastic and amorphous alloys in supercooled liquid state forged with the silicon dies are shown in Figure 2-15.



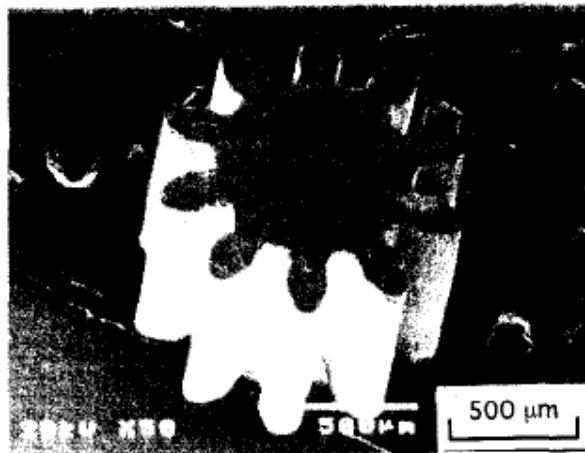
Al-78Zn fine grained superplastic alloy
Initial stress $\sigma_i=10$ MPa, Forming temperature $T=520$ K



Zr₆₅Al_{7.5}Cu_{27.5} amorphous alloy
Initial stress $\sigma_i=10$ MPa, Forming temperature $T=680$ K



La₅₅Al₂₅Ni₂₀ amorphous alloy
Initial stress $\sigma_i=10$ MPa, Forming temperature $T=500$ K



Micro-gear of La₅₅Al₂₅Ni₂₀ amorphous alloy
formed by closed die forging under a super-cooled liquid condition.

Figure 2-15: Micro-pyramids and micro-gear forged with Si die [Saotome, 1994]

Cold and warm forging of micro-parts using CuZn15 specimen with the diameter of 0.5 mm to 4.8 mm was studied by Engel et al. [Engel, 2003]. The process is carried out in the region of 100 °C to 450 °C, characterized as a warm forming process for the CuZn15 material. As expected, the reduction of flow stress is observed with increasing temperature due to increasing recovery mechanism, Figure 2-16. The scatter of data is also reduced with increasing temperature due mainly to the additional slip systems that are activated at elevated temperatures enabling even grains of unfavorable orientation to deform, i.e., less inhomogeneity flow of material.

Average hardness gradient (AHG) is a parameter that could be used to characterize the degree of homogeneity – the higher the value, the more inhomogeneous. The values are shown in Figure 2-17. It can be clearly seen that at high temperatures the material flow is more homogeneous. Additionally, the average hardness shows that the temperature effect is very small for the range of 20 to 200°C.

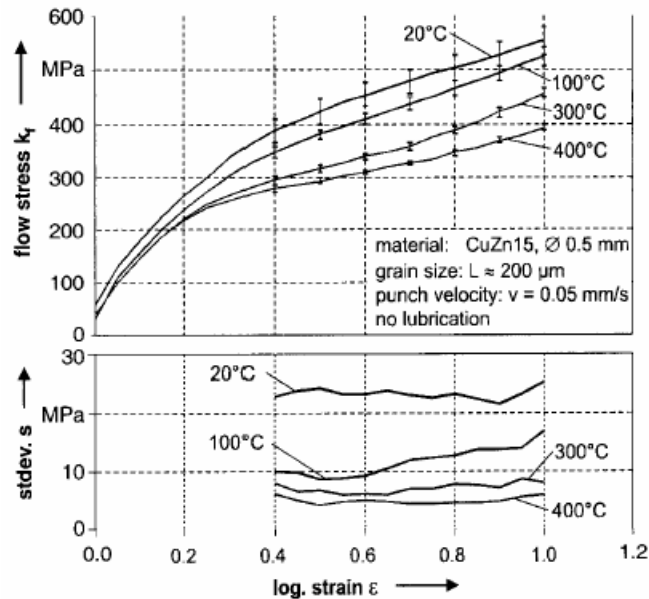


Figure 2-16: Flow stress and standard deviation of flow stress at different temperatures [Engel, 2003]

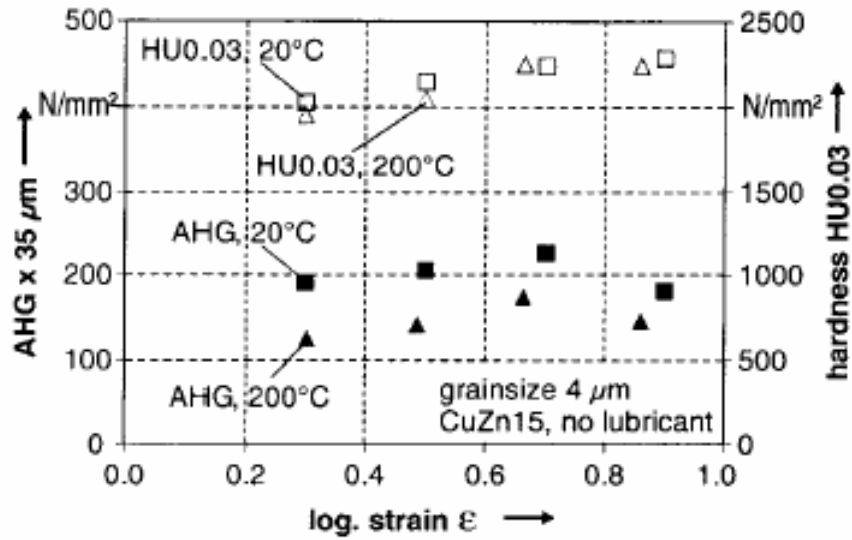


Figure 2-17: Average hardness gradient (AHG) and universal hardness (HU0.03) [Engel, 2003]

2.6.2 Micro-embossing/coining

The investigation of cold embossing using silicon die has been carried out by Otto and Bohm [Otto, 2000; Bohm, 2001]. The first set of experiments by Otto used aluminum 99.5 as the material, embossed at the room temperature with the straight channel feature. The result is shown in Figure 2-18. Based on this experimental result, the feasibility of molding structures smaller than the grain size of the material without damaging the silicon die is verified.

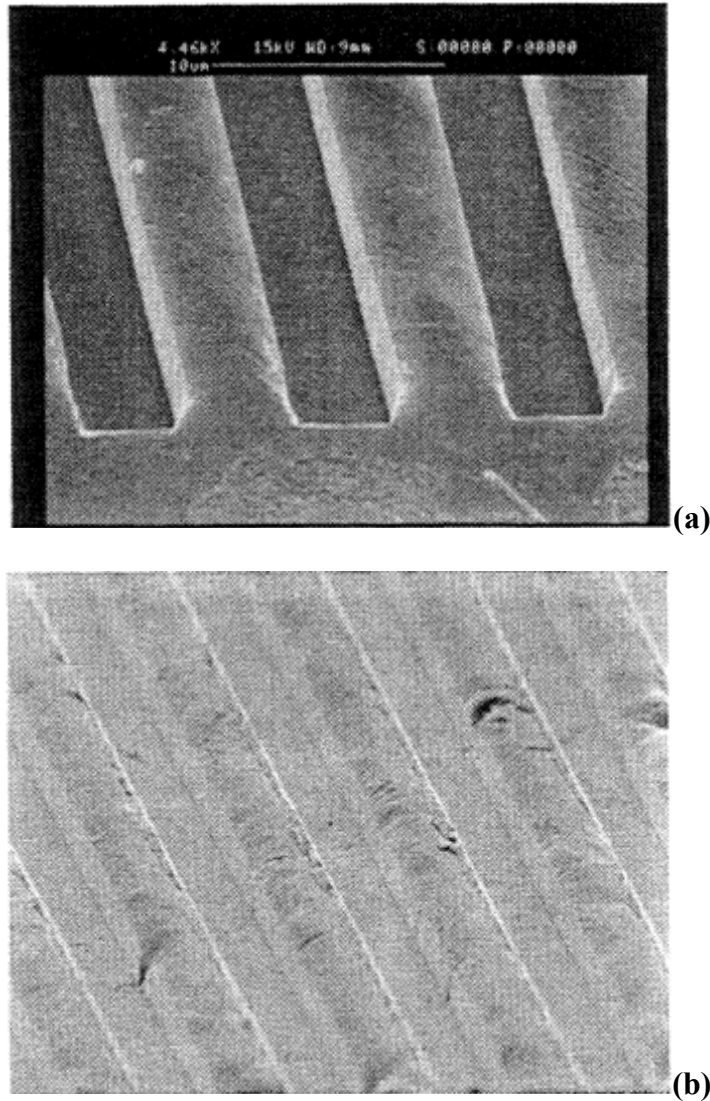


Figure 2-18: SEM images of (a) etched Si die, and (b) embossed gratings with groove depth of 2.5 μm [Otto, 2000]

The second attempt to study the cold embossing process by Bohm was focused on the study of forming precision and die-wear for different micro-geometries, applied loads, and work piece materials. Two patterns of silicon die features were used: complex and straight channel structures (Figure 2-19). For the complex structure, aluminum, stainless steel, copper, and brass are used as the blank material. The results show that complex structures can be formed with all of the four materials with very high

precision (Figure 2-20). However, the necessary compression stress must be much higher than the yield stress of the respective material. Moreover, for sharp edges at the bottom, a further increase of the pressing force is required.

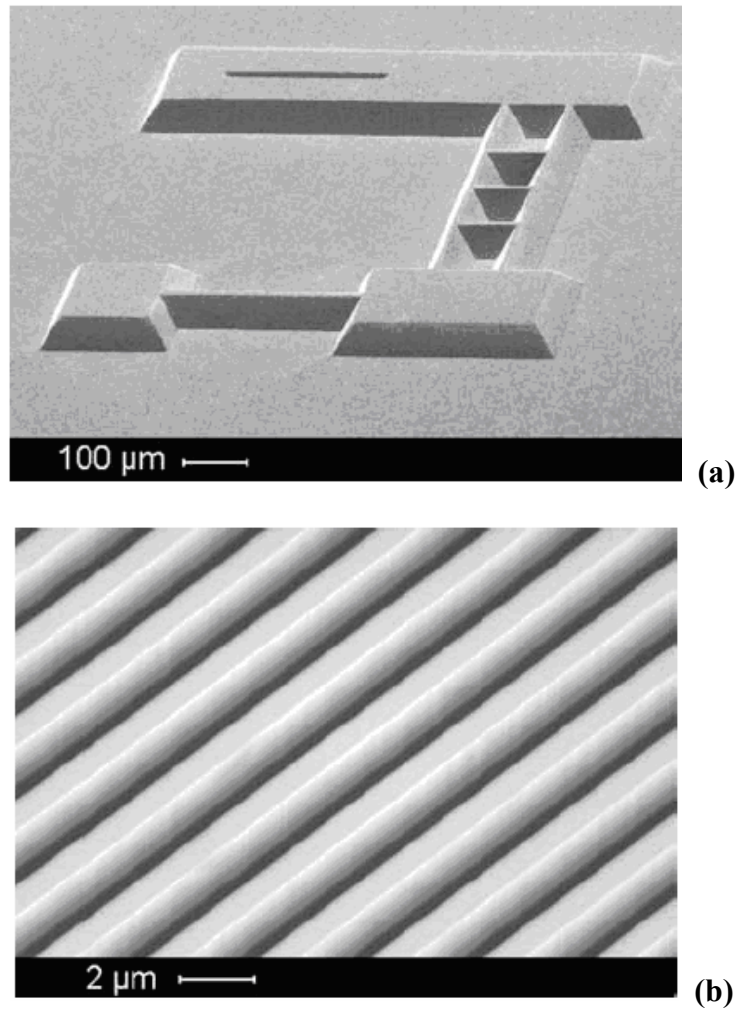


Figure 2-19: Silicon die with (a) complex structure, and (b) straight channel structure [Bohm, 2001]

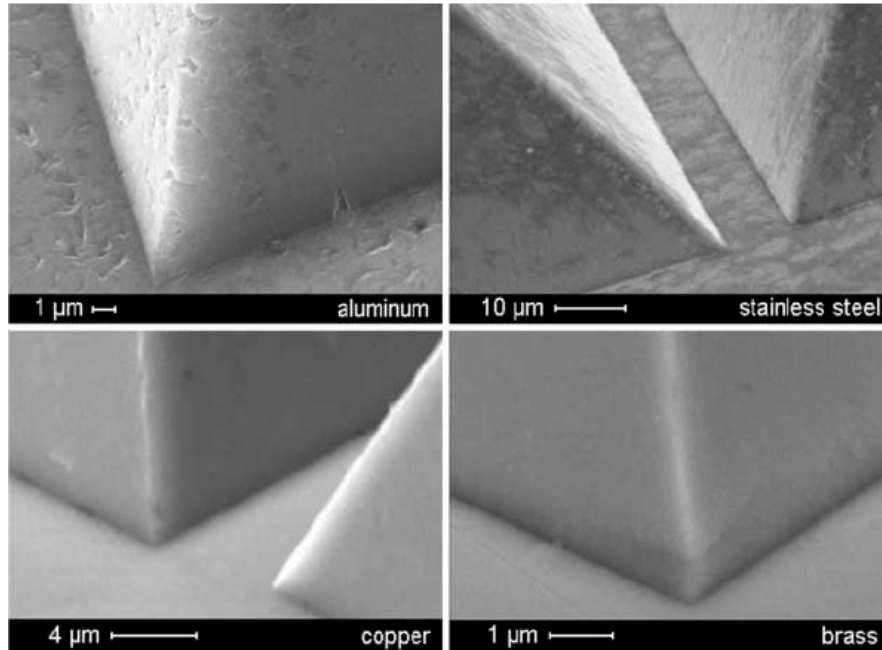


Figure 2-20: Detail of complex structure after cold embossing [Bohm, 2001]

For the straight channel structure, only aluminum is employed in the experiment to point out the possibility of molding of structures smaller than the grain size of the material (grain size $> 3 \mu\text{m}$). Figure 2-21 represents an embossed straight channel structure with a gap width of $1 \mu\text{m}$ on aluminum sheet. Based on the results, etched silicon dies prove to be capable of providing accurate molding at the micro-level, but the range of use is limited to soft material and/or low compressive stresses. The life of silicon dies is strongly influenced by the design of the microgeometry and coating.

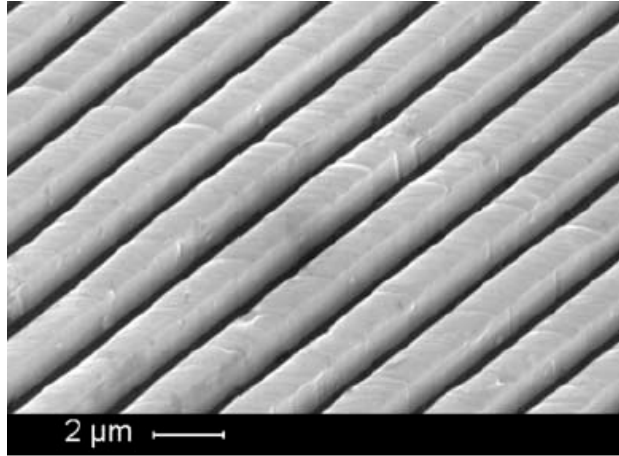
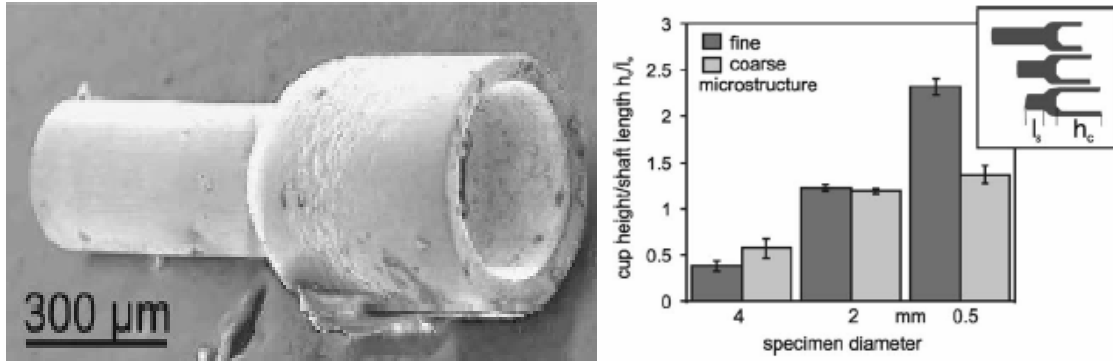


Figure 2-21: Embossed straight channel structure with a gap with of 1 μm on Al99.5 sheet with material grain size $> 3 \mu\text{m}$ [Bohm, 2001]

2.6.3 Micro-extrusion

To show the effect of microstructure on miniaturization, forward rod – backward can extrusion process was investigated by Geiger and Engel [Geiger, 2001; Engel, 2002]. Billet diameters between 0.5 and 4 mm were used. As shown in Figure 2-22, the ratio of the cup height and shaft length (h_c/l_s) increases with miniaturization with fine grains (grain size of 4 μm). However, when coarse microstructure is used (grain size of 120 μm), there is no increase in the ratio of h_c/l_s for the billet diameter of 0.5 mm. This observed result is explained by the effect of the microstructure of the specimen; that is, when the material grain size is larger than the thickness of the cup wall, it is easier for the material to flow into the shaft rather than into the cup wall. This example illustrates the importance of the exact knowledge of the miniaturization effects for part, process, and tool design.



(a) part originally was $\phi 0.5$ mm

(b) effect of microstructure

Figure 2-22: Forward rod – backward cup extrusion: effect of microstructure [Geiger, 2001; Engel, 2002]

The quality of the product is also affected by miniaturization. Figure 2-23 shows the shape of the rim in the backward can extrusion. The irregular formation shape of the rim is caused by grains of different size and orientations passing through the clearance between the die and the punch, which is quite smaller than the mean grain size, thus yielding an inhomogeneous material flow and finally the observed irregular shape.

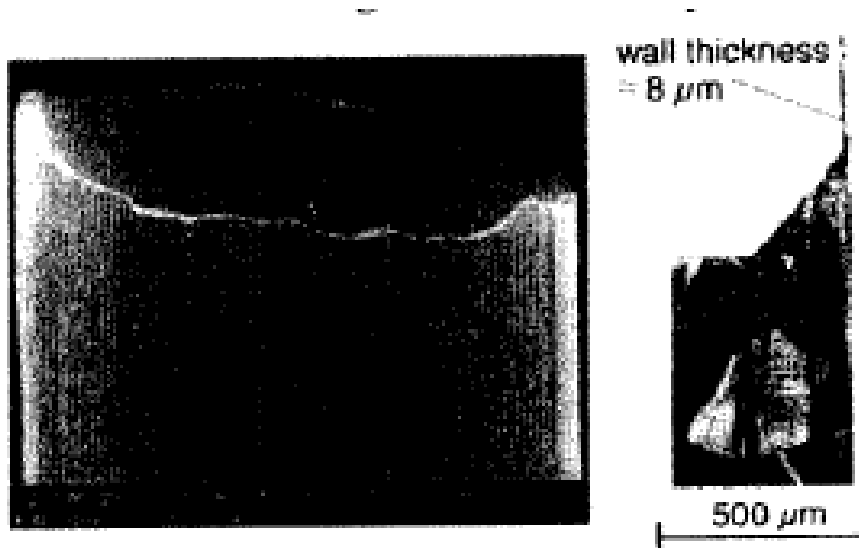


Figure 2-23: Backward can extruded part, SEM picture and cross sectional micrograph [Engel, 2003]

Micro-forward and backward extrusion of micro-gear shafts of 50 μm in module and 500 μm in diameter of the pitch circle have been successfully produced with comparable low forces and high aspect ratios (Figure 2-24). Amorphous alloys display perfect Newtonian viscous flow and are suggested for fabricating micro-machines [Otto, 2000].

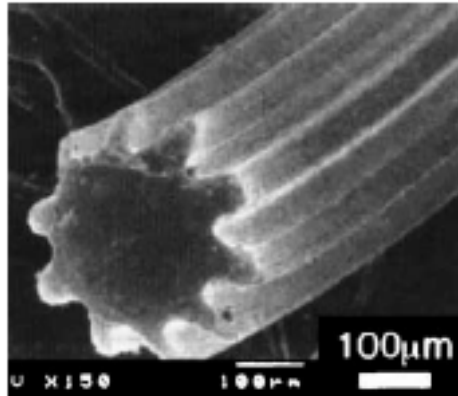


Figure 2-24: A forward-extruded micro-gear shaft – La₆₀Al₂₀Ni₁₀Co₅Cu₅ amorphous alloy, gear module = 50 μm , number of teeth =10 [Otto, 2000]

Recently, a meso-scale extrusion experiment had been conducted to extrude micropins with 1.2 and 0.48 mm in diameter by Cao et al. [Cao, 2004]. CuZn30 specimens were heat treated to obtain three different grain sizes: 32, 80, and 200 μm . The grain size effect on the flow stress was investigated through the ram force versus ram displacement plot as shown in Figure 2-25. From the result plot, smaller grain size billet was shown to require higher ram force. This means that the flow stress increases with decreasing grain size, the result that agrees with the Hall-Petch equation [Hall, 1951; Petch, 1953].

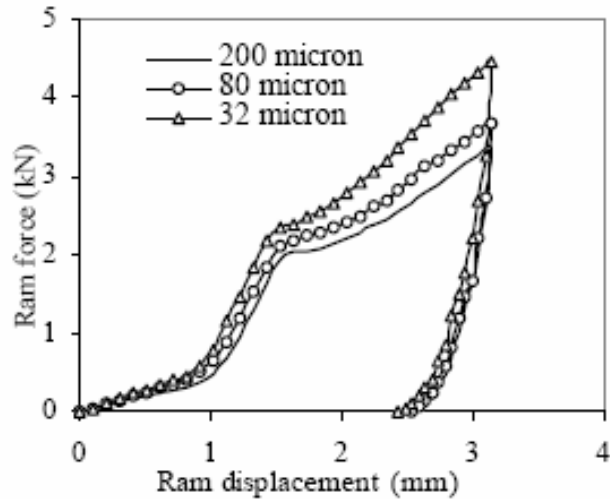


Figure 2-25: Force-displacement response for extrusion of micropins with different initial grain size [Cao, 2004]

2.6.4 Micro-bending

Bending experiments in sheet metal forming also show similar size effects associated with miniaturization – decrease of flow stresses with miniaturization. However, experiments have shown that this is valid in most cases, but the model fails when only single grain is located over the thickness of the sheet [Kals, 1999; Raulea, 2001]. In other words, the flow stresses during the experiments decrease with miniaturization and increasing grain size until one point; thereafter, an increase in the flow stress is observed with increasing grain size as shown in Figure 2-26 [Geiger, 2001]. This contradicts the theory of metal forming with conventional dimensions, where the flow stress decreases with increasing grain size according to Hall-Petch relation [Hall, 1951; Petch, 1953].

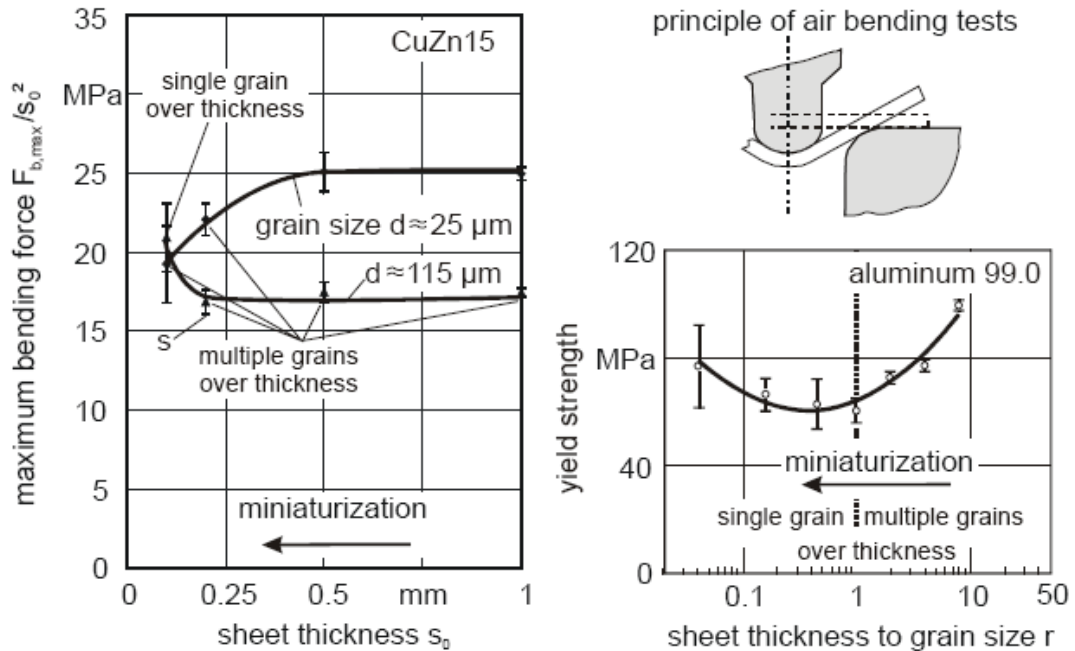
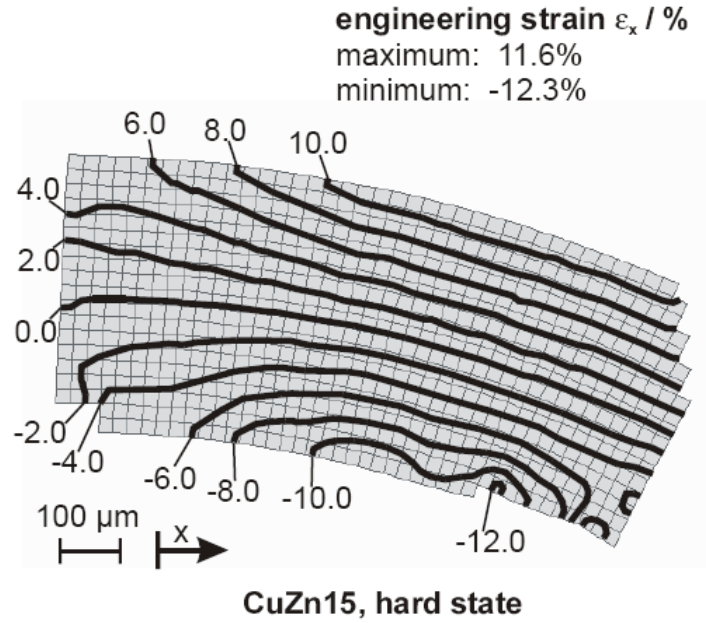
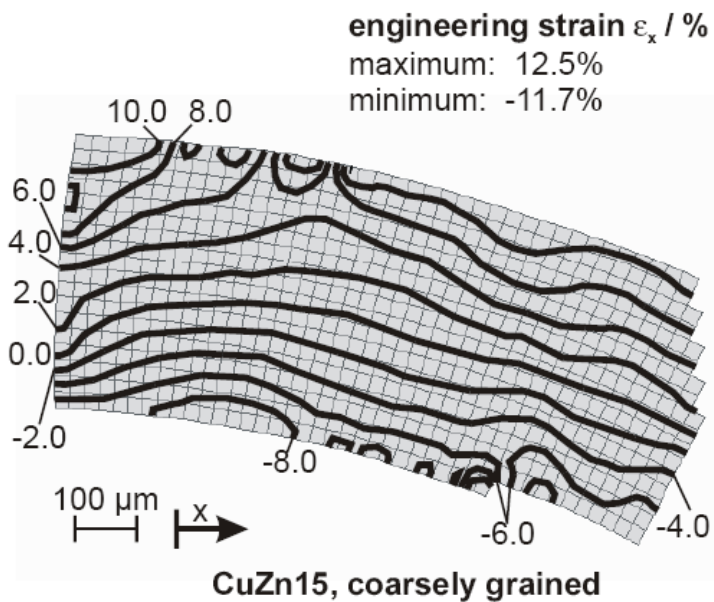


Figure 2-26: Bending forces and yield strength in bending tests [Geiger, 2001]

The effect of the grain size on the strain distribution in bent specimens was also discussed in the same work by Geiger et al. [Geiger, 2001]. Sheet blanks of CuZn15 with initial sheet thickness of 0.5 mm were bent and the strain distribution was plotted as shown in Figure 2-27 for fine grains (grain size = 10 μm) and coarse grains (grain size = 70 μm). The fine grain blank (Figure 2-27a) shows the typical distribution of strains for a bending process, while the coarse grain blank (Figure 2-27b) shows the disturbed strain distribution by the irregular orientation of the grains. This may be the reason for an increase in bending force when only a single grain is located over the thickness as the deformation mechanism will be minimized with a single grain structure, as opposed to finer and multiple grains that would have additional deformation paths (i.e., through grain boundary motions and slip lines).



(a)



(b)

Figure 2-27: Strain distribution from bending experiment: (a) fine grain, and (b) coarse grain [Geiger, 2001]

2.6.5 Micro-deep Drawing

Micro-deep drawing of very thin sheet steels below 0.2 mm thickness was investigated by Saotome et al. [Saotome, 2001]. The punch diameter to thickness ratio,

D_p/t , was chosen as an important parameter. A punch diameter of 1 mm was used with varying sheet thickness, allowing the ratio of D_p/t to vary between 10 and 100. Material properties of very thin sheet steel ($t = 0.05$ mm or below) were obtained from a new apparatus. Experimental results are shown in Figure 2-28. Selected parameters were D_p/t , R_d/t , blank holder pressure, p , and drawing ratio $\beta = D_s/D_p$.

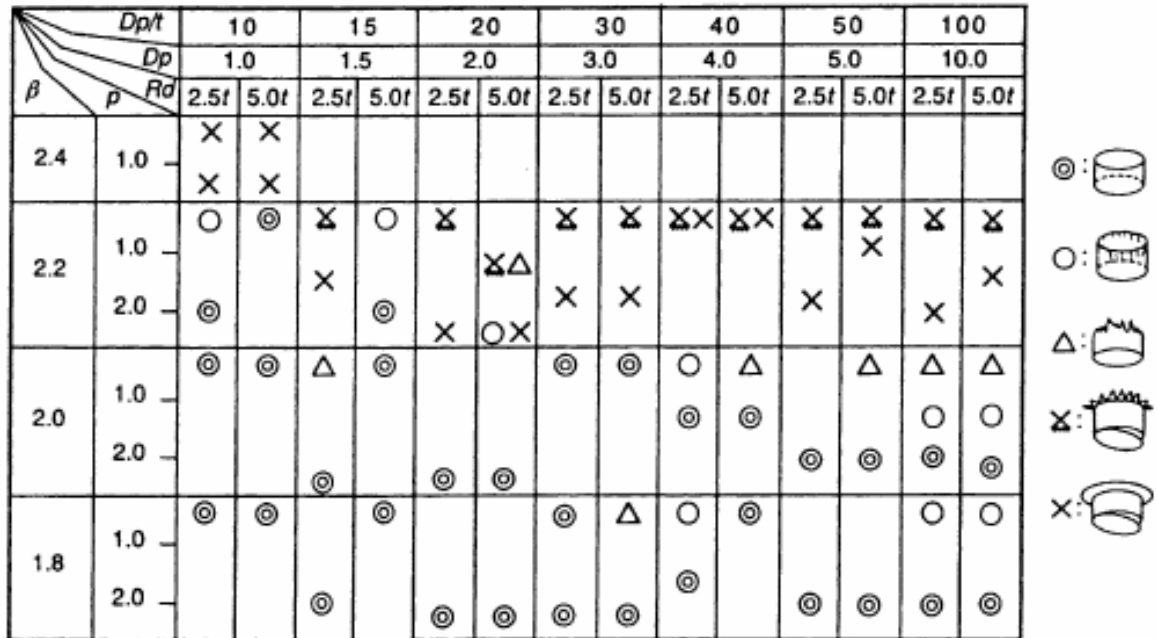


Figure 2-28: Micro-deep drawing results, $t = 0.1$ mm [Saotome, 2001]

It can be observed that the limiting drawing ratio (LDR) decreases as D_p/t increases. The effect of blank holder pressure, p , is clearly recognized above D_p/t of 40. As D_p/t increases, the required blank holder pressure increases. Also, the effect of die radius, R_d , on drawability is observed below D_p/t of 15. Higher blank holder pressure is required as R_d/t decreases. In addition, to study the geometrical similarity law in the micro-deep drawing process, further experiments were conducted with specimen thicknesses of 0.05, 0.1, 0.2 and 1.0 mm in the same study. The results are shown in

Figure 2-29.

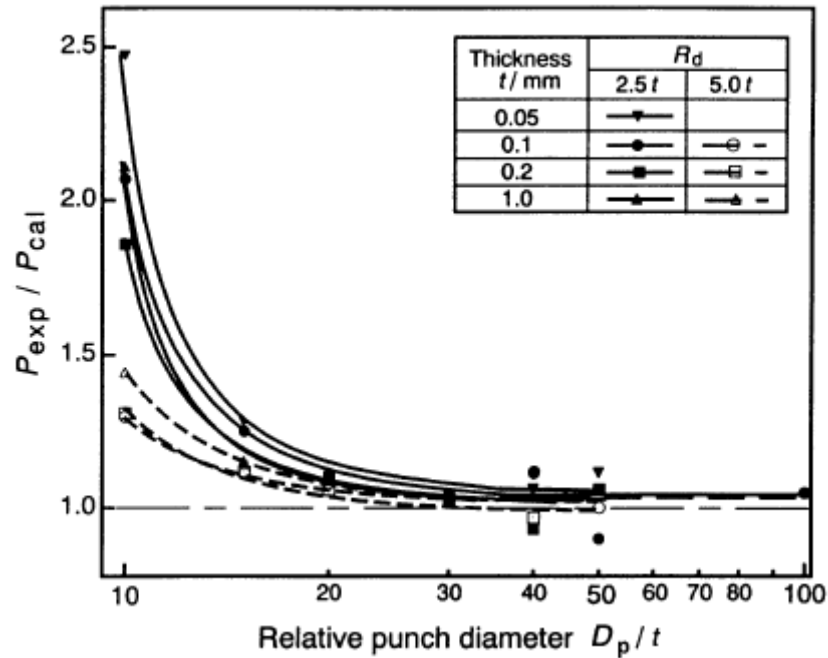


Figure 2-29: The ratio $P_{\text{exp}}/P_{\text{cal}}$ for various conditions [Saotome, 2001]

The maximum punch force, P_{exp} , was measured during the experiment, and the maximum force, P_{cal} , was calculated based on Hukui's and Yoshida's equation [Saotome, 2001]. Figure 2-29 shows that $P_{\text{exp}}/P_{\text{cal}}$ is very close to unity for D_p/t above 40. This suggests that the geometrical similarity exists for D_p/t exceeding 40. However, below D_p/t of 20, the ratio $P_{\text{exp}}/P_{\text{cal}}$ deviates from unity, and the effect of the die radius becomes remarkable. Also, at $D_p/t = 10$ and $R_d/t = 5$, bending is considered to be the dominant forming mechanism since the blank holder pressure has little effect on the drawability and no effect on the working material during the latter half of the drawing process.

Micro-deep drawing of cups with diameters between 1 and 8 mm on CuZn37 material (thickness between 80 μm and 300 μm) were performed by Witulski et al. [Witulski, 2004]. The cups were drawn successfully as shown in Figure 2-30. Punch

force was measured in the experiments and later used for result comparisons with the simulation. After the FE models were validated, they were used to further study the effects of other process parameters such as friction coefficient, transverse anisotropy, drawing gap, and blank holder gap, on the overall drawability. The effect of each process and material parameter was discussed in details in their work [Witulski, 2004]. The material flow curve used in the FE models was obtained from simple tensile tests with the maximum true strain of 0.22, extrapolating to the strain of 0.7 using LUDWIK's law:

$$k_f(\varphi) = k_{f0} + c_0 \cdot \varphi^{n_0}$$

where k_f and φ represent flow stress and true strain, respectively, and k_{f0} , c_0 , n_0 are material constants obtained from tensile test.

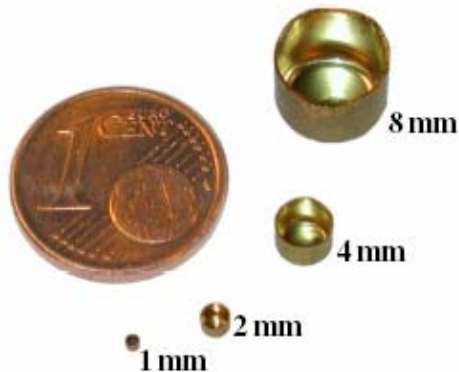


Figure 2-30: Micro deep drawing cups drawn with punch diameters from 8 to 1mm [Witulski, 2004]

Micro-deep drawing experiments of Al 99.5 foil with sheet thickness of 20 μm and mild steel foil with sheet thickness of 25 μm were carried out using 1 mm punch diameter by Vollertsen et al. [Vollertsen, 2004]. The final shapes of the drawn cups obtained at the macro- and micro-scales were compared. Wrinkling was observed on

the flange of the micro-cup, Figure 2-31. Friction force was found to decrease in both macro- and micro-cups when lubricant was applied; however, the amount of the decreased friction force was significantly higher in the micro-cup than that in the macro-cup, Figure 2-32.

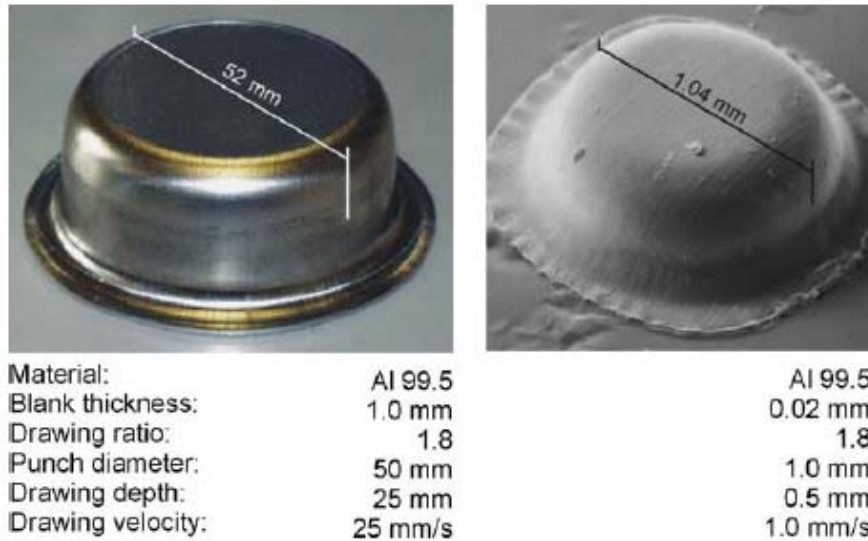
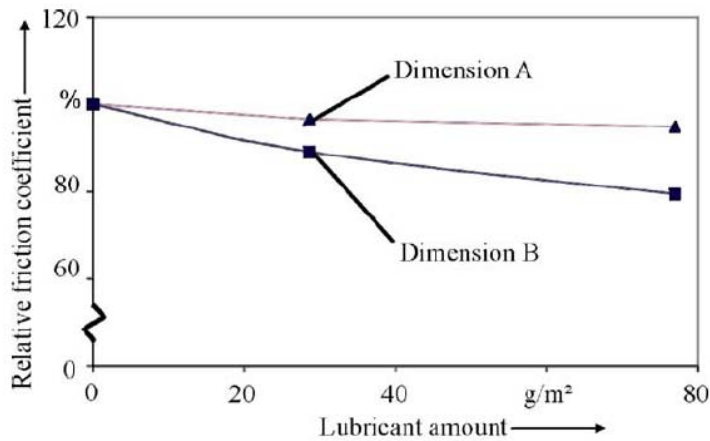


Figure 2-31: Comparison of macro and micro deep drawing cups [Vollertsen, 2004]



	Dimension A	Dimension B
Material:	St 15	1.0335
Blank thickness:	1.35 mm	0.025 mm
Drawing ratio:	1.7	1.7
Drawing velocity:	25 mm/s	1 mm/s
Lubricant:	HBO 947/11	HBO 947/11

Figure 2-32: Comparison of the effects of lubricant [Vollertsen, 2004]

Punch force was also compared between the two scales. It was found that the forming force was much higher than the calculated value for the micro-cup, while the force for the macro-cup was almost equal to the calculated value. Therefore, the friction coefficient in microforming is much greater than that in macro-forming. Vollertsen et al. also investigated the variation in the friction coefficient at the flange and the die radius by using strips of St 14 material with 1 mm in thickness. They found that the friction coefficient was unequal at these two locations, and it depended on the applied normal pressure. The plots of the friction coefficient at the flange and the die radius were calculated from the punch force, and the result is shown in Figure 2-33.

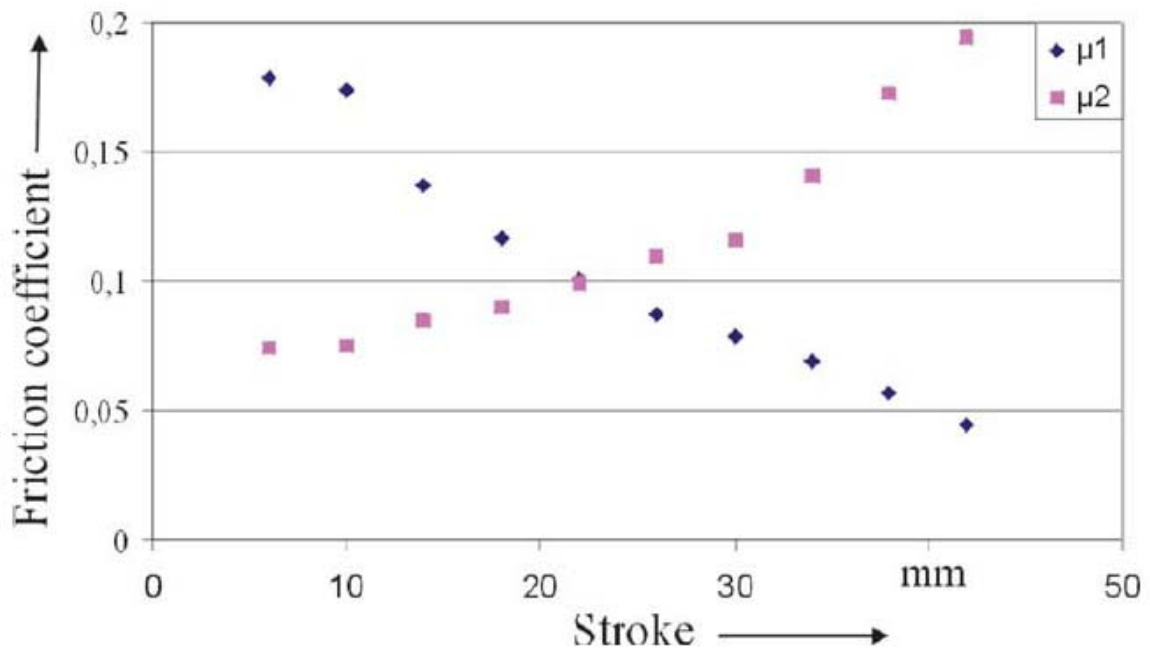


Figure 2-33: Friction coefficient value at the flange (μ_1) and die radius (μ_2) with lubricant 2 g/mm^2 [Vollertsen, 2004]

2.6.6 Micro-hydroforming

A study of micro-hydroforming process for fabrication of micro-features on thin metal sheets was performed by Joo et al. [Joo, 2004]. Successful forming of thin foil

metals (AISI 304 stainless steel with 2.5 μm -thick and pure copper with 3.0 μm -thick) into micro-channels of various shapes with the channel dimensions ranging from 10-20 μm in width and 5-10 μm in height using a static pressure up to 250 MPa is shown in Figure 2-34.

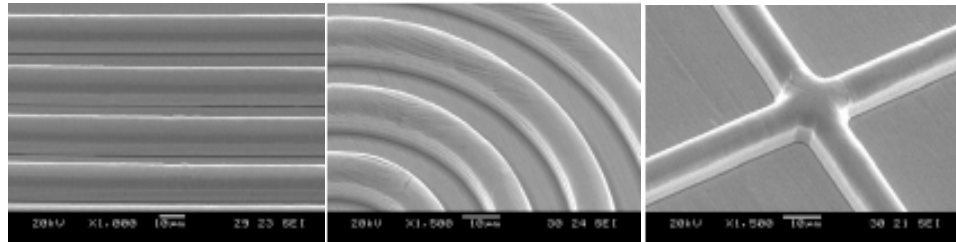


Figure 2-34: Hydroformed micro-channels on ultra thin copper foil [Joo, 2004]

The experimental results showed that the copper sheet could be fully formed into a concentric channel shape, while the stainless steel sheet could not be fully formed into any channel shapes. Furthermore, the effect of inter channel distance was revealed on the wall thickness distribution of copper foil. The results showed extreme thinning up to about 75% when a narrower inter channel distance of 1 μm was used as compared to the wider channel spacing as shown in Figure 2-35.

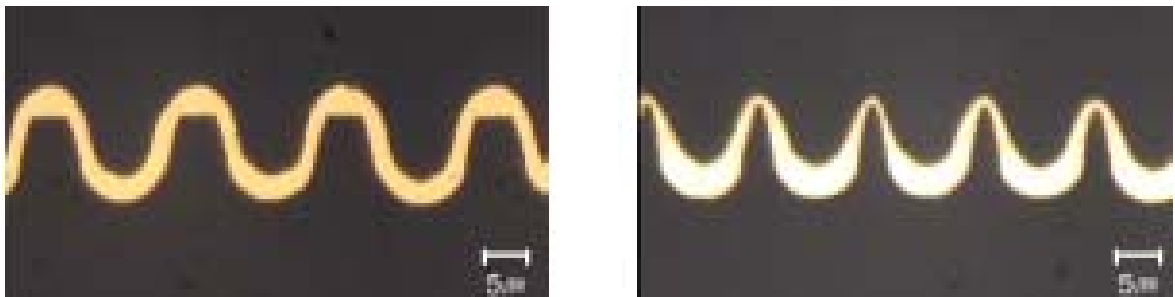


Figure 2-35: Effect of inter channel distance on thickness distribution of the copper foil [Joo, 2004]

2.7 Pressure Welding

Pressure welding is a solid-state joining method of similar or dissimilar ductile metals by bringing the surfaces to be joined in contact under high compressive pressure. This joining technique offers a fast, simple, and inexpensive method to provide a bond as strong as the parent materials without involving heat, flux or filler [Mepsted, 2002]. The combinations of metals that have been reported to successfully bond together by the cold (pressure) welding technique are shaded in the table shown in Figure 2-36, while the non-shaded blocks represent the metal pairs that cannot be cold welded. Cold welding can be accomplished in both lap (bar or sheet) and butt (wire or rod) configurations. Depending on the material, bar and sheet with thickness between 0.1 to 15 mm [Thomas, 1993] as well as wire and rod with diameter between 0.08 to 30 mm [Mepsted, 2002] have been successfully cold welded. In addition, this welding technique can be used in joining of metal combinations that cannot be fusion welded, e.g., Al-Cu, Al-Fe, and Al-Ti [Bay, 1986].

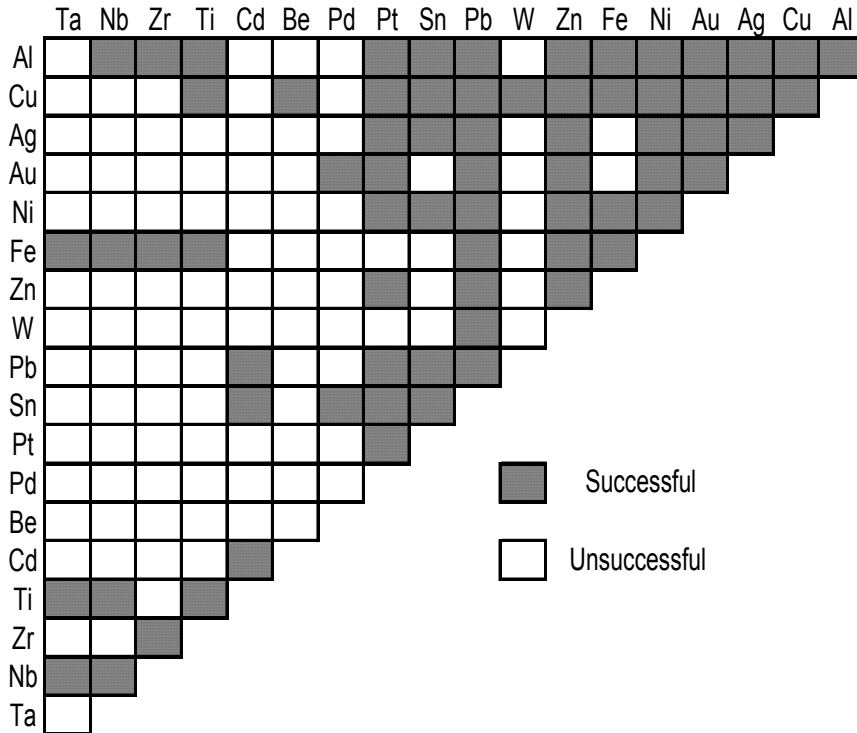


Figure 2-36: Applicability of cold pressure welding for different metal combinations [Thomas, 1993]

2.7.1 Mechanisms of Bond Formation

The mechanisms of the bond formation in cold welding have been the subject of research for many decades. Among the existing hypotheses explaining the bond formation (e.g., the mechanical hypothesis, the energy-barrier hypothesis, the diffusion-bonding hypothesis, and the joint-recrystallization hypothesis), the most widely accepted hypothesis is based on the mechanical bonding force between the negatively and positively-charged atoms at the two absolutely clean metallic surfaces which are brought closely together with only a few angstroms separation [Thomas, 1993; Lukaschkin, 1996; Mepsted, 2002; Li, 2003]. However, most metal surfaces in atmospheric environments are covered with a number of surface layers which prohibit metallic bonding when bringing two surfaces in contact. Therefore, in practice, a *film theory* [Zhang, 1996]

was proposed to explain the actual mechanism of the bond formation as follow: the contaminant layers at the surfaces will fracture, allowing the underlying base material to be extruded through the cracks of these broken layers, thus, resulting in a weld, as illustrated in Figure 2-37.

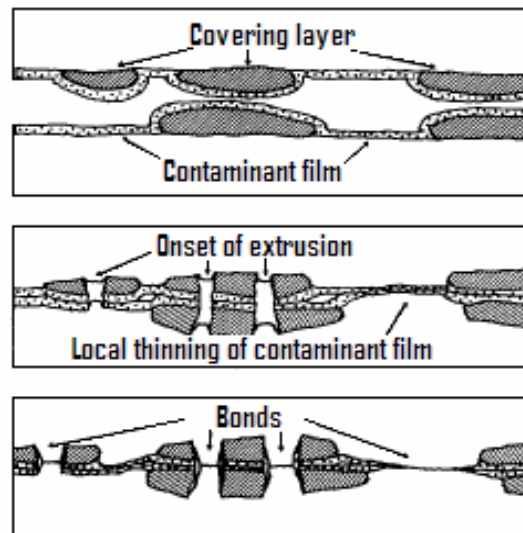


Figure 2-37: Bonding mechanism for scratch-brushed surfaces [Bay, 1986]

2.7.2 Theoretical Models for Calculating Bond Strength

Even though the importance of many factors on the final bond strength has been demonstrated, e.g., surface condition, surface preparation time, oxide film thickness, surface roughness, presence of adsorbed gas layers [Vaidyanath, 1959], the effect from these factors cannot be evaluated, because the information gained from various modeling system cannot be correlated. In other words, the impact of these factors on the bond strength varies from one setup to another; thus, cannot be included in a generic predictive model for the bond strength. Nevertheless, several theoretical models have been developed for a prediction of the bond strength attained in cold welding based on the *film theory* which deals with the fracture of the surface layers and bonding of contaminants-

free metal surfaces brought into contact under high pressure condition. Only the models based on this bond formation mechanism are discussed here.

An early attempt was made by Vaidyanath et al. [*Vaidyanath, 1959*] which proposed a simple theoretical model for calculation of the maximum ultimate shear strength of the bond obtained by cold rolling as a function of only one parameter, the final thickness reduction, R_f . In this model, the weld efficiency, η , is defined as the ratio between the strength of the weld, S_w , to the strength of base metal, S_m . The proposed models are as follows:

$$\eta = \frac{S_w}{S_m} = R_f(2 - R_f)$$

This model was derived using plane strain analysis in combination of the tri-axial stress condition. This model was later modified by Wright et al. [*Wright, 1978*] to include the threshold deformation, R_t , and the empirical hardening factor, H , as follows:

$$\eta = \frac{S_w}{S_m} = H \left(1 - \frac{(1 - R_f)^2}{(1 - R_t)^2} \right)$$

The threshold deformation is the deformation below which no welding takes place. The empirical hardening factor in this model is introduced to capture the weld strength that is stronger than the base metal ($H > 1$). Both of these newly introduced parameters are meant to be determined from the experiments. In both models proposed by Vaidyanath and Wright, the oxide layers covering the two surfaces were assumed to break up as one, so that the total length of the oxide layer is always equal to the original length of the specimen, and these oxide layers were assumed to remain at the interface of the two workpieces, as illustrated in Figure 2-38. Based on these assumptions, the total area of the cracks in the covering layers is a maximum value. Therefore, the bond strength

value obtained from these models result in an upper bound prediction of the bond strength and the applications of these models are undoubtedly limited.

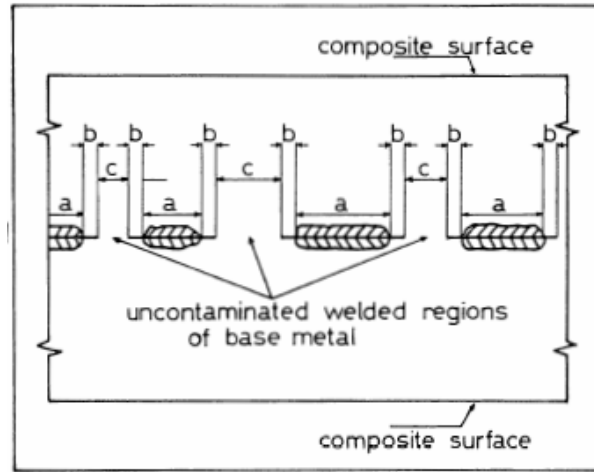


Figure 2-38: Contaminant layers combined, fractured as one, and stayed at the interface [Wright, 1978]

Bay, in 1986, derived another model based upon the analysis of the bonding mechanisms using a SEM. In his model, the bond strength is calculated as a function of surface expansion, surface preparation, and normal pressure, as follows:

$$\frac{\sigma_B}{\sigma_0} = (1 - \beta)Y \frac{p - p_E}{\sigma_0} + \beta \frac{Y - Y'}{1 - Y'} \frac{p}{\sigma_0}$$

where σ_0 = yield stress of the weaker metal between the two metals to be joined; β = area of surface with no scratch brushed layer; p = applied pressure; p_E = extrusion pressure; Y = surface expansion; and Y' = surface expansion at which contaminant film fractures. The first mechanism, extrusion of material through the cracks of the cover layer, is accounted for by the first term on the right hand side of the equation, while the second term on the right hand side represents the fracturing of contaminant films. Based on these mechanisms, if the applied pressure is less than the extrusion pressure required to squeeze the material through the cracks ($P < P_E$), the first term should be set to zero.

Similarly, the second term should be set to zero when the surface expansion is less than the surface expansion at which contaminant film fractures ($Y < Y'$). This model was validated by various sets of experiments. Bay's model was later modified by Zhang [Zhang, 1996] based on an assumption that the bond strength obtained between the absolutely clean surface is equal to the compression stress applied in cold welding. Two additional parameters, overlapping surface exposure, ψ , and the effective normal pressure, p_B , were introduced in this new model.

Another theoretical model for the plane-strain upsetting of a two-metal sandwich sheet was developed by Lukaschkin and Borissow in 1996. The model was derived based on the plastic flow of metals on their contact surfaces to realize the minimum displacement as a function of welding pressure and friction stresses at the interface. The bond strength, σ_B , is represented as a function of the softer metal strength, σ_f^S , and a coefficient of interface expansion, K , as follows (subscript H represents harder material, while S represents softer material):

$$\sigma_B = \sigma_f^S K$$

In their proposed model, the K value is calculated as follow:

$$K = \frac{F_s F_h}{F_c^2}$$

where F_s and F_h are the active contact area (the area of pure metal on the surface uncovered by contaminant layers) for softer and harder materials, respectively, which are the sum of the fractured area of the contaminant layers at the surface, i.e.,

$$F^s = \sum_{i=1}^{i=n} C_i^s(x), \text{ and } F^h = \sum_{i=1}^{i=n} C_i^h(x), \text{ as illustrated in Figure 2-39. } F_c \text{ is the real}$$

contact area.

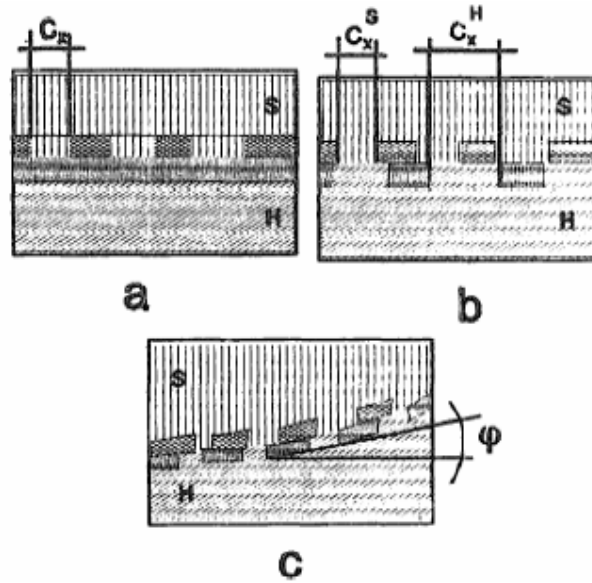


Figure 2-39: The possible schemes of the fracture of the surface layers [Lukaschkin, 1996]

Recently, another model was developed by Madaah-Hosseini and Kokabi [Maddh-Hosseini, 2002], based on the cold rolling process. By combining the strain

model in a strip rolling process: $\varepsilon = \frac{2}{\sqrt{3}} \ln \left(\frac{1}{1-R_f} \right)$, and the work hardening equation

(Power Law) of the metal workpiece: $\sigma = K\varepsilon^n$, an equation representing the strength of the metal is proposed as:

$$S_m = K\varepsilon^n = K \left[\ln \left(\frac{1}{1-R_f} \right) \right]^n.$$

Based on the assumption that the weld efficiency (η) equals to 100% at the critical thickness reduction ($R_{f,cri}$ – defined as the reduction at which the base metal fractures), then the relationship between the weld strength, S_w , and the base metal strength, S_m , can be written as:

$$S_{w,cri} = \frac{F_{w,cri}}{A_w} = S_m = K \left[\ln \left(\frac{1}{1 - R_{f,cri}} \right) \right]^n .$$

Rearranging this equation, A_w (area of the weld) is then:

$$A_w = \frac{F_{w,cri}}{K} \left[\ln \left(\frac{1}{1 - R_{f,cri}} \right) \right]^{-n} .$$

Madaah-Hosseini proposed the weld efficiency equation as follows:

$$\eta = \frac{S_w}{S_m} = \frac{S_w}{K} \left[\ln \frac{1}{1 - R_f} \right]^{-n} .$$

2.8 Numerical Modeling of Micro-scale Deformation

Finite element analysis (FEA) is an important and respected research tool used to support, and in some cases, explain the results obtained from the experiment or derived from traditional approaches of theory. As with any tool, its effectiveness heavily depends on the skill and dedication of the researcher who guides its use. This is especially true in microforming research where properties of material differ from conventional scale and the ambiguous characterization of the deformation mechanism and surface interaction are not fully understood. Since the length scale of the microforming processes is in the range of a few hundred micrometers, which is between the macro-scale (millimeter) and the molecular scale (angstrom), both continuum mechanics and molecular dynamics simulations appear to be legitimate candidates.

Molecular dynamics deals with simulating the motion of molecules to understand the physical phenomena that derive from dynamics molecular interactions. The goal of the molecular dynamics simulations is to understand and to predict macroscopic

phenomena from the properties of individual molecules making up the system. And with continuing advances in the methodology and the speed of computers, molecular dynamics studies are being extended to larger systems, greater conformational changes, and longer time scales. The results available today make clear that the applications of molecular dynamics will play an even more important role in the future [*Karplus, 2003*].

On the other hand, in continuum mechanics, material and structural properties are assumed to be homogeneous throughout the entire structure for a simplifying approximation of physical quantities, such as energy and momentum. Differential equations are employed in solving problems in continuum mechanics. Some of these differential equations are specific to the materials being investigated, and are called constitutive equations, while others capture fundamental physical laws, such as conservation of mass or conservation of momentum. The physical laws of solids and fluids do not depend on the coordinate system in which they are observed. Despite the fact that continuum mechanics completely ignores the heterogeneity in a structure, the continuum mechanics simulation has been successfully used in a wide range of application in many research fields. Continuum mechanics was originally intended to model the behavior of structural components, with dimensions of order 0.1 – 100 m or so. To apply the continuum mechanics in micro-scale analysis, the issue we need to address is the actual fact that the material is highly inhomogeneous at this micro-level, and that as a result the stress and strain fields are nowhere near uniform and homogeneous.

The obvious advantage of the molecular dynamics simulation over the continuum mechanics simulation is that it gives a route to dynamical properties of the system: transport coefficients, time-dependent responses to perturbations, rheological properties

and spectra. The predictions are ‘exact’ in the sense that they can be made as accurate as we like, subject to the limitation imposed by the computer budget [Allen, 2004]. However, since MD simulations start at the scale of an atom and the time on the order of femtoseconds, running simulations to large size and times is prohibitive. In fact, there is a competition between the time and size scales as illustrated in Figure 2-40 in terms of computing power [Horstemeyer, 2001]. Note that non-local continuum mechanics theories involve adding strain gradients or dislocation density evolution equations that include a spatial length scale.

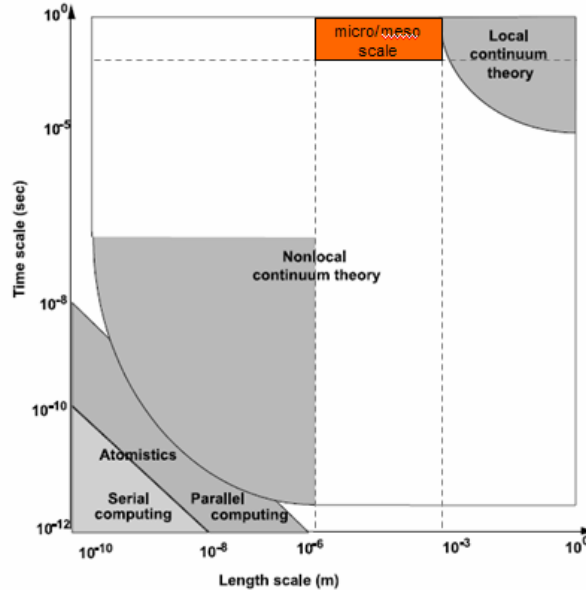


Figure 2-40: Schematic of strain rate and spatial size scale effects on computing and the regions where local and non-local continuum theories are applicable [Horstemeyer, 2001]

Figure 2-40 shows that as the simulation time (inversely related to the applied strain rate) increases, the computational power is the main constraint that limits the size of the block material. Similarly, as the block size increases, the computational times require fairly large applied strain rates (i.e., short simulation time). Strains rates lower than the

order of 10^6 s^{-1} are not feasible at this time in atomistic simulations. For example, a 10 nm cubic domain of a metal can be simulated only for times less than around 10^{-10} s , even on very large parallel machines [Horstemeyer, 2001]. This computational limitation is the major factor that prevents the extensive use of MD simulations in an analysis of structures larger than nanometer-scale.

Since the scope of the current study is in the range of hundreds of micrometers in length, and seconds in time, which is in the orders of magnitude above the length and time scales that the MD simulations with the current computational power can handle, the continuum mechanics simulation approach will be selected for validation of various analytical models and experimental results. By comparing the results obtained from the simulation with the experimental data, the FE models will also be verified and could be used for further investigations such as in parametric study and process optimization. Finally, with an accurate material model of micro-scale specimens, the continuum mechanics simulations are believed to provide a fair comparison to the experimental results at a reasonable level of accuracy.

2.9 Summary and Research Issues

Fuel cells have been proven to have various advantages over other power generation sources without having to rely on limited resources such as fossil fuels, while producing no harmful emissions. However, the current manufacturing cost of the fuel cells is still too high to be able to compete with other power generation sources, especially in the automotive application. To reduce the manufacturing cost, the development of new materials and manufacturing methods are inevitably required. Bipolar plate, a vital component of fuel cell stacks, stands out as high-volume, -weight,

and -cost. The existing manufacturing methods of the bipolar plate are slow, costly, and result in heavy fuel cell stacks. Additionally, to ensure high fuel cell performance, cooling water channels must be added. With the existing methods, an additional operation is required in order to join and seal the two plates together to obtain the internal cooling channels.

Microforming technology has a great potential for manufacturing of micro-parts, considering its process simplicity and high production rate. However, as the ratio of feature size to grain size decreases, the few grains and their orientations become more dominant and have significant impact on the material response and deformation mechanisms. The material behavior can no longer be considered as homogeneous. Previous research attempts have been carried out to qualitatively analyze and explain the “size effects” which cause the deviations in material response. However, quantitative models and analyses, especially for characterizing the material flow curve, are still lacking, and are needed for accurate process analysis. In addition, the previous research investigations mostly focused on microforming of discrete parts. Issues in microforming of micro-scale features (micro-channels) on a macro-scale part (large plate) have not been advanced yet.

For numerical investigations of microforming processes, the continuum mechanics simulation approach is more appropriate than the molecular dynamics due mainly to the limitation in terms of current computational power. In addition, with accurate material models, the continuum mechanics simulation approach is believed to provide reasonable predictions of the deformation in different microforming processes.

Pressure welding at room temperature (a.k.a. cold welding) has been shown to

successfully join different combinations of metals. ‘Thin film’ theory has been widely accepted to explain the bond formation in the cold welding process. Based on this theory, several models for prediction of the bond strength have been proposed. However, these models were developed for materials at conventional scale, leaving out the ‘size effects’. At the micro-scale, the effect of sheet thickness on the weldability should also be considered. Furthermore, these models are not practical for a rapid calculation because they contain some immeasurable parameters such as the area of the contaminant film (oxide layer) break up at the contact interface. Finally, cold welding technique cannot be applied to stainless steel and metal alloys with carbon content. Modifications to this welding technique are necessary to create bonding between stainless steel or metal alloys with carbon content blanks (e.g., use of heat, ultrasonic vibrations, etc.).

In the following four chapters, the findings in the state of the art review as presented in this chapter are utilized to the benefits of the development of the novel hybrid manufacturing process.

CHAPTER 3: INVESTIGATION OF SIZE EFFECTS ON MATERIAL BEHAVIOR OF THIN SHEET METALS USING HYDRAULIC BULGE TESTING

3.1 Introduction

The applications of micro-features (channels, arrays, bumps, etc.) have been consistently broadening in the past decades due to the miniaturization trend of devices in the field of electronics, consumer products, energy generation/storage, medical devices, and micro-system technology (MST) for the enhancement of heat and mass transfer. Specific examples include fuel cells, fuel reformers, micro-heat exchangers, micro-fluidic devices, medical devices, optical arrays, etc. Metal forming processes, well known for their process simplicity, high production rate, minimized material waste, near-net-shapes, excellent mechanical properties, and close tolerances, were claimed to be the most suitable processes to fabricate micro-parts/features, especially when high volume-low cost production is desired [Engel, 2002; Vollertsen, 2004]. However, there are challenges in scaling down the traditional metal forming processes to the micro-levels because of the unknowns in friction conditions, deformation mechanics, and material behavior due to the so-called “size effects” (i.e. grain size vs. feature/specimen size). At the micro-scales, the material behavior is characterized by only a few grains located in the deformed area; thus, the material can no longer be considered as a homogeneous continuum as in the macro-scales. Instead, it was suggested that the material response is dominated by the size and orientation of individual grains [Engel, 2003]. In terms of

numerical analysis of the process, conventionally used constitutive material models are questionable for accurate modeling at the micro-scales. Therefore, the goal of this study is to investigate and understand the “size effects” on the material behavior of thin sheet metals.

In the next section, an overview of the past studies related to the size effects is presented. In the third section, experimental setup and procedures are described, followed by a discussion of results. In the last section, new material models, both qualitative and quantitative, are developed to include the size effects parameters. Finally, the developed models are validated with the experimental results in this study as well as in the literature.

3.2 Grain, Specimen, and Feature Size Effects

According to Armstrong and Kim [*Armstrong, 1961; Kim, 2007*], the size effects can be investigated under two categories – the “grain size effect” and the “feature/specimen size effect”. The “grain size effect” has been known to follow the Hall-Petch equation [*Hall, 1951; Petch, 1953*], which simply states that the material with larger grain size demonstrates less strength than the one with smaller grain size. This effect purely depends on the average size of the material grains and is the dominant effect on the material response at the macro-levels. However, as the feature/specimen size reduces to the micro-scales, the “feature/specimen size effect” has also been reported to have considerable impact on the material response; and thus, manufacturability.

Depending on the material testing methods or metal forming processes, the “feature/specimen size effect” could be further divided into two distinctive effects – the “feature size effect” and the “specimen size effect”. In general, the “specimen size” can

be referred to as the diameter of a billet (rod) or the thickness of a blank (sheet) to be tested or formed, while the “feature size” could be regarded as the smallest features (channels, radii, protrusions, etc.) on the final part that these specimens will be formed into. For example, in an extrusion process of micro-pins [Cao, 2004], the specimen size would be the initial diameter of the rod/billet, while the feature size would be the diameter of the reduced section. In the case of micro-channels formed on initially flat thin sheet blank, specimen size will be regarded as the thickness of the blank, while micro-channels will be the feature of interest and their dimensions (i.e., width, height) will represent the feature size. Similarly, in a bulge test of thin sheet blank, the specimen size will be the blank thickness, while the feature size will be the bulge diameter. With this distinction between the specimen size and the feature size effects, it is obvious that a tensile test could only be used to study the effect of the specimen size, but not the feature size on the material behavior.

Even though these size effects can be distinguished based on the above discussion, as the grain, specimen, and feature sizes get smaller and smaller into the micro-scales, their effects are coupled; and therefore, should be considered together. In this study, two characteristic parameters N and M are used to couple and represent these interactive effects, where N is defined as the ratio between the specimen and the grain sizes, and M is the ratio between the feature and the specimen sizes. By defining N and M this way, all combinations of the interactive effects, i.e., grain-to-specimen, specimen-to-feature, and grain-to-feature sizes, can be represented and quantified using N , M , and $N*M$, respectively. A summary of different types of size effects and their corresponding characteristic parameters is presented in Table 3-1, where d is material grain size, t_0 is

specimen thickness, D_0 is specimen diameter, and D_c is die cavity.

	Size Effects		
	Grain size	Specimen size	Feature size
Tensile test	d	t_0, D_0	-
Bulge test	d	t_0	D_c
Stamping process	d	t_0	D_c
Extrusion process	d	D_0	D_c
Characteristic parameter	$N = t_0/d$ or D_0/d		$M = D_c/t_0$ or D_c/D_0

Table 3-1: Type of size effects and characteristic parameters

The “specimen size effect” (t_0 or D_0) on the material flow curve as a measure of material response was observed in various tensile test conditions for a variety of materials such as CuAl alloy [Miyazaki, 1979], CuNi18Zn20, CuZn15 [Kals, 2000], CuZn36 [Michel, 2003], and aluminum [Hansen, 1977; Raulea, 2001]. While the grain size shows a strong effect on the material response at all length scales (i.e., from macro- to micro-scale), it is not until the N value is around 10-15 that the “specimen size effect” starts to influence the material response [Hansen, 1977 confirmed by Kim, 2007; Onyancha, 2006]. In general, the tensile test results showed a decreasing trend of the flow stress with the decreasing specimen size (i.e., decreasing N value) as illustrated in Figure 3-1a and Figure 3-1b. Similar observations were reported in upsetting tests of Copper, CuZn15, and CuSn6 [Engel, 2002] as illustrated in Figure 3-1c, and in bulging test of CuZn36 [Michel, 2003] as illustrated in Figure 3-1d. This trend of decreasing flow stress with decreasing N value was rather consistent based on the results of various studies. However, as N is reduced close to a range of 2-4, several researchers had reported an increase in the flow stress as N is decreased further. For instance, the tensile test results of 99.999% Al rods by Hansen [Hansen, 1977] showed an increase in the flow stress as N decreases from 3.9 to 3.2 (Figure 3-1a). Similar results were also observed in micro/meso-scale hydraulic bulge testing of thin CuZn36 blanks [Michel, 2003] where

the flow stress was found to increase as N value decreases from 5 to 3.3 ($d = 60 \mu\text{m}$, t_0 reduced from 0.3 to 0.2 mm) as shown in Figure 3-1d. An increase in the flow stress was also observed as N is reduced close to 1 (single crystal deformation) as reported in bending tests of CuZn15 and Aluminum 99.0-99.5% [Kals, 2000; Raulea, 2001]. Nevertheless, in the tensile test results of CuNi18Zn20 specimens by Kals [Kals, 2000], a continuous decrease in the flow stress was reported as N decreased from 25 to 2.5 (i.e., $d = 40 \mu\text{m}$, $t_0 = 1.0, 0.5,$ and 0.1 mm) as shown in Figure 3-1b. A summary of the effect of N on the flow stress based on the findings reported in the literature is presented in Figure 3-2.

In contrast, studies on the “feature size effect” are only few and quite recent. In a study by Michel and Picart [Michel, 2003], thin blanks of CuZn36 with initial thickness of 0.25 mm were bulged using two different bulge diameters of 20 and 50 mm, corresponding to $M = 80$ and 200, respectively. They observed a decrease in the material flow stress when using the smaller bulge diameter. Their results revealed the effect of the feature size on the material response. Unfortunately, no discussion or explanation for this phenomenon was provided in their publication regarding the feature size effect (i.e., bulge diameter). Comprehensive understanding of the feature size effect (D_c or M) is still lacking and requires further investigations, both qualitatively and quantitatively, due to an impressive fact that micro/meso-scale channel or feature arrays on large surface area are increasingly used and needed for a wide range of end products for enhanced heat/mass transfer purposes.

Therefore, it is the goal of this study to investigate these size effects (i.e., grain, specimen, feature sizes) on the material response to better understand and be able to

include the effects into the material models that will be used in the eventual numerical investigations of the hybrid manufacturing process for the fuel cell bipolar plates.

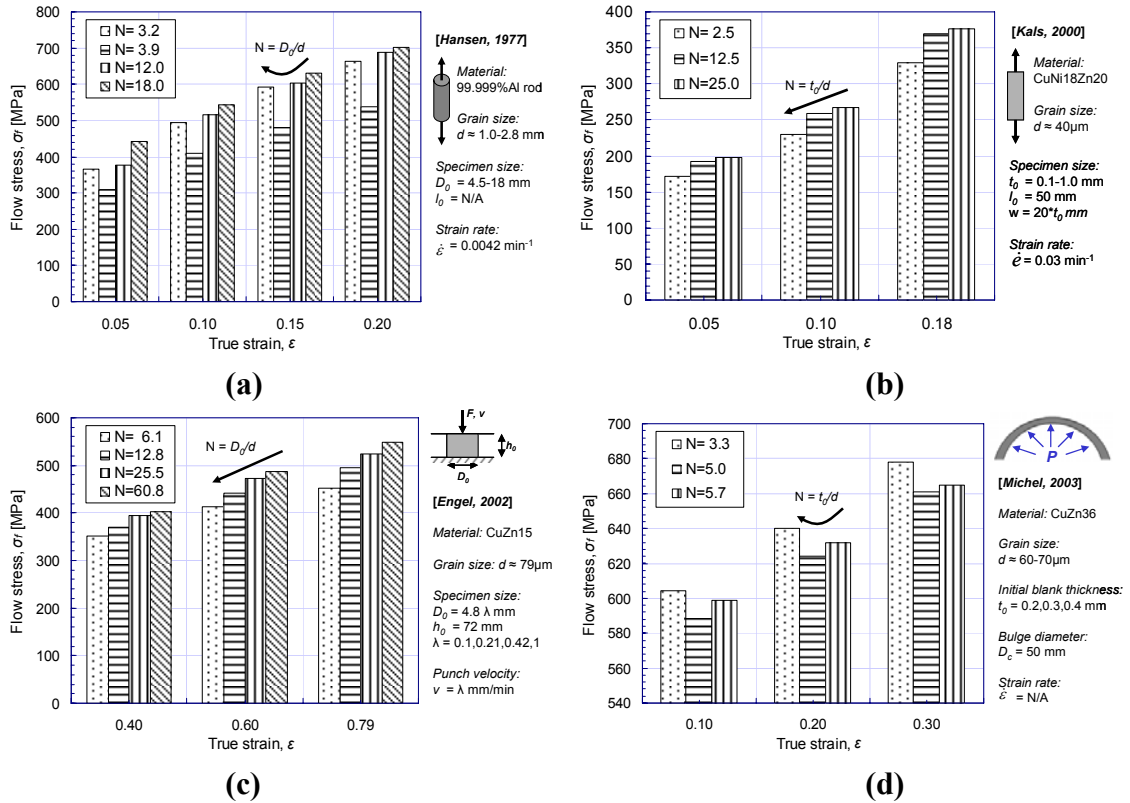


Figure 3-1: Effect of N on material flow stress under different testing conditions

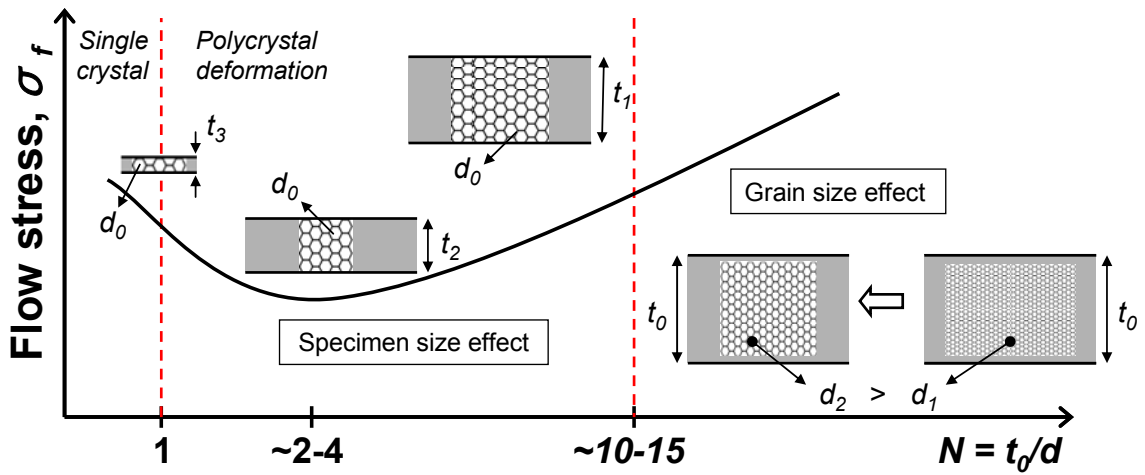


Figure 3-2: Grain vs. specimen size effect on the flow stress as a function of N

3.3 Experimental Setup and Procedure

In this study, the hydraulic bulge testing is selected over the conventional tensile testing because (1) the bulge test can be used to study the effects of both the specimen size (t_0) and the feature size (D_c) as discussed in the previous section, (2) the loading condition within the bulge test (biaxial) is more relevant to the actual state of stress in most metal forming processes, (3) the preparation and handling of the thin sheet specimens is less complicated in the bulge test than the tensile test [Dudderar, 1977; Michel, 2003], (4) material data could be obtained up to high levels of strain; thus, avoiding an excessive extrapolation of the material flow curve in the eventual numerical analysis, and (5) the use of hydraulic pressure instead of a rigid punch leads to a simpler analysis under frictionless conditions. In order to study the grain size effect, thin stainless steel sheets with initial thickness of 51 micrometers were heat treated to vary the grain sizes as will be discussed in the following section. Different sizes of the bulge diameters ($D_c = 2.5 - 100$ mm) were used to investigate the effect of the feature size on the material response. The methodology for computing the material flow stress based on the experimental data of the bulging pressure and the bulge height at the dome apex is also discussed below.

3.3.1 Material Preparation

Due to its availability and excellent properties for various micro-channel applications, such as fuel cells, stainless steel 304 is selected as the material of interest in this study. To study the effect of N , the initial sheet thickness (t_0) was kept constant at 51 micrometers, while the grain size (d) was varied through a heat treating process using

different heating profiles as shown in Figure 3-3a. An electrical furnace with a maximum operating temperature of 1,200°C and programmable heating profile (Figure 3-3b) was used for the heating process. To measure the grain size in the thickness direction of these thin blanks, samples were molded in plastic molding, polished, and electrolytic etched using a 10% oxalic acid. Average grain sizes of the heat treated blanks were measured according to the ASTM Standard E112-88 (i.e., Mean Lineal Intercept or Heyn's method). Three different grain sizes and their corresponding N values are presented in Figure 3-4. As it can be seen, although dramatically different heat treatment profiles were used, the final N values are close to each other (A and C). The variation of the grain size is also shown in Figure 3-5.

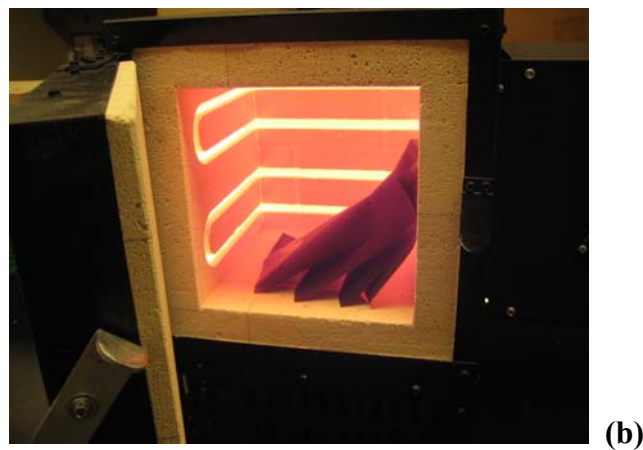
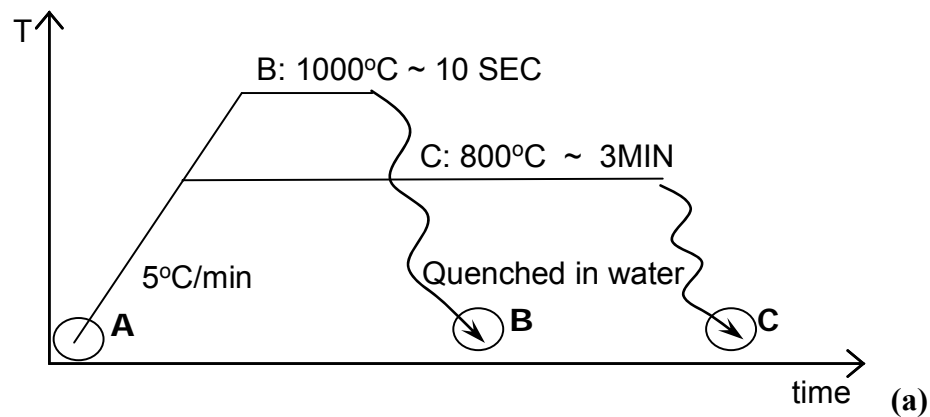
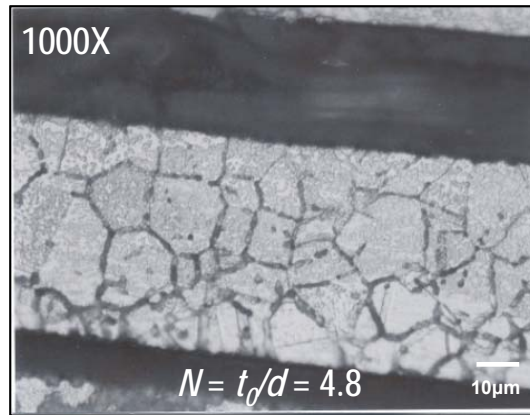
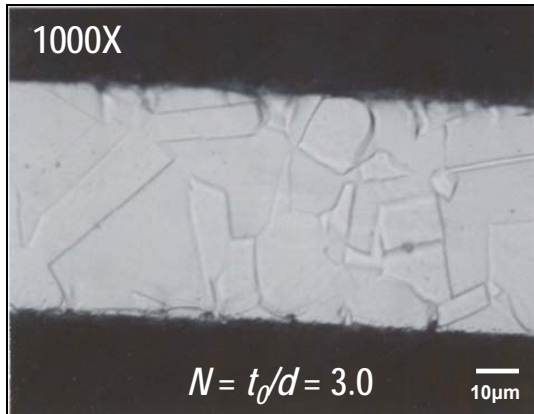


Figure 3-3: Heat treating process – (a) heating profiles, and (b) heating furnace

A: As received $\rightarrow d = 10.6 \mu\text{m}$



B: 1000°C ~ 10SEC $\rightarrow d = 17.0 \mu\text{m}$



C: 800°C ~ 3MIN $\rightarrow d = 9.3 \mu\text{m}$

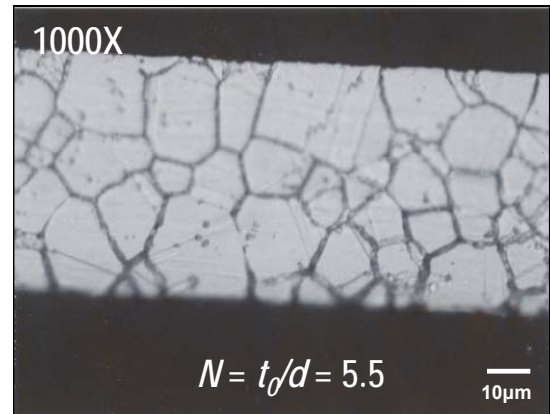


Figure 3-4: Grain size and N values of SS304 blanks, 51 μm -thick

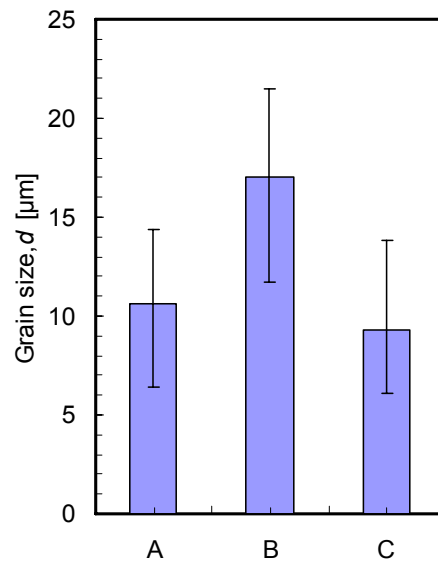


Figure 3-5: Grain size variations

3.3.2 Hydraulic Bulge Test Setup

Hydraulic bulge test apparatus was developed as shown in Figure 3-6. Five different bulge diameters (D_c) of 2.5, 5, 10, 20, and 100 mm were used in order to investigate the effect of the feature size (D_c), and also the effect of M ($M = 49, 98, 196, 392, \text{ and } 1961$) on the material response (i.e. flow stress). The die corner radius (R_c) of the 2.5, 5, 10 and 20 mm bulge diameters was 0.125 mm, and that of the 100 mm bulge die was 6.5 mm. The upper die, the lower die, and the die inserts used in this study were fabricated using turning, drilling, heat-treating, and grinding operations on tool steel materials (D2 and H13). As depicted in Figure 3-6, the blank (7) was placed between the upper and lower dies (1, 2), which were tightly clamped together by threaded bolts (4) around the circumference of the die, assumingly no material was allowed to flow into the die cavity. Copper gaskets (5) were used to provide strong sealing at the contact surfaces between the blank and the lower die. Bulging pressure (6) was injected at the bottom of the lower die. The peak pressure (P) was measured and recorded during each test using a pressure transducer (Omega PX605-3KG). Once the bulging pressure reached the target value, the specimens were removed for the measurement of the dome height (h). A laser measurement system (Keyence LK-G37), Figure 3-7, was used to measure the dome height for the 2.5 and 5 mm samples, while a micrometer was used for the 10 and 20 mm samples. The variations between six specimens bulged under the same test conditions are presented in Figure 3-8, showing the variation of less than 10% with respect to the mean value. As for the 100 mm bulge diameter case, a long-range laser sensor (Keyence LK-G402) was used to continuously measure and record the dome height during the bulge tests and the dome height data was synchronized with the bulging

pressure recorded by the pressure transducer. These measurement values of the pressure (P) and the dome height (h) were later used to compute the material flow curve.

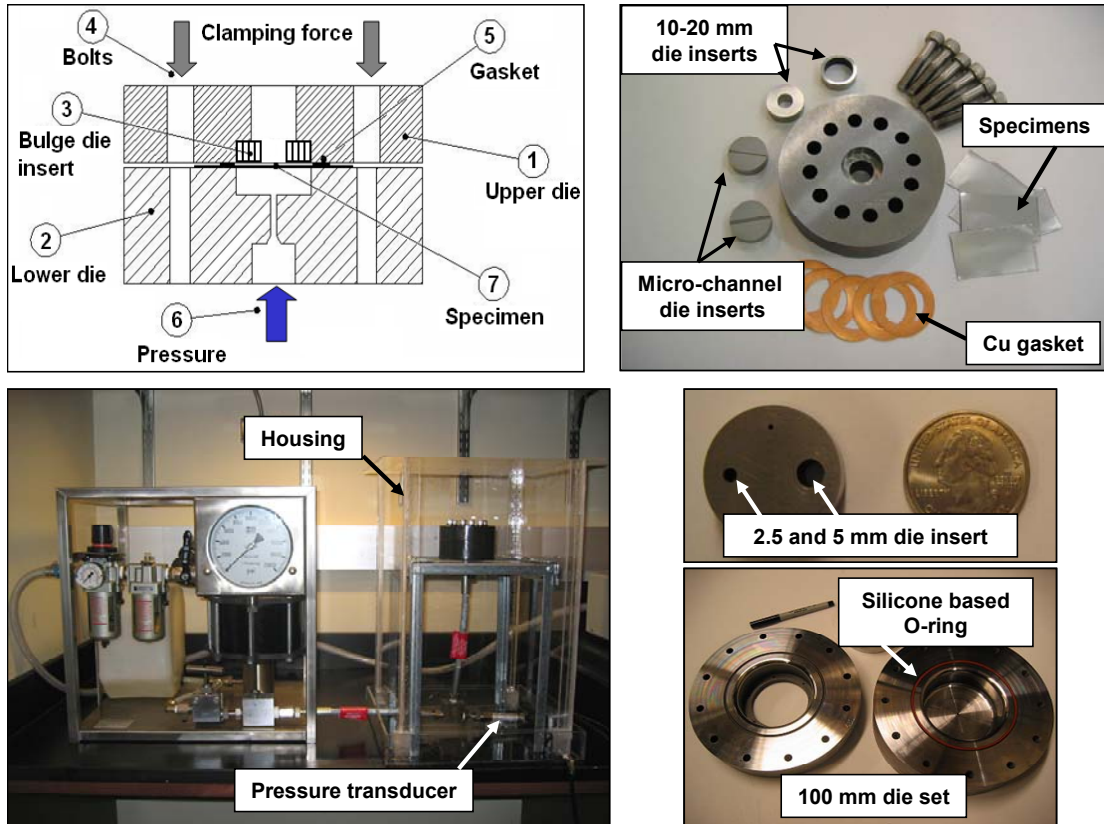


Figure 3-6: Bulge test setup

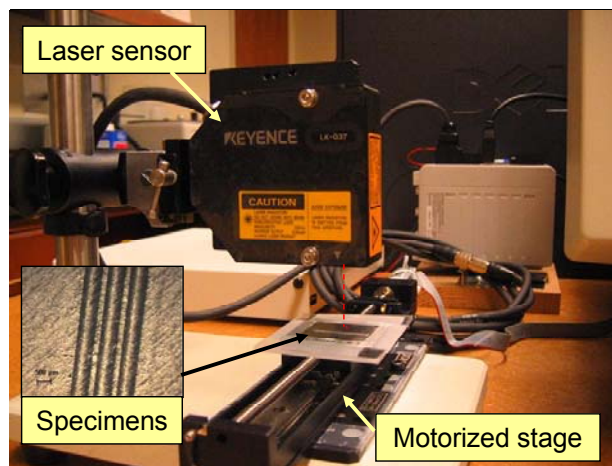


Figure 3-7: Laser measurement system (Keyence LK-G37 laser sensor)

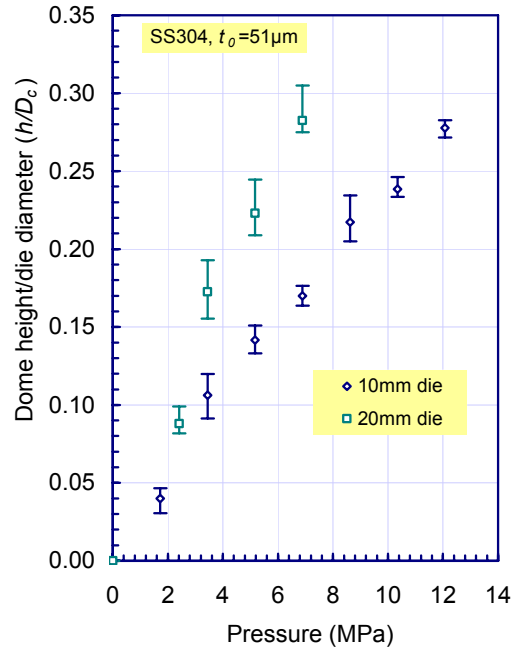


Figure 3-8: Repeatability test of the bulge setup and measurement approach

As a final comment on the bulge test setup, even though the strain rate control during forming/hydroforming operations is known to be an important factor that may affect the overall formability of the blanks, it is also commonly known that the material properties of most metal alloys are not quite sensitive to the strain rate in a cold forming operation as compared to a warm/hot forming processes. Therefore, since all bulge tests are performed at a room temperature in this study, the effect of the strain rate on the material response is not included in the scope of this investigation.

3.3.3 Determination of the Flow Curve

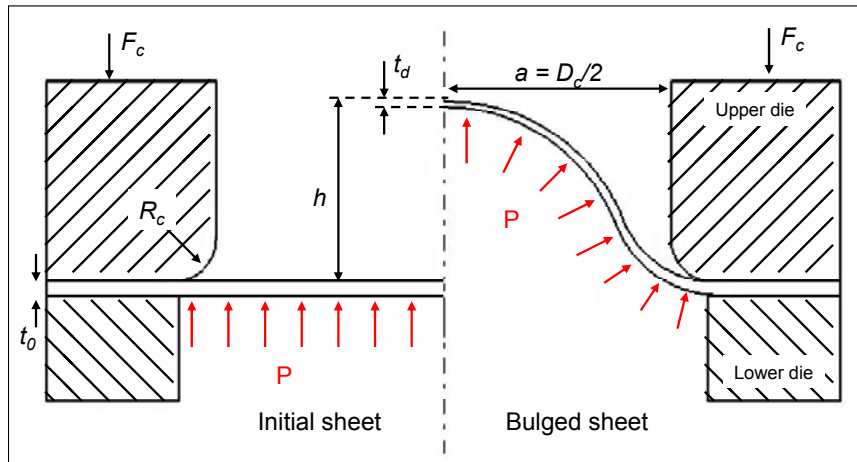


Figure 3-9: Schematic diagram of the bulge setup

A schematic diagram of the bulge test setup is shown in Figure 3-9. The flow stress/curve was basically calculated using the measured values of the bulging pressure (P) and the dome height (h) based on the Hill's theory of plasticity which was derived upon the following assumptions: (1) the bulge shape is spherical, (2) no material is drawn into the die cavity, (3) the sheet is thin and the bending stress could be ignored, (4) the effect of the die corner radius (R_c) is negligible when $R_c < D_c/20$ ($D_c =$ bulge diameter), and (5) the material property is isotropic and follows the von Mises yield criterion. With these assumptions, the equivalent stress ($\bar{\sigma}$) and strain ($\bar{\varepsilon}$), the curvature of the bulge radius (R), and the apex thickness (t_d) could be calculated using the following equations [Hill, 1950]:

$$\bar{\sigma} = \frac{PR}{2t_d} \quad \dots (3-1)$$

$$\bar{\varepsilon} = \ln\left(\frac{t_0}{t_d}\right) \quad \dots (3-2)$$

$$R = \frac{a^2 + h^2}{2h} \quad \dots (3-3)$$

$$t_d = t_0 \left(\frac{a^2}{a^2 + h^2} \right)^2 \quad \dots (3-4)$$

where $a = D_c/2$. Hill also suggested that the calculation of the equivalent strain ($\bar{\varepsilon}$) according to equations (3-2) and (3-4) will only be accurate up to the strain value of 0.4. Therefore, caution should be exercised when attempting to use the calculated flow curve for numerical analysis at strain value higher than 0.4.

The calculation of the apex thickness (t_d) was later modified by Chakrabarty [Chakrabarty, 1970] to include the strain hardening effect (n) since the calculation according to equation (3-4) can be valid only when the material is sufficiently work-hardened. Chakrabarty proposed the following relation for the calculation of the apex thickness:

$$t_d = t_0 \left(\frac{a^2}{a^2 + h^2} \right)^{2-n} \quad \dots (3-5)$$

where n is the strain-hardening exponent.

Another modification to Hill's theory was suggested by Gutscher [Gutscher, 2004] to include the effect of the die corner radius (R_c) in the calculation of the curvature of the bulge radius (R). According to Hill's assumption, the die corner radius effect could be omitted when $R_c \ll D_c/20$. However, when the bulge diameter gets smaller, this effect cannot be neglected which is the case in this study (e.g. in the case of $D_c = 2.5$ mm and $R_c = 0.125$ mm, $D_c/20 = R_c$). Therefore, the calculation of the curvature of the bulge radius (R) in this study was performed using the following equation [Gutscher, 2004]:

$$R = \frac{(a + R_c)^2 + h^2 - 2hR_c}{2h} \quad \dots (3-6)$$

However, an error of larger than 10% was reported when using equation (3-6) to calculate the curvature of the bulge radius (R) for h/a larger than 0.56.

In another study by Dudderar et al. [Dudderar, 1977], they measured the shape of foil samples in the bulge test and found that the shape of the bulge dome was far from being spherical at low values of h/a , especially when $h/a < 0.2$. Therefore, in this study the calculation of the flow stress begins at $h/a = 0.2$ and ends at $h/a = 0.56$ as suggested by Gutscher [Gutscher, 2004]. Finally, since the strain-hardening exponent (n) is an unknown parameter in equation (3-5), iterative calculations are required. A simple iterative calculation loop is constructed to obtain the n value that best describes the data from the experiments according to the power law relation between the stress and strain ($\bar{\sigma} = K\bar{\varepsilon}^n$). The methodology for the flow curve determination based on the bulge test results as discussed in this section is summarized in a flow chart in Figure 3-10.

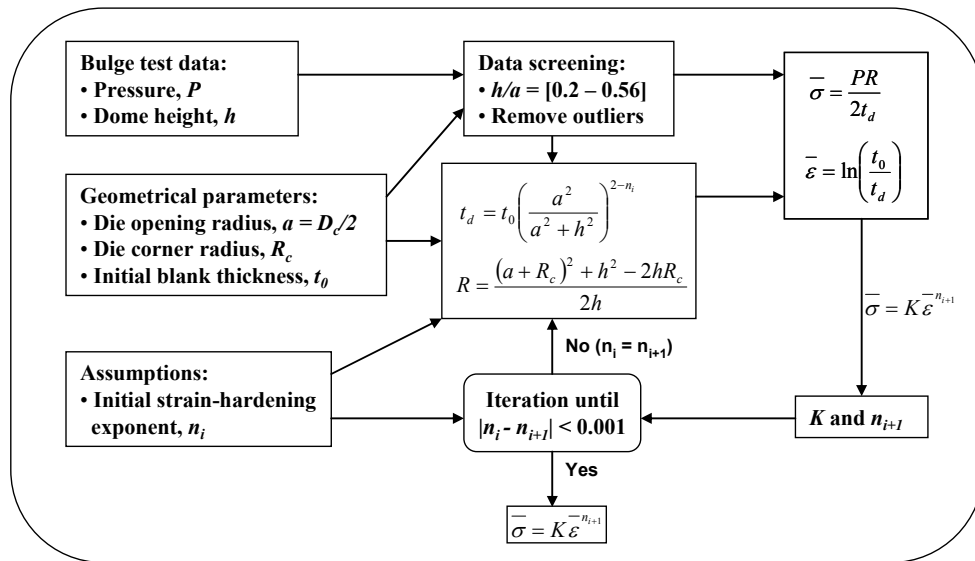


Figure 3-10: Methodology for determination of the material flow curve in hydraulic bulge testing

3.4 Results and Discussion

A series of bulge tests were conducted to study the effects of the grain/specimen size ($N = t_0/d$) and the feature size ($M = D_c/t_0$) on the material flow stress. Thin blanks of SS304, 51 micrometers in thickness, with three different grain sizes of 9.3, 10.6, and 17.0 micrometers ($N = 5.5, 4.8,$ and $3.0,$ respectively) were bulged using five different bulge diameters of 2.5, 5, 10, 20, and 100 mm ($M = 49, 98, 196, 392,$ and $1961,$ respectively). Some of the bulged samples are shown in Figure 3-11. The height of the bulged specimens was then measured using either the laser measurement system (Keyence LK-G37 or LK-G402) or a micrometer. Plots of the dome height (h) as a function of bulging pressure (P) for different grain sizes (d) and bulge diameters (D_c) are presented in Figure 3-12. These pressure and dome height data were then used to calculate the material flow curves. The calculation results of the flow stress in the range of h/a between 0.2 and 0.56 are shown in Figure 3-13.

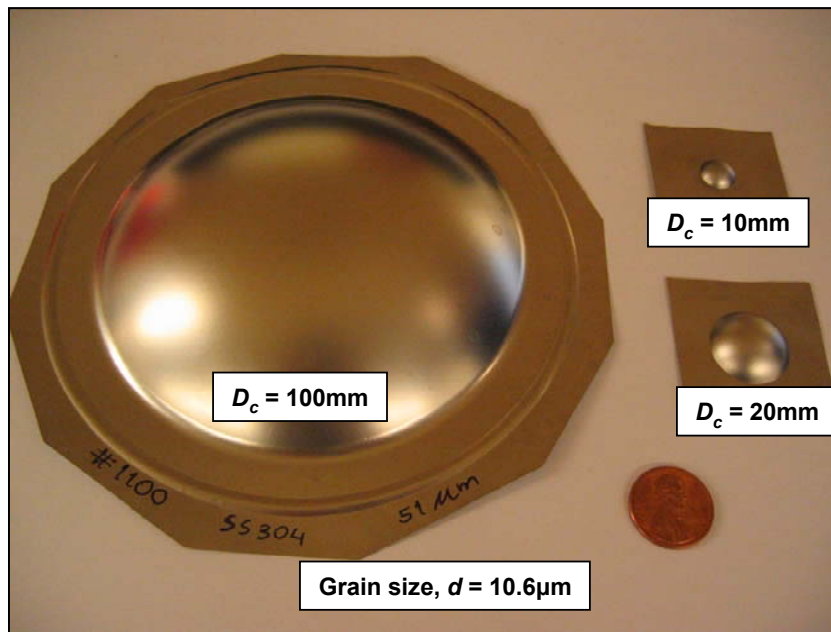
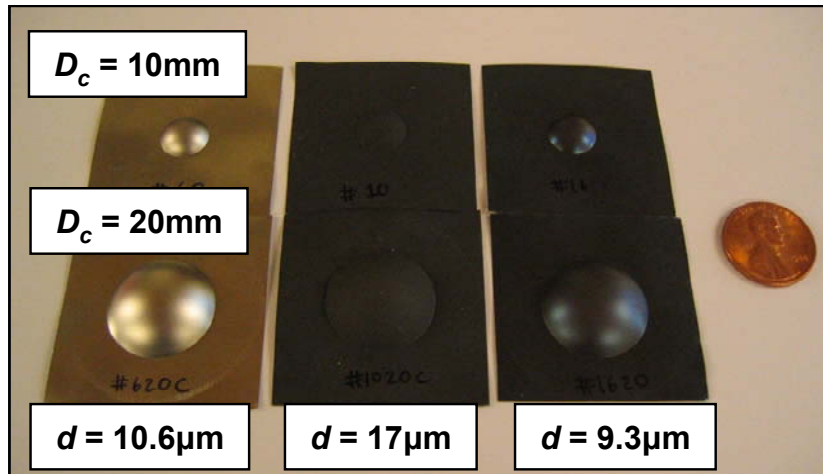
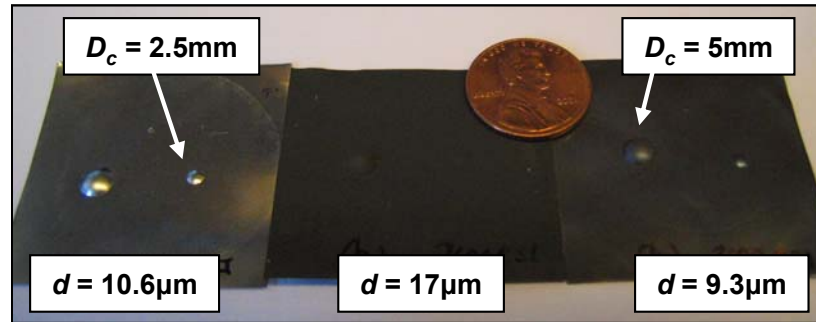


Figure 3-11: Bulged samples of SS304 ($t_0 = 51 \mu\text{m}$) for different grain sizes (d) and bulge diameters (D_c)

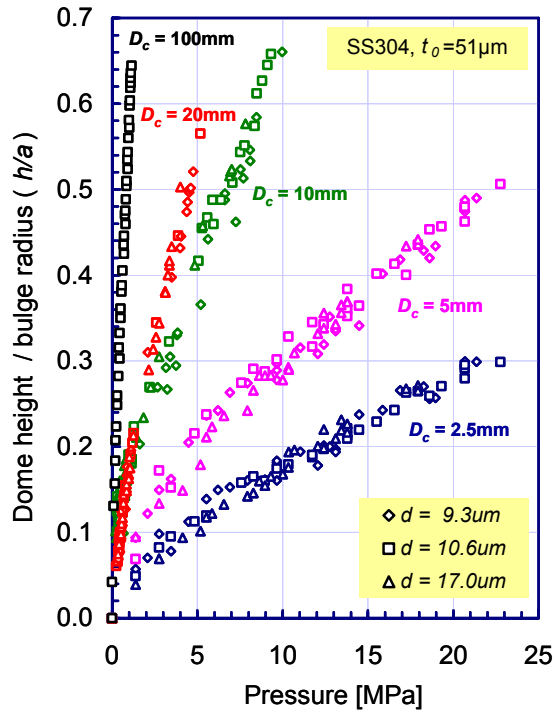


Figure 3-12: Plots of P vs. h/a for different D_c and d sizes

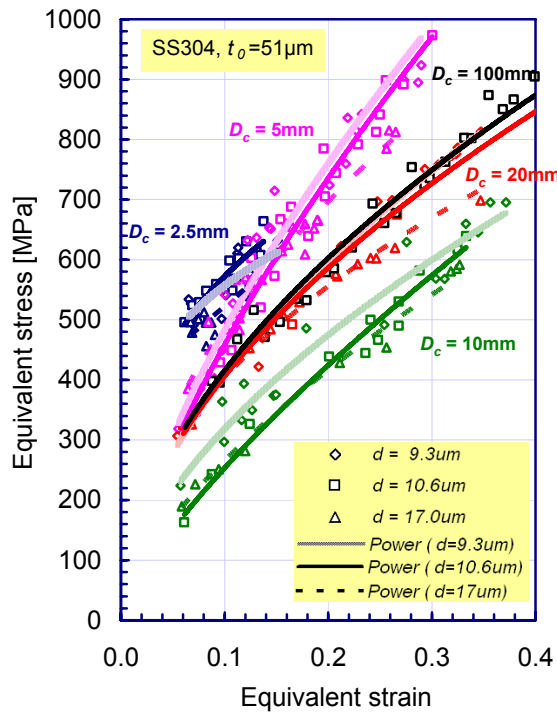


Figure 3-13: Equivalent stress-strain plots for different D_c and d sizes – experimental measurements and curve fit using Power law ($\sigma = K\varepsilon^n$)

Based on the flow curve plots shown in Figure 3-13, the effect of the material grain size could be clearly observed; that is material with larger grain size is weaker, a result that agrees with the Hall-Petch relation. This observation is consistent for all of the bulge diameters with an only exception in the case of the smallest bulge diameter of 2.5 mm. With this bulge diameter (2.5 mm), the 10.6 micrometers grain size showed highest flow stress values. However, this discrepancy may have come from the interactive effects between the grain size and the feature size where the material response is not only dependent on the size of the grains, but also the orientation and defects inside the grains as the feature size becomes smaller. This argument could be reinforced by the observed data scattering in the literature that becomes larger when the feature/specimen size is reduced closer to the grain size. Another cause of this discrepancy may have been from the limited numbers of data points, leading to a rather short flow curve. This happens so because the 2.5 mm bulge diameter is on the same die insert with the 5 mm; therefore, the maximum bulging pressure before bursting is limited by the latter bulge size.

In terms of the feature size (i.e., bulge diameter) effect, the flow curve plots in Figure 3-13 show a decrease in flow curve when the bulge diameter is reduced from 100 mm to 10 mm. This trend is consistent for all grain sizes and agrees well with the results reported by Michel et al. [*Michel, 2003*]. However, as the bulge diameter is reduced further from 10 mm down to 2.5 mm, an inverse trend was observed; that is, higher flow curves were observed when the 2.5 and 5 mm bulge diameters were used. The increase in flow stress with decreasing bulge diameter below 10 mm is understandable and expected because in general a higher bulging pressure would be

required to form smaller feature sizes (i.e., bulge diameter) or fill sharp corner radii. As a result, the material response should demonstrate higher strength when attempting to form smaller features/parts.

Finally, the material flow curves in Figure 3-13 could be described by the Power Law relation: $\bar{\sigma} = K \bar{\varepsilon}^n$ with the corresponding K and n values shown in Table 3-2 for different values of d and D_c (i.e., N and M).

d (μm)	$N = t_0/d$	$M=49$ (2.5 mm die)		$M=98$ (5 mm die)		$M=196$ (10 mm die)		$M=392$ (20 mm die)		$M=1,961$ (100 mm die)	
		K [MPa]	n	K [MPa]	n	K [MPa]	n	K [MPa]	n	K [MPa]	n
17.0	3.0	941	0.26	1,588	0.51	1,184	0.65	1,166	0.46	-	-
10.6	4.8	1,325	0.39	2,207	0.68	1,406	0.74	1,375	0.53	1,428	0.54
9.3	5.5	948	0.23	2,177	0.65	1,199	0.58	1,454	0.55	-	-

Table 3-2: K and n values for SS304 with $t_0 = 51 \mu\text{m}$

In order to compare the observed size effects in this study to other materials and tests in the literature, the characteristic parameters (N and M) are employed to show the effect of the grain, specimen, and feature size, as well as their interactions on the flow stress. The results are summarized in Figure 3-14.

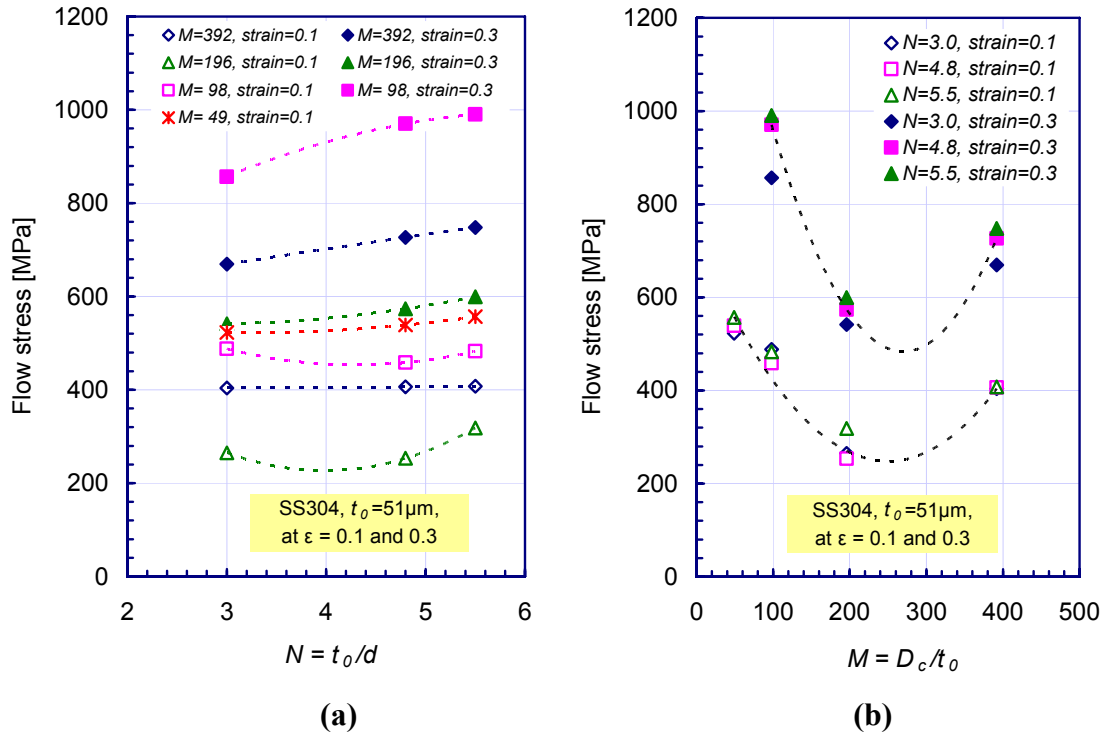


Figure 3-14: Effect of (a) specimen/grain size (N), and (b) feature/specimen size (M) on material flow stress at two strain levels ($\epsilon = 0.1$ and 0.3)

Recall from Figure 3-2 that the flow stress has been reported in the literature to decrease with decreasing N value down to about 2-4, after which the flow stress starts to climb up as N decreases further as observed by others [Hansen, 1977; Kals, 2000; Raulea, 2001; Michel, 2003]. For the range of N used in this study (3.0 – 5.5), the flow stress appeared to continuously decrease with decreasing N value (Figure 3-14a) at the strain level of 0.3. However, this trend is shown to be slightly different at the strain value of 0.1 where a small increase in the flow stress value is observed in certain cases of M values as N was reduced from 4.8 to 3.0 as shown in Figure 3-14a.

On the other hand, the effect of the feature/specimen size (M) on the material flow stress as shown in Figure 3-14b is a new discovery that has not been reported in any previous studies in the literature. Surprisingly, the effect of M on the flow stress is

shown to also have a critical point, similar to the observed phenomena in the experiments reported in the literature as summarized in Figure 3-2, where the effect is inverted after this critical value. For the thin stainless steel 304 sheets with initial thickness of 51 micrometers and three different grain sizes (9.3 – 17.0 μm) that are in this study, this critical M value is found to fall between 100 and 200. In other words, when M is reduced below 200, the forming force or pressure would be expected to increase significantly.

In addition, further analysis was performed to evaluate the significance of the strain-hardening effect (n) on the flow stress calculation. In other words, if equation (3-4) was used to calculate the apex thickness (t_d) instead of equation (3-5), different flow stress values would be obtained. Recall that equation (3-4) was derived based on the assumption that the material is fully work-hardened prior to the bulging test; and thus, the strain-hardening effect is negligible. The results of the calculation using equation (3-4) are plotted in Figure 3-15 with the corresponding K and n values shown in Table 3-3. As it can be seen in Figure 3-15, the effect of the strain-hardening on the flow stress calculation is significant and should not be neglected. This effect is found to become even more significant in the case of smaller bulge diameters.

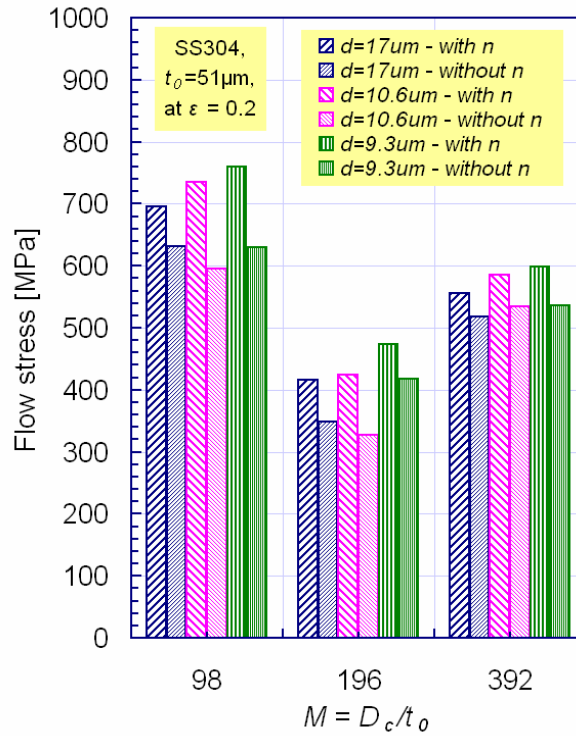


Figure 3-15: Comparison of flow stress calculations with and without strain-hardening effect (n) for different M and d sizes at $\epsilon = 0.2$

d (μm)	$N = t_o/d$	$M=49$ (2.5 mm die)		$M=98$ (5 mm die)		$M=196$ (10 mm die)		$M=392$ (20 mm die)		$M=1,961$ (100 mm die)	
		K [MPa]	n	K [MPa]	n	K [MPa]	n	K [MPa]	n	K [MPa]	n
17.0	3.0	950	0.27	1,561	0.56	1,126	0.73	1,178	0.51	-	-
10.6	4.8	1,325	0.39	2,033	0.76	1,265	0.84	1,380	0.59	1,433	0.60
9.3	5.5	962	0.24	2,030	0.73	1,189	0.65	1,438	0.61	-	-

Table 3-3: K and n values without considering strain-hardening effect

3.5 Qualitative Model Explaining the Size Effects

One of the most widely accepted theories used for explaining the size effects is the “surface layer model”, Figure 3-16 [Kals, 1996]. The surface layer model simply states that the surface grains are less hardening and the share of this surface grain increases with a decrease in specimen size; thus, lowering the material strength.

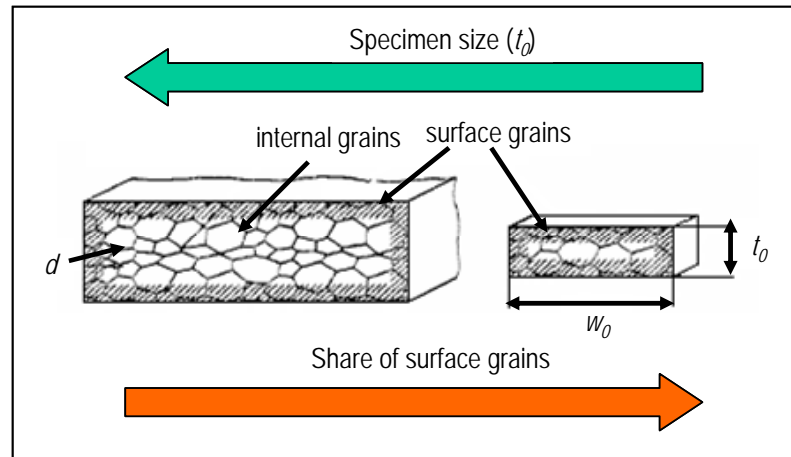


Figure 3-16: Surface layer model [after Kals, 1996]

The ratio between the surface grains to the internal grains was calculated according to the following equation:

$$\alpha = 1 - \frac{(w_0 - 2d)(t_0 - 2d)}{w_0 t_0} \quad \dots (3-7)$$

where α = the share of surface grain, w_0 = specimen width, t_0 = specimen thickness, and d = material grain size. According to studies by Michel and Tseng [Michel, 2003; Tseng, 1990], the effect of the specimen width (w_0) on the material flow curve was found to be insignificant. Therefore, the characteristic dimension of the specimen is the thickness (t_0) in thin sheet based micro-forming application. Extending the surface layer model to a section on a bulge sample (Figure 3-17), the share of the surface grain could be calculated using equation (3-8).

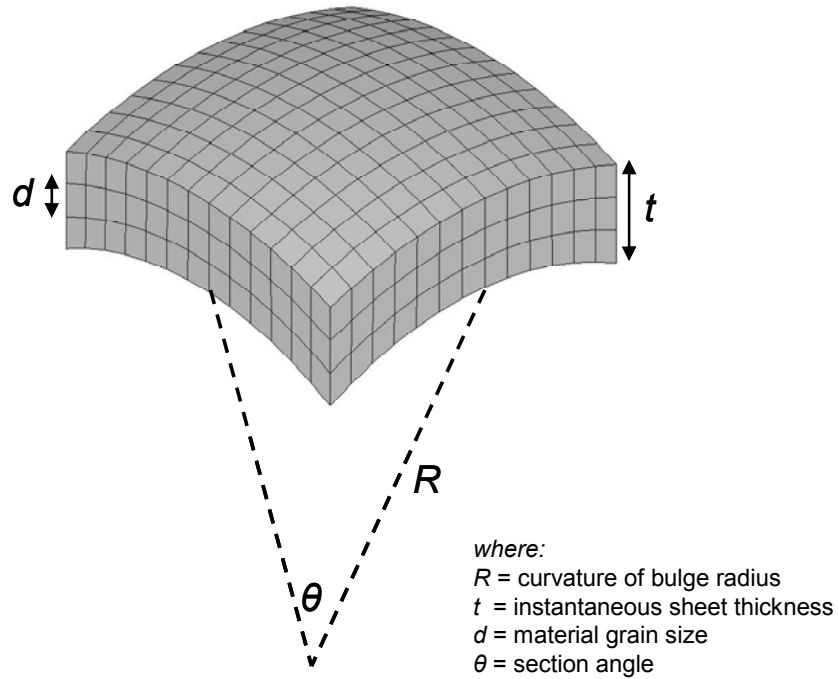


Figure 3-17: Section on a bulge sample

$$\alpha = 1 - \frac{(R\theta - 2d)(t - 2d)}{R\theta t} \quad \dots (3-8)$$

Substituting t/d by N and assuming $d \ll R\theta$, the relationship between α and N could be approximated by the following relation:

$$\alpha \approx \frac{2}{N} \quad \dots (3-9)$$

The relationship in equation (3-9) is plotted in Figure 3-18. The value of α is shown to increase exponentially as N decreases (t_0 decreases and/or d increases) and would result in a decrease in the flow stress. The bulge test results in this study are shown to agree well with this explanation.

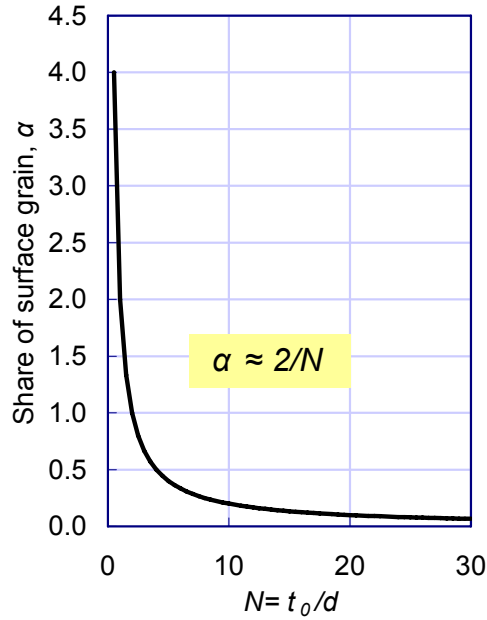


Figure 3-18: Relationships between N and α

Next, the surface layer model was applied to explain the effect of the feature size (M). For simplicity, let us consider the case where we have a perfect hemisphere (i.e., the curvature of the bulge radius $R = a = D_c/2$). Recall that $M = D_c/t$, so $R = (M \cdot t)/2$. Substituting this relationship between R and M into equation (3-8), we obtained:

$$\alpha \approx \frac{4d}{t} \cdot \frac{1}{\theta M} + \frac{2d}{t} - \frac{8d^2}{t^2} \cdot \frac{1}{\theta M} \quad \dots (3-10)$$

Substituting $\frac{t}{d} = N \approx \frac{2}{\alpha}$ in equation (3-10), we obtained $\alpha \approx 1$. This would mean that the surface layer model could not be applied to explain the deviation in material response when the feature size (M or D_c) changes as observed in the bulge test results. In the flow curve calculations, the feature size effect (M) is shown to have a significant impact on the material flow stress. Therefore, the surface layer model failed to explain the effect of the feature size (M) on the material flow stress, even just in a qualitative sense.

As a result, a new material model is put forward in this section to qualitatively explain the feature size effect (M) as observed in the bulge test results. According to the Hall-Petch relation, the material is predicted to be stronger when the grain size is reduced. It happens so because of the increasing number of the internal grain boundaries which prevents the free movement of the dislocations. In other words, with the same volume, the material which has higher number of the internal grain boundaries is predicted to have a higher strength (flow stress). With this concept, the ratio between the internal grain boundary length and the volume ($GB_L/Volume$) is proposed to be used as an index value to represent the material strength. The calculation of this ratio ($GB_L/Volume$) in a bulge test can be carried out using the following equation:

$$\frac{GB_L}{Volume} = \frac{2MN(MN-1)(N-1) + N(MN-1)^2}{M^2 N^3} \quad \dots (3-11)$$

where $M = D_c/t_0$, and $N = t_0/d$. In the bulge test, D_c represents the bulge diameter, t_0 is the initial blank thickness, and d is the average grain size of the material. Equation (3-11) was derived based on a cubical grain geometry which has the volume of d^3 . Samples of the calculation are shown in Table 3-4. The plot of $GB_L/Volume$ for different N and M combinations is shown in Figure 3-19. As can be seen, the $GB_L/Volume$ ratio does not vary much for a large value of M , indicating no significant feature size effect at the macro-scales. However, substantial change of this ratio could be observed as M is reduced close to about 50. This effect is amplified by small N values as the size of the specimen is reduced close to the size of the grain (i.e., N reduces to 1). Based on this qualitative model, the $GB_L/Volume$ ratio would decrease with decreasing N and M values, leading to lower flow stress values as observed in the bulge test results in this study when N decreases from 5.5 to 3.0 and M from 1,961 to 196 (i.e.,

D_c from 100 mm to 10 mm). However, this qualitative model would fail to explain the observed increase in the flow stress value as M decreases from 196 to 49 (i.e., D_c from 10 mm to 2.5 mm). Therefore, the proposed qualitative model could only be used to explain the results from the bulge tests when $M > 200$. In the next section, another material model is put forward with an attempt to quantify the effect of N and M on the material flow stress when $M < 200$.

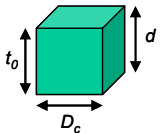
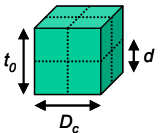
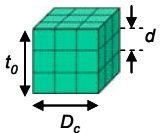
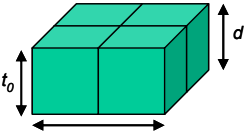
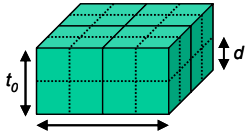
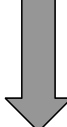
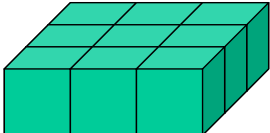

	$N = 1$	$N = 2$	$N = 3$
$M = 1$	 $GB_L/Volume = 0$	 $GB_L/Volume = 6/8$	 $GB_L/Volume = 36/27$
$M = 2$	 $GB_L/Volume = 1/4$	 $GB_L/Volume = 42/32$	
$M = 3$	 $GB_L/Volume = 4/9$		<div style="border: 1px solid black; padding: 5px; width: fit-content; margin: 0 auto;"> $\frac{GB_L}{Volume} = \frac{2MN(MN-1)(N-1) + N(MN-1)^2}{M^2 N^3}$ </div>

Table 3-4: Calculation of internal grain boundary length per unit volume ($GB_L/Volume$)

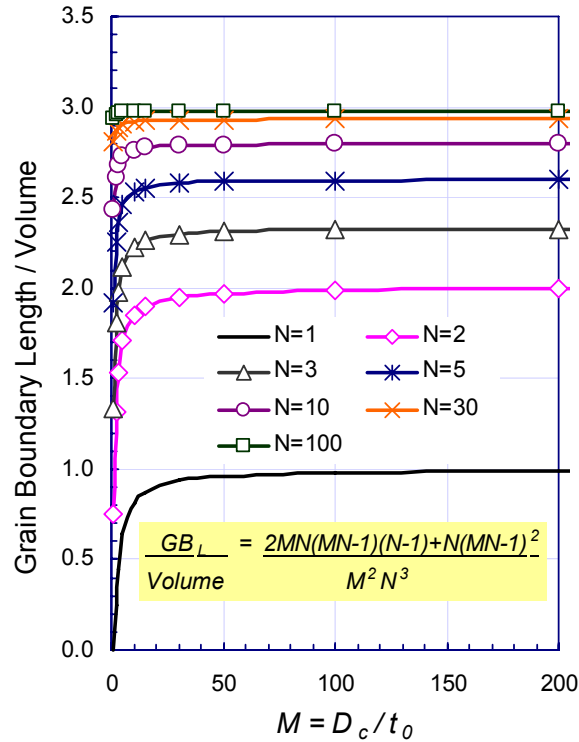


Figure 3-19: Grain boundary length per unit volume for different N and M combinations

3.6 Quantitative Model Explaining the Size Effects

In this section, another material model is developed with an attempt to quantify the magnitude of the size effects (N and M) on the material flow stress (σ_f) when $M < 200$. The model specifically correlates N and M values to σ_f based on the Hall-Petch relation, the Hill's theory of plasticity, and the relationship between the strain-hardening coefficient (n) and σ_f according to the material power law. Based on these relationships and theories, the correlation between the size effects (N and M), the strain hardening effect (n), and the material flow stress (σ_f) can be presented in the following fashion:

Hall-Petch relation:

$$\sigma_f = \sigma_0 + \frac{k}{\sqrt{d}} = \sigma_0 + \frac{k}{\sqrt{t_0}} \sqrt{N} \longrightarrow \sigma \propto \sqrt{N} \quad \dots (3-12)$$

Hill's theory:

$$\bar{\sigma} = \frac{PR}{2t_d} = \frac{P\left(\frac{a^2 + h^2}{2h}\right)}{2\left(\frac{t_0}{e^\varepsilon}\right)} \longrightarrow \bar{\sigma} \propto \left(\frac{a^2}{e^\varepsilon}\right) = \left(\frac{D_c^2}{e^\varepsilon}\right) = \left(\frac{M^2}{e^\varepsilon}\right) \quad \dots (3-13)$$

Power law:

$$\sigma_f = K\varepsilon^n \longrightarrow \sigma \propto \varepsilon^n \quad \dots (3-14)$$

Based on the above equations (3-12) to (3-14), combining the effect of the grain size (d), the specimen size (t_0), the feature size (D_c), and the strain-hardening effect (n) on the material flow stress (σ_f) would yield following correlation between N , M , n and σ_f as follows:

$$\sigma_f = \left(a + b\sqrt{N} + c\frac{M^2}{e^\varepsilon}\right)\varepsilon^n \quad \dots (3-15)$$

When applying the calculation in equation (3-15) to the flow curves obtained from the bulge tests for $N = 3.0-5.5$, and $M = 49-196$, the constants a , b , c , and n were found to be $a = 1,658$, $b = 148.2$, $c = -0.02973$, and $n = 0.5436$. The flow curve comparison between the experiment and the calculation in equation (3-15) is presented in Figure 3-20.

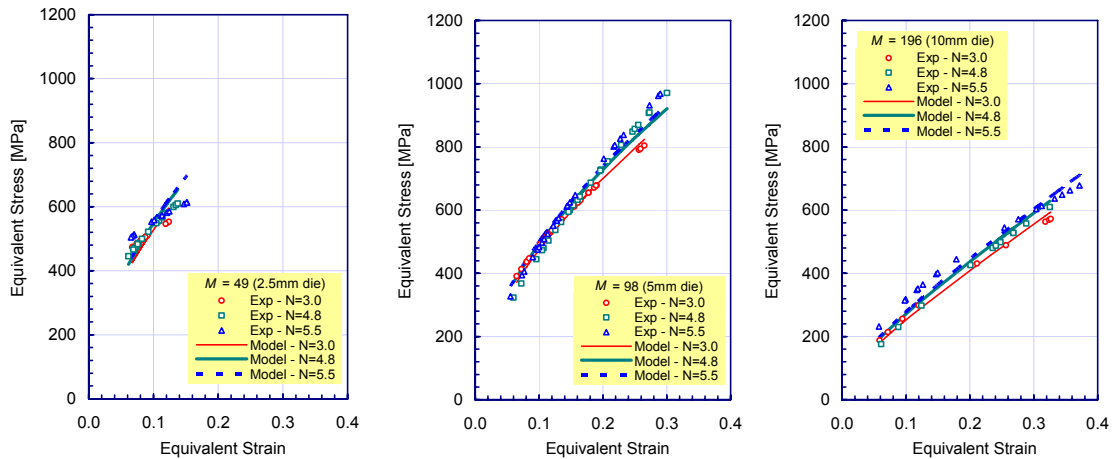


Figure 3-20: Flow curves comparison between experiment and proposed model

Based on the plots in Figure 3-20, the proposed material model in equation (3-15) shows good predictions of the flow curve when compared to the experimental results. In addition, this model was further applied to another set of bulge test results as reported in [Michel, 2003]. In that study, a bulge diameter of 50 mm was used to bulge CuZn36 blanks with three different thicknesses of 0.2, 0.3, and 0.4 mm ($M = 250, 167, \text{ and } 125$, respectively). The average grain size of the blanks with the sheet thickness values of 0.2 and 0.3 was 60 micrometers, and that of the 0.4 mm thick blanks was 70 micrometers, corresponding to N values of 3.3, 5.0, and 5.7, respectively. The calculation in equation (3-15) was then applied to analyze the bulge test results. The flow stress comparison between the experimental values and the ones obtained based on the calculation in equation (3-15) for different combinations of N and M values is shown in Figure 3-21 with the material constants ($a, b, c, \text{ and } n$) listed next to the plot. The calculation in equation (3-15) was shown to be capable of capturing the effect of N and M on σ_f . Therefore, it is reasonable to state that equation (3-15) represents a legitimate calculation between the grain, specimen, and feature sizes (N and M) and the flow stress (σ_f). Once the material constants ($a, b, c, \text{ and } n$) are identified based on actual material testing data (i.e. reasonable range of N and M values), this calculation could then be used to predict the material flow curve in the similar range of the N and M domains without having to conduct the material testing again when there are changes in either material grain size, blank thickness, or feature size, in the microforming processes.

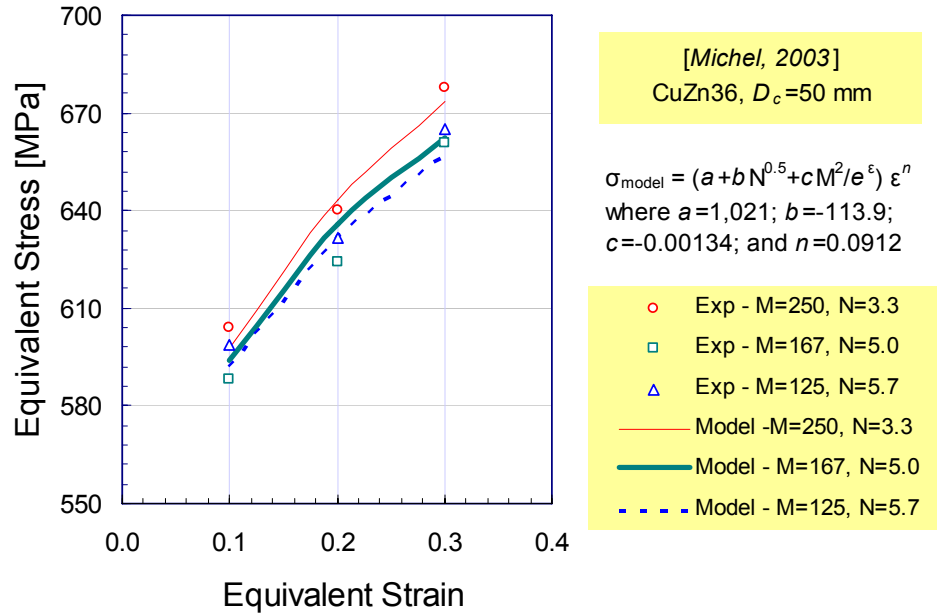


Figure 3-21: Flow stress comparison between bulge test results [Michel, 2003] and proposed model for different N and M combinations

3.7 Summary and Conclusions

In this study, the hydraulic bulge test was used to investigate the size effects – the grain/specimen size effect ($N = t_0/d$) and the feature/specimen size effect ($M = D_c/t_0$), on the material flow curve of thin SS304 sheet with an initial blank thickness of 51 micrometers. To study the effect of the grain/specimen size (N), the material grain size (d) of SS304 blanks was varied through a heat treating process. Three values of grain sizes of 17.0, 10.6, and 9.3 micrometers were obtained, corresponding to the N values of 3.0, 4.8, and 5.5. To study the effect of the feature size (M), five bulge diameters (D_c) of 2.5, 5, 10, 20, and 100 mm were used, corresponding to the M values of 59, 98, 196, 392, and 1,961, respectively. Based on the bulging pressure and the dome height data, the material flow curve was calculated based on the methodology discussed in section 3.3.3, which taken the die corner radius (R_d) and the strain-hardening (n) effects into

consideration. It was shown that these effects are crucial to the flow stress calculation, especially when the feature size (i.e., bulge diameter) is small; and thus, should not be ignored. Based on the flow stress calculations, the flow curves were constructed for each combination of N and M values. The results showed that the flow stress would decrease with decreasing N values from 5.5 to 3.0 for all bulge sizes, and the flow stress would also decrease with decreasing M values from 1,961 to 196, after which the flow stress was found to increase with a further decrease of M value (from $M = 196$ to $M = 49$). This observed phenomenon is understandable as higher pressure/force values would generally be required in hydroforming of smaller feature sizes, given the specimen thickness and material grain size are kept constant. In addition, the increase in the material flow stress when $N < 4$ as reported in several literatures was not observed in this study.

The surface layer model was discussed and shown to only be applicable to explain the grain/specimen size effects (N), but not the feature size effect (M). Therefore, new material models were proposed to explain the latter effect on the flow stress both qualitatively and quantitatively. By using the total grain boundary length per unit volume (GB_L/Volume) as the material strength index (i.e., higher GB_L/Volume value indicates stronger material), the feature size effect on the flow stress as observed from the bulge test results when the bulge diameter was decreased from 100 to 10 mm (M from 1,961 to 196) could very well be explained and understood. However, this GB_L/Volume ratio failed to explain the size effect when $M < 196$. Therefore, another material model was proposed to specifically correlate the size effect characteristic parameters (N and M) and the strain-hardening effect (n) to the flow stress (σ_f) calculation. This model was

derived based on a superposition of Hall-Petch equation (d or N), Hill's theory of plasticity (D_c or M , and ε), and the material power law (n) as shown in equation (3-15). The calculation between N , M , n , and σ_f as proposed in this model was applied to the bulge test results in this study as well as in the literature for different N and M values, and different materials. The result comparisons showed that the proposed calculation in equation (3-15) is a legitimate model, capable of capturing and including the size effect parameters (N , M) and strain-hardening exponent (n) on the material flow stress (σ_f). The material constants (a , b , c , and n) in equation (3-15) are needed to be identified based on a reliable and adequate results from the experiments. Once the constants are known, the model could provide a tool for rapid prediction of the material flow curves at various N or M combinations that are still within the similar range to the experiments that are conducted to identify the material constants. This study can also be found in the Journal of Machine Tool and Manufacturing [*Mahabunphachai, 2008*].

CHAPTER 4: HYDROFORMING OF MICRO-CHANNEL ARRAYS – PROCESS CHARACTERIZATION AND CHANNEL DESIGN GUIDELINES

4.1 Introduction

Micro-feature (micro-channel, micro-protrusion, micro-cavity, etc.) arrays on large area-thin metallic sheet alloys are increasingly needed for compact and integrated heat/mass transfer applications that require high temperature resistance, corrosion resistance, good electrical/thermal conductivity, etc. Such applications include bipolar/interconnect plates for fuel cells (PEMFC, SOFC, MOFC), fuel reformers/processors, micro-power generators, micro-reactors, micro-heat exchangers, micro-turbines, etc., Figure 4-1. Apparently, channel geometry, size, and configuration have a great influence on the ultimate functionality of the channel arrays such as mass transportation and heat transfer [Kumar, 2003; Cha, 2004]. In this chapter, the manufacturability aspect of such micro-feature arrays is investigated in order to determine the design limitations and identify challenges of making micro-channels with desired shape and configuration for given applications. Examples of existing manufacturing methods of micro-feature arrays on thin metallic sheet alloys include (a) stamping of stainless steel sheets as shown in Figure 4-1a [Allen, 2000], (b) photo etching of stainless steel/titanium plates as shown in Figure 4-1b [Tech-etch, Inc.], (c) Lithography Galvanik Abformung (LIGA) with electroforming of stainless steel plate [Lee, 2005], and (d) hydroforming of pure copper and stainless steel foils [Joo, 2004].

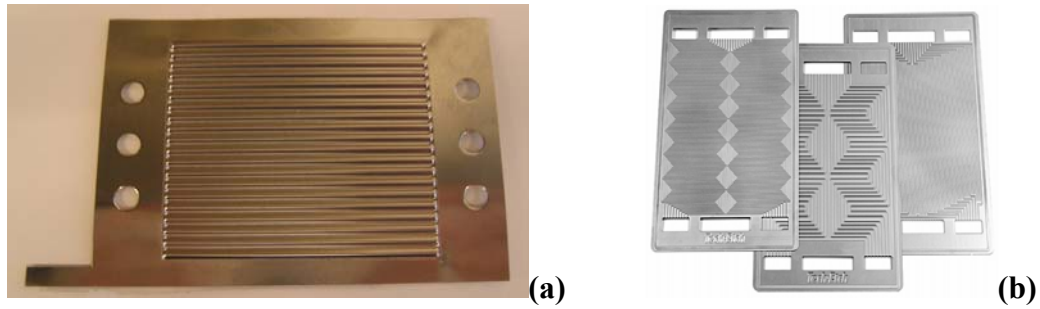


Figure 4-1: Micro-feature arrays on thin metallic sheet for PEMFC fabricated by (a) stamping [*GenCell Corp.*], and (b) photo etching [*Tech-etch, Inc.*]

Among existing manufacturing processes of micro-feature arrays on initial flat thin metallic sheet, the hydroforming process stands out as a prominent candidate, especially at a large-scale production, due to various advantages in terms of the simplicity of the process setup, superior surface topology, uniform thickness distribution, and higher formability of the final parts under the bi-axial loading and frictionless conditions. Therefore, the first half of this chapter is dedicated to study the hydroformability of the micro-channels using thin stainless steel sheet. In addition to the process producibility study, the so-called “size effects” on the material behavior are also investigated to understand if and to what extent they affect the formability of thin metallic sheets into micro-channels. In doing so, hydroforming experiments are conducted using thin stainless steel 304 blanks of 0.051 mm thick with different grain sizes of 9.3, 10.6, and 17.0 micrometers into several channel geometries ranging from 0.46 to 1.33 mm in width and from 0.15 to 0.98 mm in height. In the second part of this chapter, the focus of the study is placed on the establishment of design guidelines for the micro-channel hydroforming technique for robust mass production conditions through a set of parametric studies.

In the following two sections, the hydroforming experimental set up and conditions are presented, followed by the discussion of the experimental results. In the fourth section, the finite element (FE) models of the process are developed and validated with the micro-channel experiments based on several material flow curves obtained from the hydraulic bulge tests and proposed material model in the previous chapter. In the fifth section, the validated FE models are used to conduct a parametric study to establish design guidelines. These design guidelines are expected to minimize the trial-and-error procedures when designing and fabricating micro-channel array devices to result in optimal dimensions or shapes for different applications.

4.2 Experimental Setup

An experimental apparatus for thin sheet hydroforming was developed as shown in Figure 4-2. The setup is composed of an upper die (1) that has an opening at the middle with a shoulder to allow the use of different die inserts (3), a lower die (2) that has an opening at the bottom for the pressure injection, threaded bolts (4) to provide clamping force, and copper gaskets (5) to provide sealing. Three different micro-channels die inserts, namely 1-channel die, 3-channel die, and 6-channel die as shown in Figure 4-3, with channel dimensions between 0.46 and 1.33 mm in width, and 0.15 to 0.98 mm in height, were used in this study. Detailed geometries of the micro-channels on each die insert could be found in Table 4-1. The forming pressure was measured and recorded using a pressure transducer (Omega PX605), while the formed micro-channel profiles were measured using a laser sensor (Keyence LK-G37), Figure 4-4.

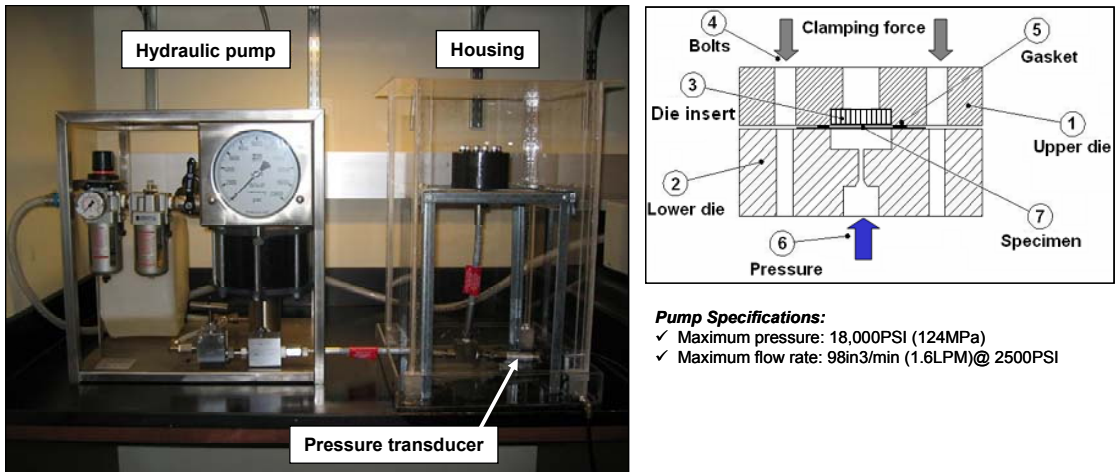


Figure 4-2: Hydroforming process apparatus

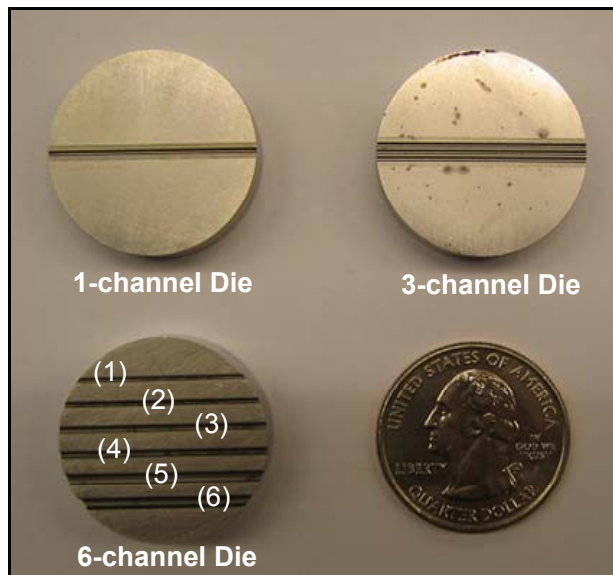
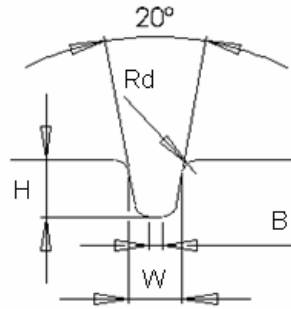


Figure 4-3: Die inserts: 1-channel, 3-channel, and 6-channel dies



Dimensions of each die insert [mm]								
Feature	1 Channel	3 Channels	6 Channels					
			#1	#2	#3	#4	#5	#6
W	0.46	0.46	0.52	0.63	0.78	0.78	1.33	1.33
H	0.50	0.50	0.15	0.24	0.24	0.46	0.46	0.98
Rd	0.13	0.13	N/A	N/A	N/A	0.13	0.26	0.26
B	0.11	0.11	N/A	N/A	N/A	N/A	N/A	N/A
Channel spacing*	N/A	0.82	3.00	3.00	3.00	3.00	3.00	3.00

* Distance measured from center to center of adjacent channels
All channels have 10° draft angle

Table 4-1: Micro-channel geometries on different die inserts

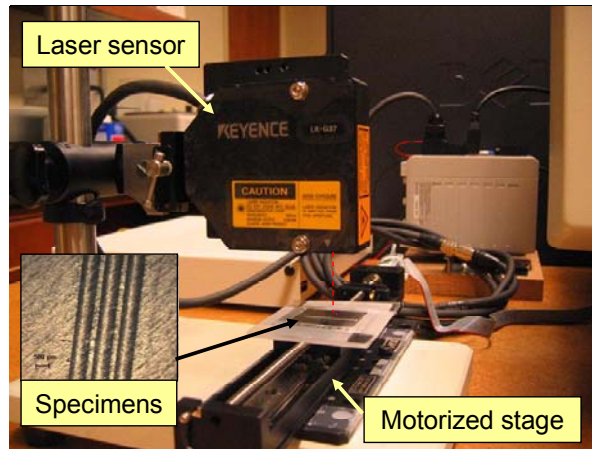


Figure 4-4: Laser measurement system (Keyence LK-G37 laser sensor)

4.3 Experimental Results and Discussion

The first set of the hydroforming experiments were performed on thin blanks of SS304 in the as-received condition (grain size = 10.6 μm) using all three die inserts to evaluate the process repeatability. Samples of hydroformed micro-channels are shown in Figure 4-5. The measured micro-channel profiles for hydroformed specimens at

different pressure levels of 55.2 and 82.7 MPa (8,000 and 12,000 PSI) are presented in Figure 4-6. The measurement results showed good process repeatability on all three die inserts with a maximum variation in the channel height of less than 20 micrometers.

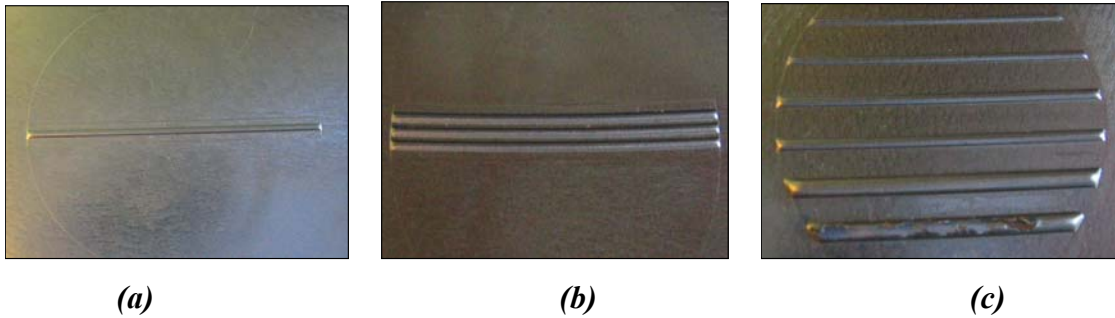


Figure 4-5: Samples of hydroformed micro-channels on SS304, 0.051mm-thick. (a) single-channel specimen, (b) 3-channel specimen, and (c) 6-channel specimen

The effect of the pressure was clearly shown in the 1-channel and 3-channel samples, where higher channel height (h) was obtained at higher pressure level. The effect of channel spacing, defined as the distance measured from the center to the center of adjacent channels (a.k.a. inter-channel distance, W_{int}), was also observed when comparing the channel profiles of the 1-channel and 3-channel specimens that were formed at the same pressure level. Less formed height was measured from the 3-channel specimens due to the higher constraint on the material flow. On the other hand, the formed height on the 6-channel specimens appeared to be more dependent on the die width (W) rather than the die height (H) or pressure. For example, higher channel height (h) was obtained when wider channel was used ($W = 1.33$ mm for channel #5 and $W = 0.78$ mm for channel #4, both with $H = 0.46$ mm). In addition, the channel heights (h) were measured to be approximately the same in the case of forming channels #3 and #4 that have different die heights (H), but the same die width (W), showing the dominant

effect of the die width (W) on the formability over the die height (H). Another notable observation was also made in forming channels #5 and #6, both with $W = 1.33$ mm, but different die height (H). At the pressure level of 82.7 MPa (12,000 PSI), the blanks were ruptured in channel #6, while a fully formed channel was obtained in channel #5. This observation suggested that there exists an optimal aspect ratio (h/W) that could be obtained at each specific pressure level above which rupture could occur due to excessive wall thinning.

In the second set of experiments, the effect of the material grain size was investigated by using thin SS304 blanks with three different grain sizes ($d = 9.3, 10.6,$ and 17.0 μm). These blanks were hydroformed using 6-channel die at a pressure level of 82.7 MPa (12,000 PSI). The hydroformed channel profiles are shown in Figure 4-7. The measurement profiles showed an uncertain trend of the grain size effect on the channel height/formability; therefore, no conclusion could be drawn at this time. This unclear trend of the grain size effect is understandable if we can recall that in the previous chapter the material flow curves of different grain sizes are not significantly different either. However, in the case of the bulge tests, the effect of the grain size on the flow curves has a clear trend. This may be because the feature size in the case of the channel hydroforming (i.e., channel width) is much closer to the size of the grain; and thus, the orientation of the grains and their texture become important to the material response, and thus, formability. Furthermore, the process variation of about 20 μm in channel dimensions adds another factor to the observed difference in the channel profiles from material with different grain sizes. Nonetheless, channel #6 was also found to rupture for all three grain sizes at this pressure level.

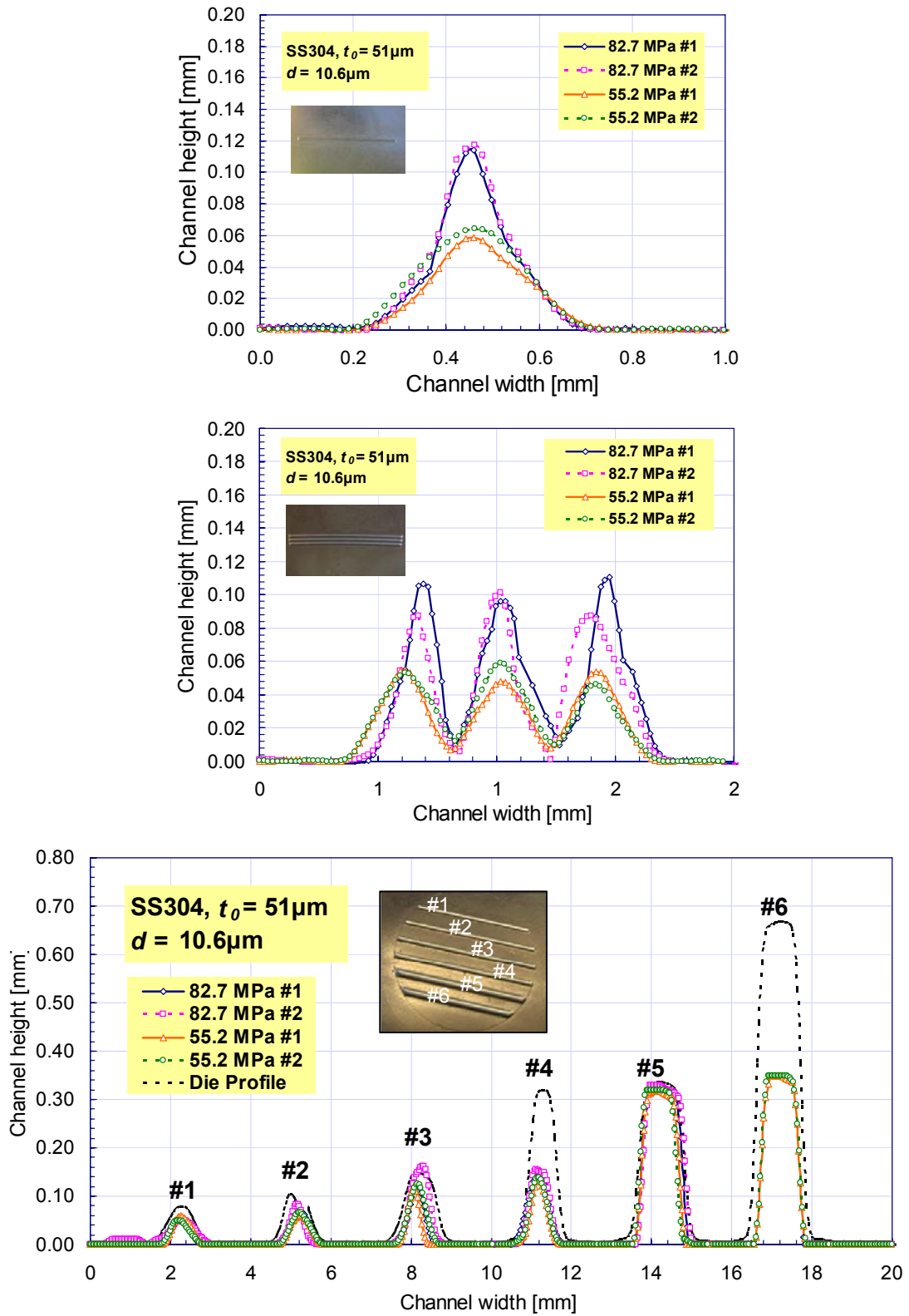


Figure 4-6: Micro-channel profiles of 1-channel (top), 3-channel (middle), and 6-channel (bottom) specimens

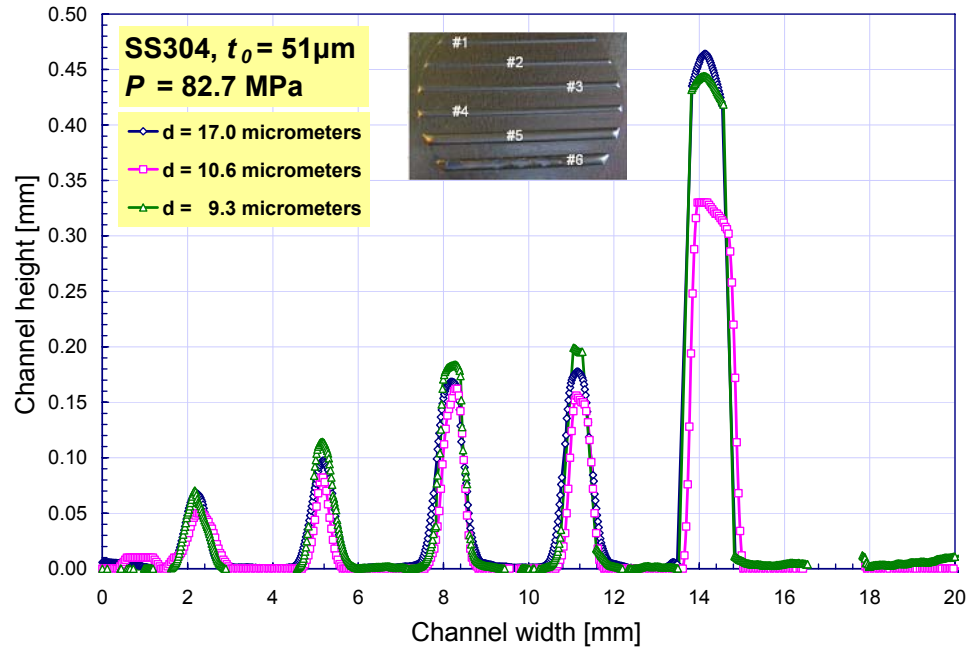


Figure 4-7: Effect of material grain size on the micro-channel formability

In this section, the experimental results showed that the process is repeatable with the maximum dimensional variation of 20 micrometers. Thus, the hydroforming process is a legitimate candidate for producing accurate micro-channel dimensions to be used in micro-devices. In the following section, FE models are developed and validated with the experimental results.

4.4 FE Models and Validation

The hydroforming process of thin sheet blanks to form micro-channel arrays is modeled using an FE tool (MSC.Marc) to further investigate the manufacturability of different micro-channel designs. One of the crucial factors leading to reliable process and design predictions is the use of accurate material models. In the previous chapter, the “size effects” on that material behavior of thin SS304 blanks were investigated and characterized. In this section, the material flow curves that were obtained from the

bulge test results using five different bulge diameters of 2.5, 5, 10, 20, and 100 mm and from the proposed material model that includes the size effect parameters (N and M where $N = t_0/d$ and $M = D_c/t_0$) are used as the material models. The comparison between the experimental and simulation results will indicate which material flow curve provides the best predictions in terms of the micro-channel hydroformability. The strength coefficient (K) and strain-hardening exponent (n) values that described the flow curves obtained from the bulge tests are listed in Table 4-2 as well as the material constants (a , b , c , and n) for the proposed material model. Note that the values of N and M that should be used in the proposed model are 4.8 and 9.8, respectively, since the material grain size (d) is 10.6 micrometers, the specimen sheet thickness (t_0) is 51 micrometers, and the micro-channel width (W), as the feature size, is 0.5 mm. Other material data used in the model are Young's modulus of 195 GPa, Poisson's ratio of 0.29, and mass density of 8E-9 kg/m³. Based on the experimental and simulation result comparisons, the material flow curve or model that best describe the material behavior of the thin SS304 blanks in the hydroforming process will be selected to be used in the next section where a series of parametric studies is conducted.

SS304, $t_0=51\mu\text{m}$, $d=10.6\mu\text{m}$, ($N = 4.8$)	Bulge test: $\sigma = K \epsilon^n$					$\sigma_{\text{model}} = (a+bN^{0.5}+cM^2/e^{\epsilon}) \epsilon^n$	
	$D_c = 2.5\text{mm}$	$D_c = 5\text{mm}$	$D_c = 10\text{mm}$	$D_c = 20\text{mm}$	$D_c = 100\text{mm}$	a	1,658
	$M = 49$	$M = 98$	$M = 196$	$M = 392$	$M = 1,961$	b	148
K [MPa]	1,325	2,207	1,406	1,375	1,428	c	-0.0297
n	0.39	0.68	0.74	0.53	0.54	n	0.54

Table 4-2: Material constants for different flow curves

As for the boundary and loading conditions of the FE models, the blank is fixed at the nodes at both ends to prevent the draw-in effect, and normal pressure is applied at the element edges as illustrated in Figure 4-8. A ramp pressure loading with a slope of

2,000 PSI/second is selected based on the actual pressure profile measured during the experiments. Solid elements are used for the modeling of the blank with three to eight elements across the thickness depending on the maximum strain value in each case. Coulomb friction condition is assumed in this study. Different values of friction coefficient ranging from 0.003 to 0.3, the commonly use values for friction coefficient in metal forming processes, are tested to identify the most suitable value that would provide the best prediction for channel formability. However, the effect of the friction coefficient on the channel formability is found to be insignificant. This may be because of the small contact area between the sheet and the die surface with the test setup in this study. Therefore, the friction coefficient is selected to be 0.03, a moderate value, for the rest of this study. The FE model of the process setup is demonstrated in Figure 4-8 for the 3-channel die insert.

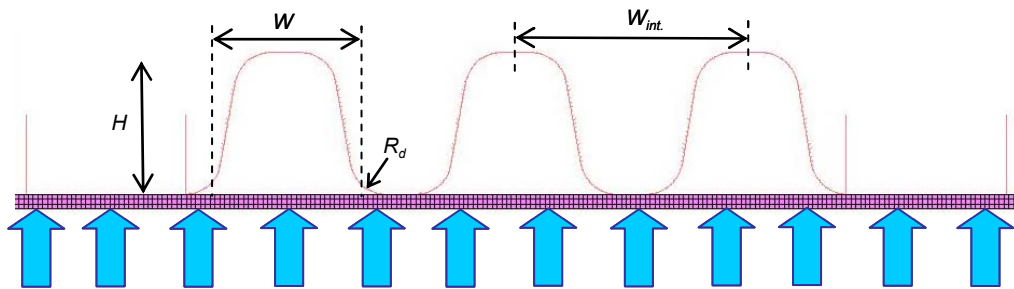


Figure 4-8: Simulation set up

In order to compare the experimental result to the simulation prediction, the height of the hydroformed channels (h) was selected as the measure of the sheet formability. The comparisons of the results in Figure 4-9 show that the prediction of the channel height using the calculated flow curves obtained from different bulge sizes

changes according to the material strength. That is when the material flow stress (i.e., strength) is lower, the predicted channel height would be higher. And since the flow stress obtained from the 10 mm bulge diameter is the lowest among all, the predicted channel height is the highest in the FE simulation. Nonetheless, all the material flow curves from the bulge tests and the proposed model are shown to over predict the channel height for both 1-channel and 3-channel dies at both pressure levels. Note that in Figure 4-9, the variations in the channel height values (i.e., error bar) for the 3-channel die case come from the differences between the channel heights at the middle and at the left or at the right. The channel height at the left channel always equals to the right due to the symmetry reason. The channel height is lower at the middle because the material at this region is constraint by the adjacent channels on both sides; and thus, the material flow is more difficult. A typical channel profile of the 3-channel specimen showing the height variation is illustrated in Figure 4-10.

The poor simulation predictions based on these flow curves are believed to be caused by the feature size effect on the material response since there is a significant difference in the size scale between the smallest bulge diameter used in the bulge tests ($D_c = 2.5$ mm) and the micro-channel width used in the hydroforming experiments ($W = 0.5$ mm). Therefore, the flow curves calculated based on the bulge tests may not be able to represent the actual deformation mechanics at the micro-scale; and thus, resulted in the discrepancy in the result comparisons. Nonetheless, the proposed model was shown to provide better prediction than most of the flow curves obtained from the bulge tests, except in the case of the flow curve from the 2.5 mm bulge diameter. As a result, the proposed model would require further modifications in order to better predict the channel

hydroformability for the eventual FEA of the process design. Further investigation is needed to understand and include other size effect parameters besides N and M , such as material anisotropy, material defects, dislocation density, preferred slip planes, etc., into the proposed model in order to improve its accuracy.

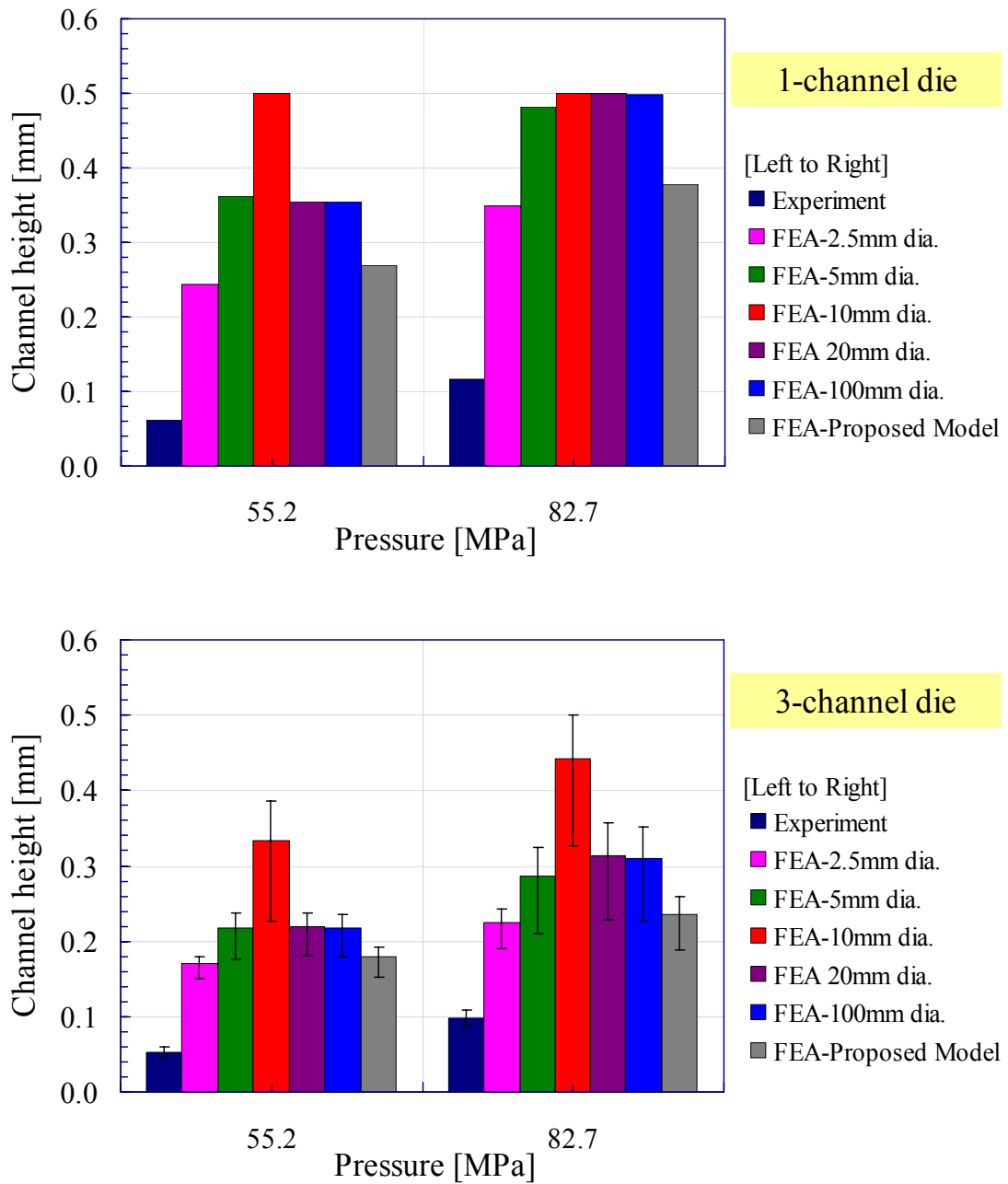


Figure 4-9: Simulation results for channel height prediction from different material flow curves and models

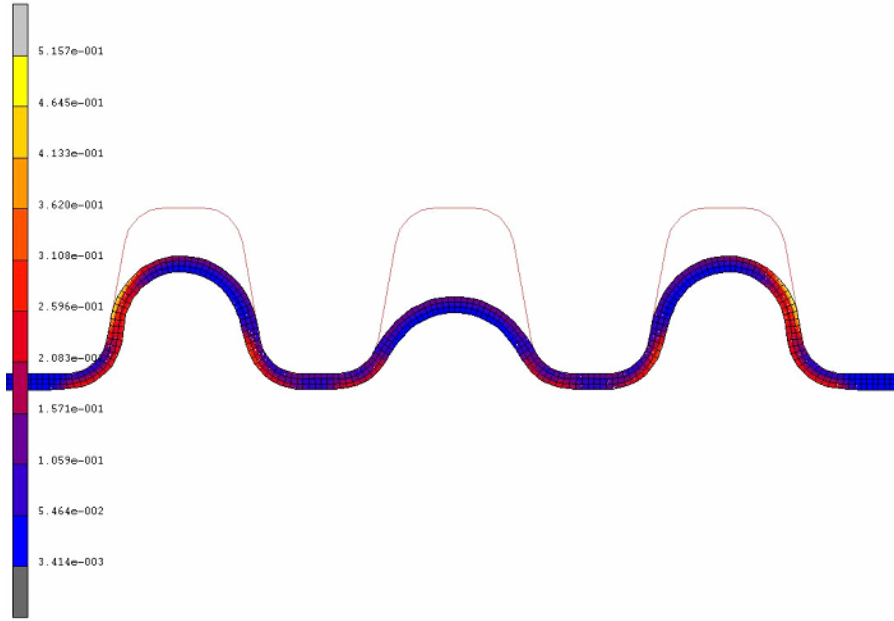


Figure 4-10: A typical channel profile for 3-channel specimens with lower channel height at the center

Finally, since the flow curves obtained from the bulge tests and the proposed model could not accurately predict the channel hydroformability, a reverse FEA method was utilized with an attempt to determine the material flow curve that would provide better predictions in terms of the channel height when compared to the experimental results. Based on different trial and error runs in the FEA, the flow curve with $K = 1,400$ MPa and $n = 0.12$ yielded reasonable predictions for both the 1-channel and 3-channel specimens as shown in Figure 4-11. From the observations during the trial and error runs in the FEA, it appears that better predictions could be obtained by decreasing n value further, but lowering the n value below 0.12 would almost eliminate the strain-hardening effect; and thus, not pursue in this study. On the other hand, varying the K value does not show a significant improvement of the channel height prediction. This may be because the hydroforming of the micro-channels occurs at a low range of the strain values ($\epsilon < 0.3$) and the effect of n value is much more prominent in this region

than the K value on the material flow curve. Thus, in the parametric study in the following section, several values of the strain-hardening exponent, n , are used in the FEA to show the effect of the material response, specifically, the strain-hardening behavior (n) and the micro-channel geometries on the overall formability of the channels (i.e., channel height). The results from this parametric study would lead to an establishment of design guidelines for the micro-channel tooling in order to yield the maximum channel aspect ratio that is desired in most heat and mass transfer applications.

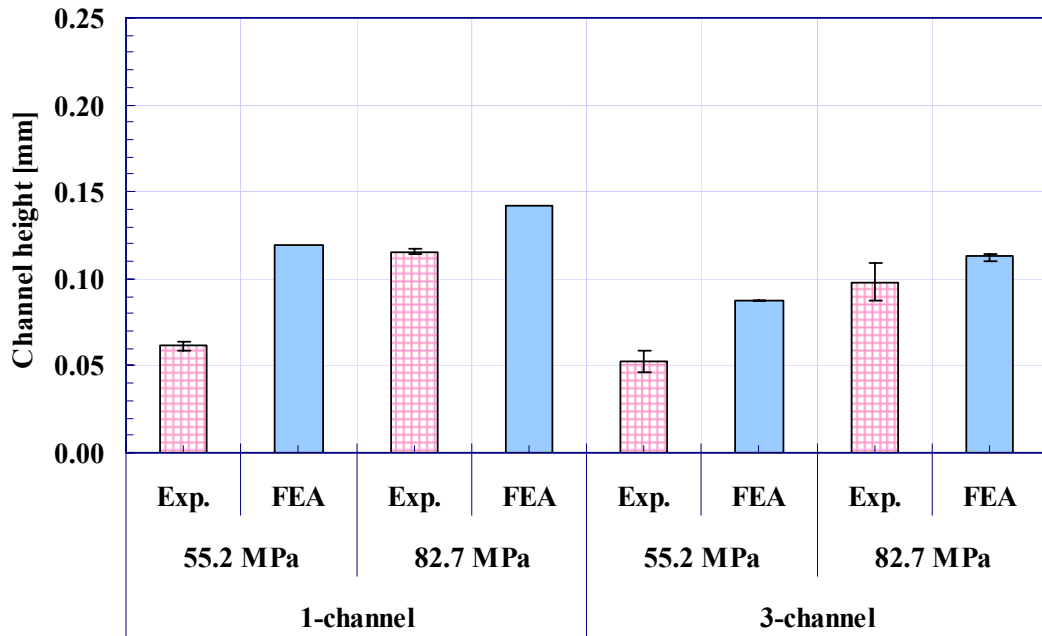


Figure 4-11: FEA result comparison using $\sigma = K\varepsilon^n$ with $K = 1,400$ MPa and $n = 0.12$

4.5 Parametric Study

In this section, a parametric study is conducted using FEA models of the micro-channel hydroforming developed in the previous section to investigate the effect of different micro-channel geometries on the overall channel formability. The studied

parameters include die width (W), draft angle (α), die corner radius (R_d), channel spacing (i.e., inter-channel distance, W_{int}), and channel number. In order to make the results from this parametric study more generalized and useful for different material responses (i.e., different n values), three values of strain-hardening exponent, n , of 0.12, 0.36, and 0.60 are used for each combination of channel geometries. The strength coefficient, K , is kept at a constant value of 1,400 MPa in this study because the K value only affects the flow curve by shifting it up or down, while n value indicates how the material would response to the applied pressure. Thus, the results from this parametric study could be used for material whose n value lies within the selected range (i.e., 0.12 to 0.60). The forming pressure that is required for successful hydroforming of thin blank material would need to be scaled accordingly with different K values for different blank materials.

In this study, the channel height (h) is regarded as the output response from the simulation to represent the formability; and thus, the channels on the die are modeled such that the bottom part is open (Figure 4-12). Furthermore, the initial blank thickness (t_0) is kept constant at 0.051 mm for all simulation cases since the formability of the channel depends on the ratios of the channel geometries to the initial blank thickness (i.e., W/t_0 , R_d/t_0 , W_{int}/t_0 , etc.) rather than each individual parameter itself. Therefore, we could also understand the effect of the change in thickness value by varying other channel parameters. The parametric study is divided into two sections: single-channel and multi-channel hydroforming. In the former, the effect of the channel width (W), draft angle (α), and die corner radius (R_d) is investigated, while the latter focuses on the effect of the inter-channel distance (W_{int}) and the channel number.

4.5.1 Single-channel Hydroforming

The studied ranges of W , α , and R_d are given in Table 4-3. For each case, the blank is hydroformed up to the maximum pressure (P_{max}) level, defined as the pressure level where the maximum thickness reduction is 25% of the initial thickness (i.e., 25% thinning). The aspect ratio (AR), defined as the ratio between the formed height (h) and the channel width (W), is used as the formability index. The simulation results are presented in Figure 4-13 and Figure 4-14.

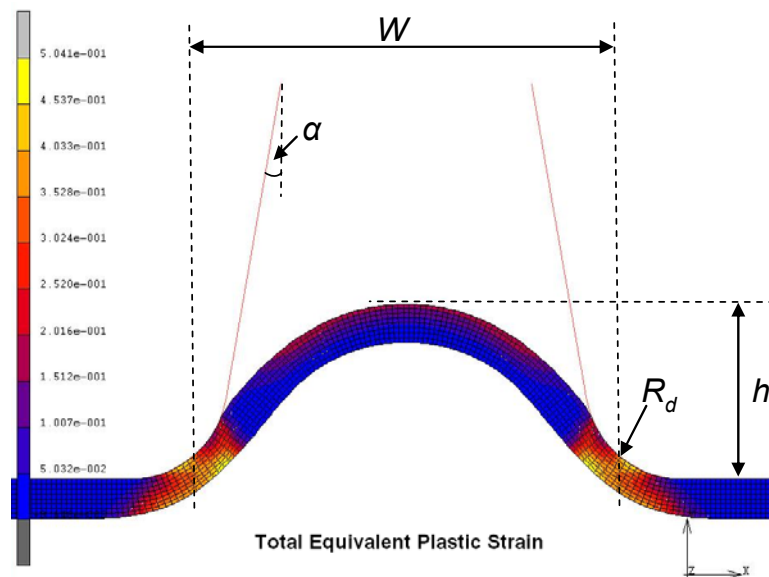


Figure 4-12: Studied parameters in the FE simulations

Studied Parameters	W [mm]	α [°]	R_d [mm]
Die width, W	0.125, 0.25, 0.5, 1.25, 2.5	10	0.125
Draft angle, α	0.5	5, 10, 20	0.125
Die corner radius, R_d	0.5	10	0.0625, 0.125, 0.25

Table 4-3: Study cases of single-channel in FEA

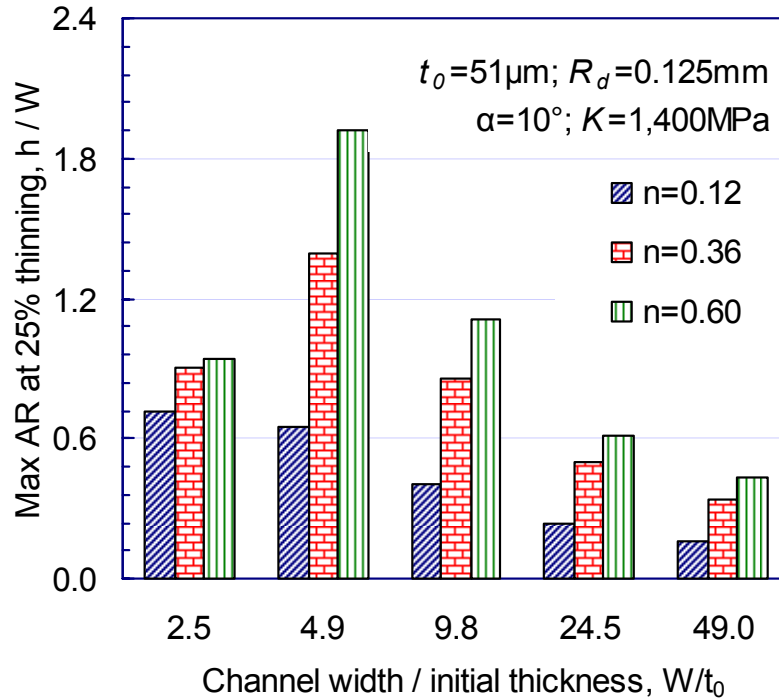


Figure 4-13: Effect of channel width (W) and strain-hardening (n) on maximum aspect ratio (AR)

The simulation results in Figure 4-13 show that for material with lower n -value ($n = 0.12$), the aspect ratio ($AR = h/W$) increases with decreasing channel width (W). This is due to the fact that when the simulation was stopped at the 25% thinning, the same stretching/thinning profile would be expected at the die corner radius area for all channel width sizes (i.e., die corner radius was fixed at 0.125 mm in this case). Therefore, channel with a higher W value would yield a smaller AR value. However, for $n = 0.36$ and 0.60 , the maximum AR is highest when $W/t_0 = 4.9$. This happens because when W/t_0 ratio continues to reduce, the channel width (W) becomes the dominant parameter that affect the overall formability, as discussed in the experimental results. In other words, when W/t_0 is small, the maximum AR values would converge to a single value, diminishing the effect of the n -value. Nonetheless, the effect of the strain-

hardening and the channel width on the channel formability is coupled, and therefore, should be considered simultaneously. In addition, the forming pressure is found, as expected, to increase significantly with decreasing W/t_0 ratio (e.g., forming pressure = 800-850 MPa in the case of $n = 0.12$ and $W/t_0 = 2.5$). As a result, the maximum AR may not be feasible for small W/t_0 ratio due to the manufacturing limitation. On the other hand, material with higher n -value (i.e., weaker material) would require less forming pressure for the same W/t_0 and AR values. The simulation results in Figure 4-13 reveal the significant effect of the W/t_0 ratio and the n -value on the channel formability.

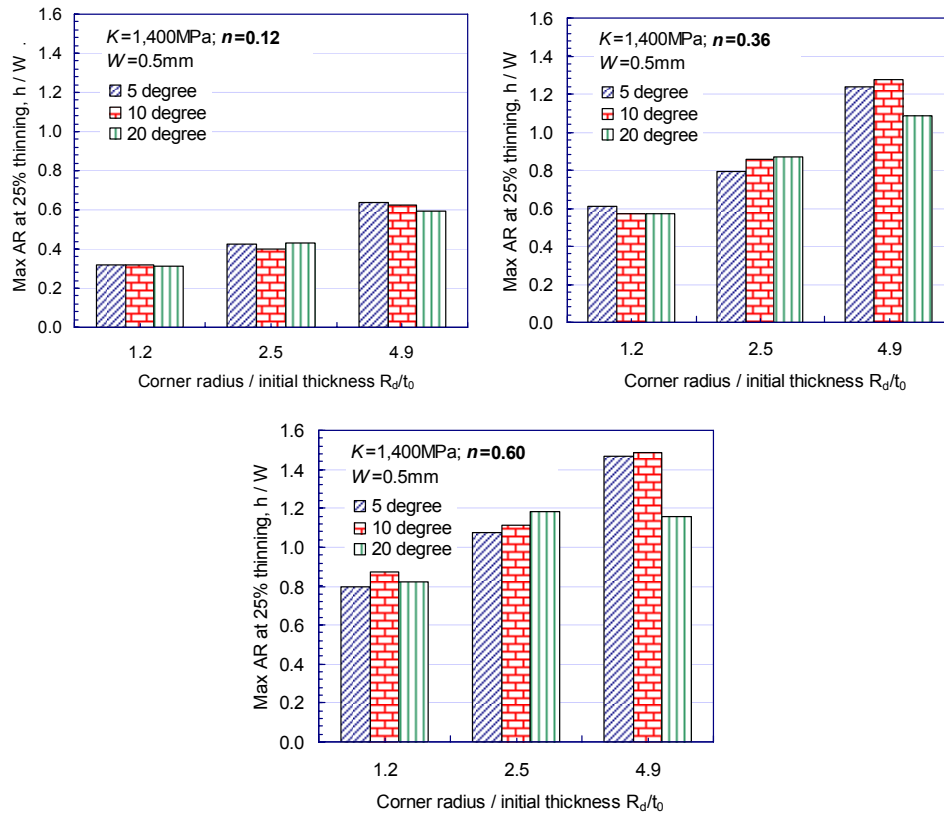


Figure 4-14: Effect of corner radius (R_d), draft angle (α), and strain-hardening (n) on maximum aspect ratio (AR)

The simulation results from the study of the corner radius (R_d), draft angle (α), and n -value effects on the maximum aspect ratio (AR) is shown in Figure 4-14. An increase in R_d value is shown to increase the channel formability, while the effect of the draft angle between 5-20° only slightly affects the maximum AR value. However, even though a large corner radius would improve the overall channel formability, this is not desirable from the performance perspective as a larger R_d would decrease the number of channels that can be produced on a given plate size. Therefore, the value of R_d should be selected based on both the forming and the computational fluid dynamic (CFD) simulation results. On the other hand, since the draft angle (α) only contributes a small effect on the overall formability, it is suggested to be made as low as possible (i.e., steep channel) in order to maximize the cross-sectional area of the channel in order to reduce the pressure drop value; and thus, increase the heat/mass transfer capability. Finally, the effect of the strain-hardening (n) has revealed a similar trend on the channel formability; that is the maximum AR value increases with increasing n -value (i.e., weaker material). Since the effect of the material strain-hardening value (n) is fully revealed in this section using the single-channel geometry, this effect will be omitted in the following section, which is aimed to study the effect of the channel spacing and the channel number on the channel formability and variation between different channels on the same blank.

4.5.2 Multi-channel Hydroforming

The effects of channel spacing (W_{int}) and channel number on the height and thickness variation are investigated using FEA in this section. The selected ranges for the channel spacing and the channel number are 1-2 mm and 3-12, respectively. The

simulations are also stopped at the 25% thinning mark. Other parameters are selected to be: channel width (W) = 0.5 mm, draft angle (α) = 10°, corner radius (R_d) = 0.125 mm, initial blank thickness (t_0) = 0.051 mm, K = 1,400 MPa, and n = 0.12. The simulation results are presented in Figure 4-15.

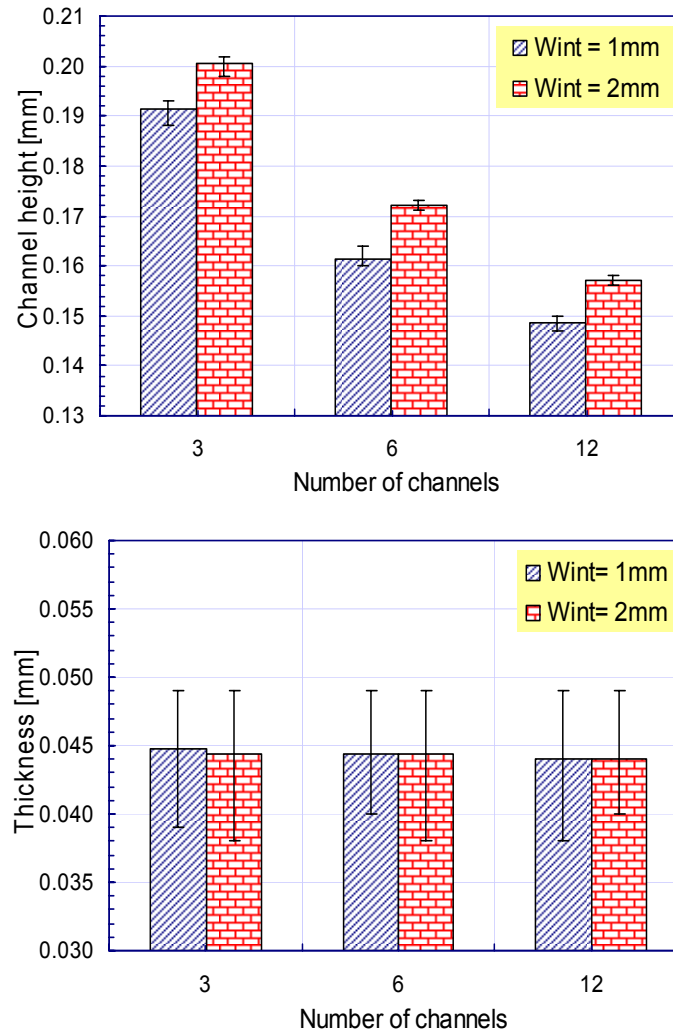


Figure 4-15: Effect of channel spacing (W_{int}) and channel number on the channel height and thickness distribution

Both channel spacing and channel number are shown to have considerable impact on the channel hydroformability. Higher channels could be formed when using

larger channel spacing or less number of channels. On the other hand, only slight effect of these two parameters is observed on the thickness distribution. The thinnest location is always observed at the corner radius of the channel close to, but not at, the channel at the middle of the arrays. The thickness at the land and valley regions for all studied cases here is found to be 0.049 mm. In other words, the maximum value of the thickness in Figure 4-15 is measured at the land or valley regions, while the minimum thickness value is measured at the corner radius areas with the minimum value of 0.37-0.38, which corresponds to the 25% thinning threshold.

4.6 Summary and Conclusions

In this study, the fabrication of micro-channels using internal fluid pressure (hydroforming) was investigated from the design and manufacturability aspects. A hydroforming apparatus was developed to conduct micro-channel hydroforming experiments on thin SS304 sheets (51 μm thick) with different material grain sizes (9.3 – 17.0 μm) and channel sizes (0.46 – 1.33 mm in width and 0.15 – 0.98 mm in height). The repeatability of the process and the accuracy of the laser measurement system were first evaluated and shown to be repeatable and reliable with small variations of channel dimensions below 20 micrometers. The experimental results showed an unclear effect of the material grain size on the channel hydroformability, while the forming pressure and the feature (channel) size were shown to have significant impact on the hydroformed channel height.

FEA tool was employed to conduct a parametric study in order to establish design guidelines for the micro-channels in the hydroforming process. In the parametric study, the studied parameters were channel width (W), draft angle (α), die corner radius

(R_d), channel spacing (W_{int}), and channel number. The material flow curves used in the parametric study were selected to be $K = 1,400$ MPa with $n = 0.12, 0.36,$ and 0.60 since none of the material flow curves calculated from the bulge tests with different bulge diameters (2.5, 5, 10, 20, and 100 mm) and the proposed model in the previous chapter could provide close predictions of the channel height. The results from the parametric study suggested that in order to obtain a higher value of the maximum aspect ratio ($AR = h/W$), a small channel width (W) should be used. Even though a large channel width (W) would result in a higher channel height (h), the aspect ratio (h/W) was found to be lower in this case due to the similar stretching/thinning profiles at the die corner radius (i.e., $R_d = 0.125$ mm) for all channel width values. In addition, higher aspect ratio could be obtained by using larger corner radius (R_d), wider channel spacing (W_{int}), or less number of channels on a given plate size, but these design modifications may not be desirable from the performance point of view. In this study, the variation in draft angle (α) between 5° and 20° in combinations with the other channel geometries was found to have a slight effect on the channel height. On the other hand, the material response (i.e., strain-hardening coefficient, n) is shown to significantly affect the maximum AR values, and thus, the channel design and forming pressure. Finally, the thickness reduction on the multi-channel arrays was found to be about 4% at the valley and land locations, while around 25% thinning was observed at the corner radius regions.

All in all, these channel parameters ($W, R_d, W_{int}, \alpha,$ channel number, etc.) would need to be designed and optimized simultaneously in order to obtain such a design of the micro-feature arrays that would meet the performance requirements and still be within the manufacturing limitations. However, the general design guidelines from the

manufacturing point of view are provided in this study. This study can also be found in the Journal of Power Sources [*Mahabunphachai, 2008*].

CHAPTER 5: CHARACTERIZATION OF PRESSURE WELDING PROCESS OF THIN SHEET METALS IN COLD AND WARM TEMPERATURE CONDITIONS

5.1 Introduction

Pressure welding is a solid state welding technique used in many applications to bond similar or dissimilar ductile metals together under high compressive pressure. If the process involves heating, it is known as “warm welding” (a.k.a. “low temperature welding”) for temperature below $0.3 \cdot T_m$, where T_m is the melting temperature in K, or “diffusion welding” (a.k.a. “high temperature welding”) for the welding temperature between 0.3 and $0.7 \cdot T_m$. If the process does not require heating, it is called “cold welding” [Williams, 1976; Lehrheuer, 1993]. Even though pressure welding is one of the oldest joining techniques, its applications are limited, and it requires a lot of experiences based mostly on the empirical methods. When the materials or process conditions are changed, the know-how from previous conditions cannot simply be applied to the new cases. The pressure welding process is suitable for applications that require close tolerances where changes in dimension or metallurgical structure of the material are unacceptable.

Theoretically, the *bond strength* should be as strong as grain boundaries within the parent metals, depending on crystallographic match across the interface, inter-diffusion, and recrystallization. However, in practice it is difficult to obtain a high

degree of surface cleanliness by any mechanical or chemical cleaning techniques. One of the most commonly used methods for the *surface preparation* prior to the pressure welding is by degreasing and then scratched-brushing the surfaces with steel wire brush (0.004" diameter). The reverse of the order gives poorer bond due to the degreasing agent covering the newly-exposed metal surfaces [Sowter, 1949; Donelan, 1959; Williams, 1976]. In addition, in the case of aluminum, the surface can be cleaned by anodizing the surfaces of the sheets. This process would require no other surface preparation and only sacrifice about 10% reduction in bond strength when compared to brushed-surface case [Donelan, 1959]. It is also recommended to perform the cold welding right after the surface preparation step to keep the contaminant layer from reforming. On the downside, the surface preparation method may introduce some *work-hardening* to the surface layer with roughened texture. Nevertheless, a previous study by Pendrous et al. [Pendrous, 1984] showed that no significant difference was observed between work-hardened and annealed Cu samples in terms of *threshold deformation*, defined as the minimum plastic deformation required to initiate the bond between the two metal surfaces below which the weld would fracture upon removal of load due to released elastic stresses.

The value of bond strength has been shown to significantly depend on the amount of *deformation* (i.e., thickness reduction in the case of joining sheet metals). As the percentage deformation increases, the value of bond strength will progressively increase until it reaches a maximum point at an *optimal deformation* value, followed by a decrease, corresponding to fracture across the reduced cross-section of the two bonded blanks. In welding dissimilar materials, the threshold deformation is controlled by

deformation of the softer metal [Donelan, 1959; Pendrous, 1984]. Both threshold deformation and optimal deformation values are totally material and process dependent; that is these values will change as the metal combinations or process conditions are changed. Therefore, it is rather difficult to attempt to predict these deformation values for materials and process setups that have not been experimentally tested. This is one of the main reasons why most successful pressure welding results were obtained based on empirical method. Nonetheless, some threshold deformation values of different metals that can be cold welded as suggested in literatures are given in Table 5-1.

Material	Threshold Deformation
Pure aluminum	20-60%
Aluminum alloys	70-80%
Copper	40-80%
Lead	84%
Nickel	89%
Zinc	92%
Silver	94%
Stainless steel	> 81% *

*Not welded at this value

Table 5-1: Threshold deformation of some metals that can be cold welded [Sowter, 1949; Donelan, 1959; Pendrous, 1984]

In addition, the threshold deformation was reported to be dependent on the *indenting die design* as well as the *material sheet thickness*. A satisfactory tool design is a single straight joint where the stress is perpendicular to the length of the weld. The threshold deformation can be decreased by lowering the ratio between indenting die width, W , and material sheet thickness, t . For example, using narrower indenting platens of 3.2 mm on 3 mm thick composites of Cu-CuZn30 as compared to the indenting platens of 7.7 mm, the threshold deformation decreased by 50% while the pressure required for welding also decreased by about 70% [Pendrous, 1984]. For a *rectangular*

shape indenter, the width of the indenter was suggested to be equal to the gauge thickness ($W = t$) for a double action tool (indent from both sides) and the length of the indenter must not be less than five times of the sheet thickness, $5t$. For a single action tool used in conjunction with a flat plate or anvil, the tool width, W , should be reduced to $\frac{1}{2} t$ [Sowter, 1949]. The distance between each spot being welded and distance from the weld to the sheet edge should be about $5t - 6t$ to allow the material to flow freely [Donelan, 1959]. For welding of dissimilar materials which have different hardness values, a tool with a larger surface area should be used on the softer surface to promote a uniform flow of the two metals on both sides. The ratio of tool surface area should be scaled proportionally with the hardness ratio of the two metals (e.g., if the hardness is doubled, the tool width should be reduced to $\frac{1}{2}$ on the contact side of the harder material) [Sowter, 1949; Donelan, 1959]. A *circular shape indenter* results in an undesirable curvature from a radial flow of metals. This can be prevented by allowing more spacing between the weld spot to the edge of the specimen so that the effect of the radial flow will not reach the specimen edge; thus, no shape changes would be observed. In addition, the *die material* should not introduce too much adhesive force between the dies and the specimens in order to avoid the “pickup” from occurring [Sowter, 1949].

The effect of *temperature* on the bond formation has been studied by Sim [Sim, 2005]. The minimum welding pressure was found to be decreasing with increasing welding temperature. The effects of *surface roughness* and *holding time* were also examined in the same study. The results showed that lower welding pressure would be required for the surface with higher roughness value and the bonding strength would increase rapidly with the increased holding time until 10 minutes and after then the rate

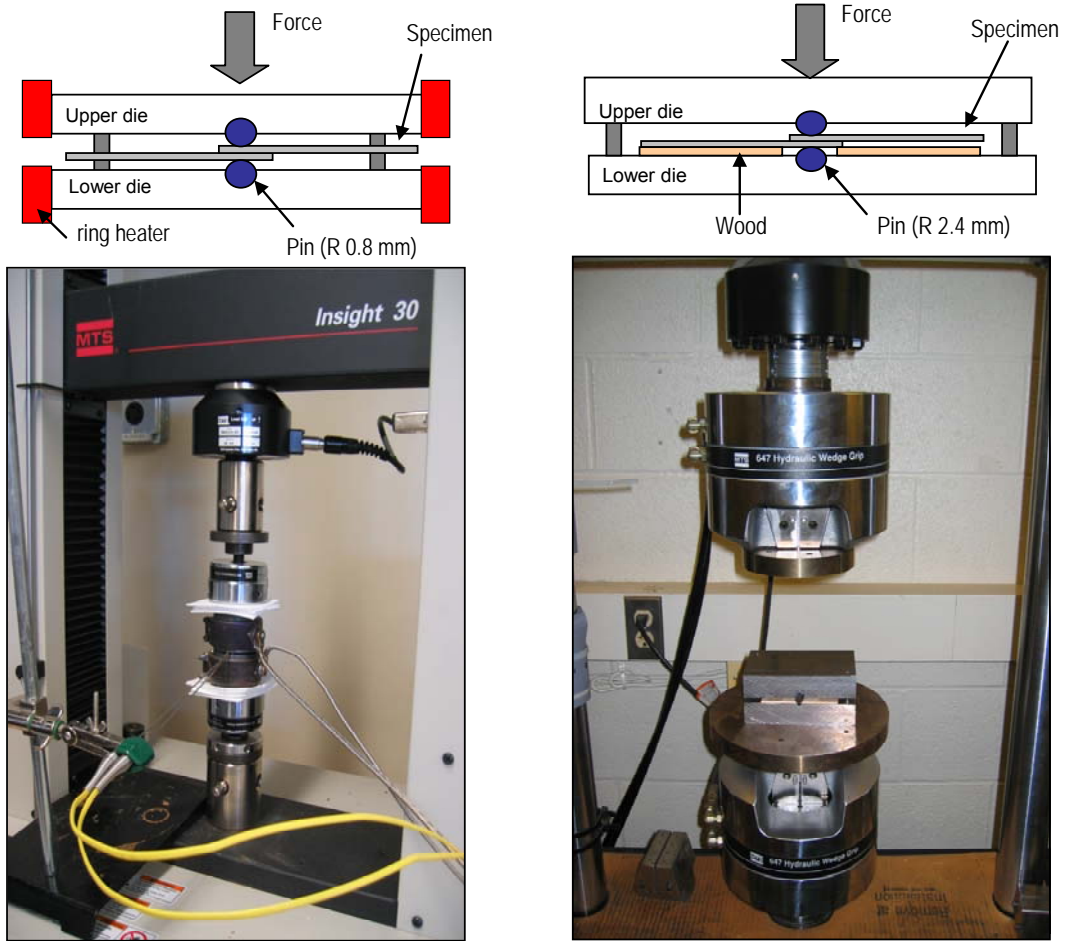
of increase of the bonding strength is slow. Such behavior was observed at the relatively high welding temperature of 130°C and 200°C. However, no evident changes in bonding strength were observed with the increased pressure holding time until 20 minutes at room temperature [Sim, 2005].

Although the pressure welding process has been studied and understood almost fully, the technology and knowledge are mostly developed for the applications of ductile materials, such as copper and aluminum alloys, and for specimen size (i.e., diameter or thickness) at macro-scales. Therefore, the objective of this chapter is to investigate and understand how this pressure welding technique could be applied to stronger and harder materials, such as nickel and stainless steel alloys, and micro-scale specimen size. In Chapters 2 and 3, the material behavior of thin sheets has been shown change when the specimen size is reduced to the micro-scales. Therefore, the specimen size (i.e., sheet thickness) on the pressure welding process will be investigated here. Specifically, in this chapter, the focus of the study is placed on the pressure welding of thin stainless steel and nickel blanks due to their increasing and promising utilization in fuel cell bipolar plates. However, to broaden the understanding of the process, aluminum and copper alloys blanks are also used to investigate the process at different conditions where stainless steel and nickel blanks are not applicable. Several sets of pressure welding tests are conducted to establish optimal process guidelines and design methods. In the next section, the experimental method and procedures are described in detail, followed by the results and discussion section. In the last section, a summary of the results and understanding of the process is presented.

5.2 Experimental Setup and Procedure

Two sets of experimental setup were developed in this study to conduct a series of experiments to characterize the effects of material and process condition on the minimum welding pressure and bond strength. As shown in Figure 5-1, each experimental setup consists of upper and lower dies and two cylindrical pins of H13 tool material. The pin diameters were 1.6 mm (1/16") for setup (a), and 4.8 mm (3/16") for setup (b). These pins were placed inside a straight groove located at the center of each die. With the cylindrical shape of these pins, it would be more appropriate to use the pin radius values to define the indenter size rather than the pin diameter. For simplicity, throughout this chapter, the indenter size in setup (a) will be referred to as 0.8 mm indenter, and the one in setup (b) as 2.4 mm indenter. To prevent distortion of the sheets from bending, two thin pieces of wood were placed beneath the specimens to assure the symmetry of the setup in setup (b). On the other hand, no supporting wood pieces were used in setup (a) because the pin diameter is relatively small in this case.

Setup (a) could be used to conduct the experiments in both cold and warm temperature levels, while setup (b) could only be used in the cold condition. In setup (a), ceramic ring heaters with a maximum operating temperature of 760°C (1,400°F) were attached to each die, Figure 5-1a. Two thermocouples were used to measure the temperature of each die half. The welding temperature is precisely controlled by a temperature controller which only allows a slight temperature fluctuation of less than 5°C during the welding process. Depending on the target welding temperature, the heating time is between 10 and 25 minutes with the use of insulators at the top and bottom of the die set.



(a) Indenter radius = 0.8 mm (cold/warm) (b) Indenter radius = 2.4 mm (cold)

Figure 5-1: Experimental apparatus

Three different equipments, 3-ton and 10-ton MTS machines and a 220-ton Instron machine, were employed to supply the joining force. Since the force data were obtained from these machines, the welding pressure was calculated by dividing the measured force by the weld area. Note that even though the holding time was shown to affect the bond strength, especially at the elevated temperature levels [Sim, 2005], in this study the holding time of 10 seconds is used for all the tests mainly because the ultimate goal of this study is to apply this joining technique to mass produce thin double bipolar plates; and thus, a longer holding time would be inappropriate.

The weld area was calculated using mathematical relations and with the measurement values of the final thickness of the bonded blanks, t_f , along the weld line, Figure 5-2. The final sheet thickness was measured using a micrometer with special conical shape tips.

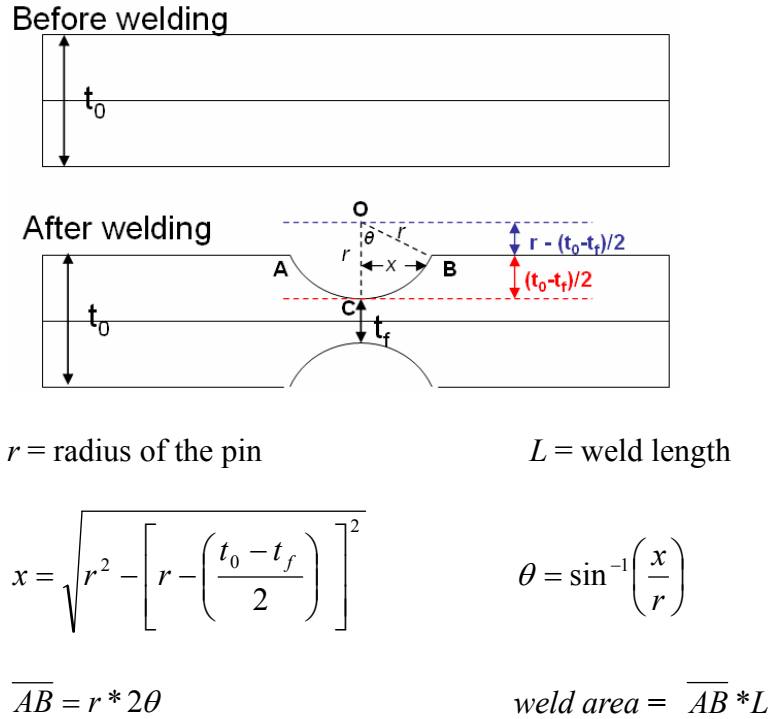


Figure 5-2: Calculation of weld area

The thickness reduction, defined as the ratio of the reduced thickness ($t_0 - t_f$) to the original sheet thickness (t_0), was also calculated using the measured values of the final thickness of the bonded blanks. This ratio was used to define the amount of plastic deformation of the sheet blanks at the end of the stroke.

$$\% \text{ thickness reduction} = \frac{t_0 - t_f}{t_0} \times 100\%$$

Thin blanks of Cu110, Al3003, Ni200, and SS304&316 with different thicknesses were used in this study. The material properties, which were obtained from

the database on *matweb.com* and *hpmetals.com*, are given in Table 5-2. The specimen size of 15 x 40 mm was used for all testing conditions, except for Al3003 where a size of 24 x 50 mm was used. Prior to welding, the specimen surfaces were degreased by acetone.

Grade	Thickness (mm)	YS (MPa)	Elong.
Cu110	0.051	69	50%
	0.076		
	0.127		
	0.254		
Al 3003	0.158	186	10%
Ni200	0.051	148	45%
	0.076		
	0.127		
	0.254		
SS304	0.051	215	70%
SS316	0.127	251	58%

Table 5-2: Material properties

A 5-kN tensile test machine was used to measure the bond strength under shear and normal loadings. For shear loading, the bonded specimens were pulled in the direction as shown in Figure 5-3a. For normal loading, each specimen was folded into a U-shape and placed between the grippers as shown in Figure 5-3b. The bond strength was calculated by dividing the peak force that the specimens could withstand by the weld area. All specimens were pulled at a low constant speed of 0.05 mm/s.

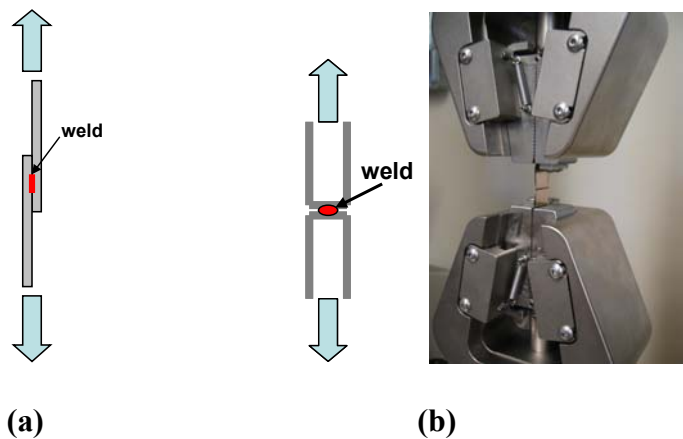


Figure 5-3: Tensile test of bonded specimens under (a) shear, and (b) normal loading

5.3 Results and Discussion

5.3.1 Effect of Surface Condition on P_{\min} and Bond Strength

Even though many literatures have reported the usefulness of the surface preparations (i.e., degreasing, scratch brushing, anodizing for Al), the discussion of the “wet” surface condition is still missing. This specific surface condition is critical to the present study of the hybrid manufacturing process because one critical process involves with the hybrid process is the mechanical bonding the two thin blanks in the present of fluid media for hydroforming of the specimens. Therefore, in this section, aluminum blanks (Al3003) with thickness of 158 micrometers are used to study the effect of the surface condition on both the minimum welding pressure and the bond strength. Three different surface conditions are investigated – wet, dry, and brushed. Water is used as the fluid medium in the wet surface condition, while coarse sandpaper (grit number 60, i.e., 60 abrasive particles per square inch) is used to prepare the brushed surface condition. To prevent oxide layers from forming over the newly brushed surface, the welding of the specimens is performed immediately after the cleaning and brushing of the specimen surfaces. Based on the results shown in Figure 5-4, the brushed surface reduces the minimum welding pressure, defined as the minimum pressure required to bond the two blanks, while the wet surface tends to increase it. In addition, the brushed surface condition enhances the bond strength, while the wet surface condition weakens it. Note that large variations were observed in the bond strength for the brushed surface case, and assumed to be caused by the unevenly scratched brushings on the different specimens. Therefore, it is possible to apply this welding technique to thin sheet metals with the present of the fluid media such as water, however, higher pressure would be required and

lower bond strength should be expected.

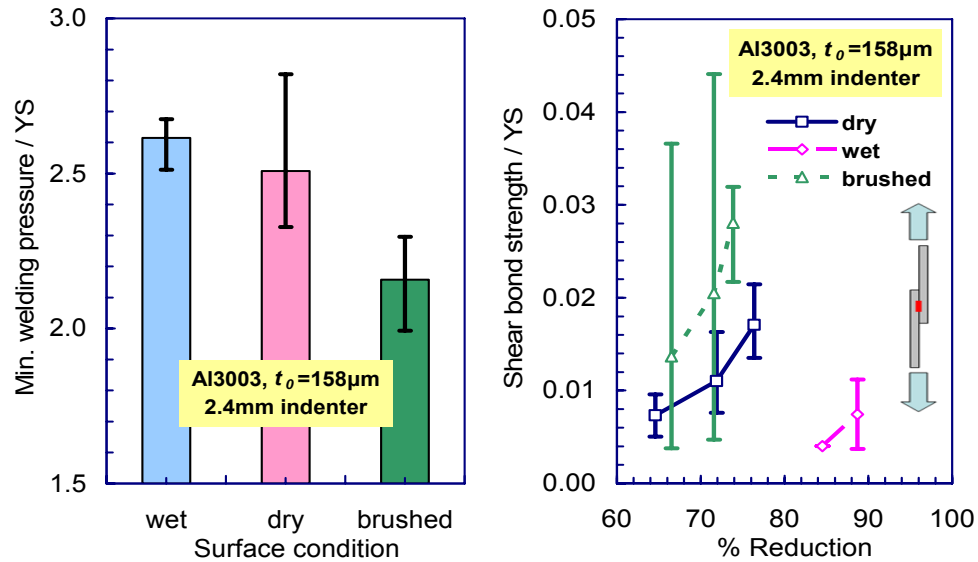


Figure 5-4: Effect of surface conditions on the minimum welding pressure and bond strength under shear loading

5.3.2 Effect of Material Type and Initial Blank Thickness on P_{min}

As mentioned earlier, the one of the goals of this study is to investigate the feasibility of the pressure welding process for the applications with stronger and thinner sheet blanks. Therefore, in this section the effects of material type and thickness are investigated. The 0.8 mm indenter die is used for bonding different blank materials of Cu110, Ni200, and SS316 and 304 blanks with the sheet thickness between 51 and 254 micrometers at room temperature. The minimum welding pressure is used to demonstrate the effect of the material type and thickness. Based on the results shown in Figure 5-5, for the same sheet thickness the ratio between the minimum welding pressure to the material yield strength of Ni200 is found to be higher than that of the Cu110 (YS of Ni200 = 148 MPa, YS of Cu110 = 69 MPa), showing that Cu110 blanks are easier to bond than Ni200. SS316 and 304 blanks (YS = 251 MPa and 215 MPa, respectively)

fails to bond at the room temperature even at the high welding pressure of 3,000 MPa. Deformation of the indenters/pins (H13 YS = 372 MPa) is observed at this level of welding pressure. When a deformation is observed on the pins, new pins are used to replace the deformed ones.

In addition, the blank thickness is shown to have a significant impact on the minimum welding pressure. As illustrated in Figure 5-5, when the sheet thickness of Cu110 and Ni200 is reduced, the minimum welding pressure is shown to increase. In thinner sheets, there is less amount of the material to be plastically deformed; thus, more welding pressure will be required to generate an adequate amount of the plastic flow to create the bond between two sheet metal blanks. Another observation is made on the scattering of the data which is larger for thinner sheets. We hypothesize that as the sheet blanks become thinner, there will be less number of grains across the thickness and the material response can no longer be regarded as homogeneous; but instead, dominated by the grain size and orientation, leading to larger variations as illustrated in Figure 5-5.

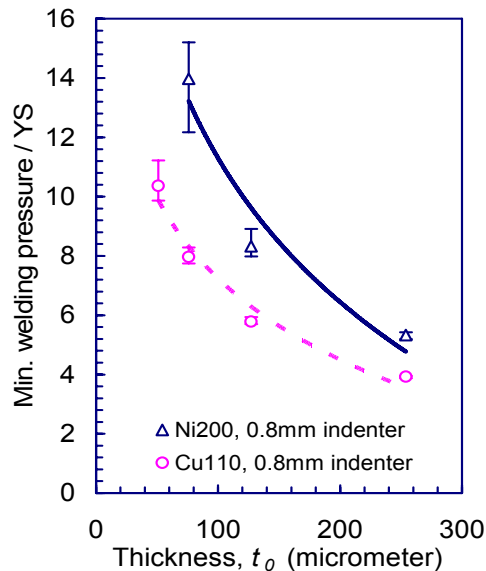


Figure 5-5: Effect of material type and thickness on the minimum welding pressure and its variation

5.3.3 Effect of Indenter Size on P_{min}

Two different indenter radii (0.8 and 2.4 mm) were used to bond Cu110 blanks at a room temperature. The effect of the different indenter radii on the minimum welding pressure is shown in Figure 5-6. However, only a slight difference was observed between these two indenter sizes. Furthermore, the effect of the blank thickness on the minimum welding pressure and scattering of the data were also observed with both indenter sizes.

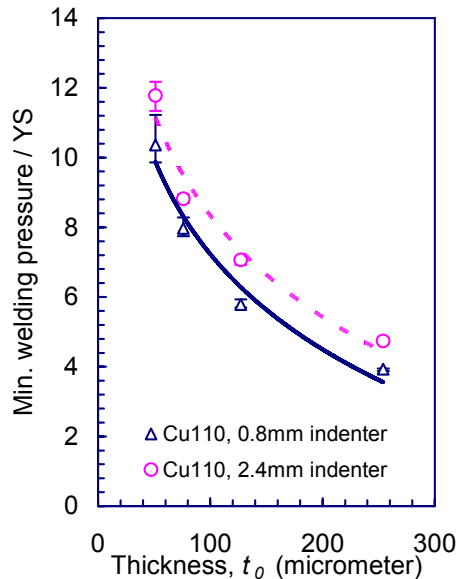


Figure 5-6: Effect of indenter size on the minimum welding pressure

5.3.4 Effect of Welding Pressure on Bond Strength

To investigate the effect of the welding pressure (i.e., thickness reduction) on the bond strength of different material blanks under different process conditions, tensile tests were conducted on the bonded specimens under normal loading condition as shown in Figure 5-7. The bond strength is found to increase with the thickness reduction ratio for both Cu110 and Ni200 up to a certain point, after which the bond strength would

decrease as more deformation is introduced to the specimens. At higher values of the thickness reduction ratio, the bonded specimens become very thin at the weld location leading to fracture. During the tensile test, these specimens would break at these thinning spots along the edges of the weld line, instead of at the spot of the weld itself which would be expected at a lower reduction value. This reduction ratio is directly dependent on the welding pressure. Therefore, there exists an optimal welding pressure at which the bond strength is a maximum. This optimal welding pressure value is a material and process dependent parameter.

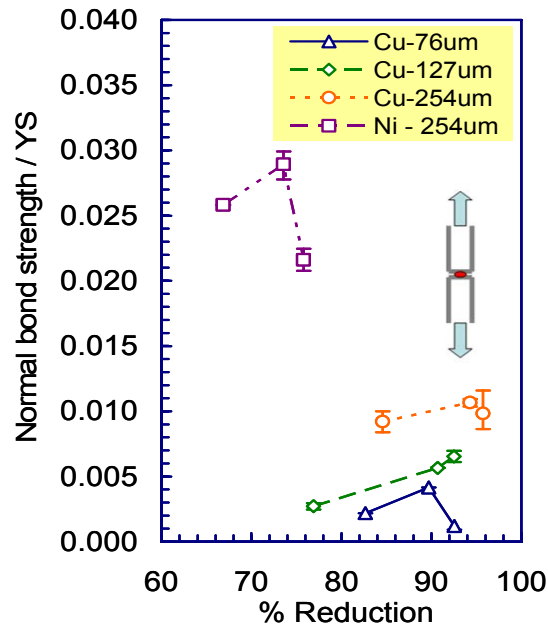


Figure 5-7: Effect of welding pressure on the bond strength under normal pull tests

5.3.5 Effect of Welding Temperature on Bond Strength

Welding experiments at elevated temperature levels of 150°C and 300°C were performed on thin blanks of Ni200 and SS304 both with the initial thickness of 51 micrometers. The nickel and stainless steel thin sheets with this specific thickness were selected because they could not be joined in the cold condition as discussed in the

previous section. Based on the experimental results shown in Figure 5-8, successful bonding of both nickel-to-nickel and stainless steel-to-stainless steel blanks occurred at the minimum welding pressure between 8 to 10 times of the material yield strength value (YS of Ni200 = 148 MPa, YS of SS304 = 215 MPa) for the two selected temperature levels. The material strength seemed to be slightly lower with increasing temperature as more thickness reduction was observed at the similar pressure level, but at different temperature levels. This mechanism, i.e., material softening due to temperature, as well as the breaking up of contaminant layers at elevated temperatures may be the main reason behind the successful bonding of these materials in the warm condition as compared to the cold condition. Since plastic deformation is the fundamental bonding mechanism in this pressure welding process, materials with high ductility and low strength would provide better plastic flow; thus, more likely to bond at lower welding pressure levels. Nonetheless, the threshold reduction for bonding nickel at 150°C and 300°C is around 50% and 35%, respectively, and that for stainless steel is approximately 55% at both temperature levels. On the other hand, Figure 5-8b showed a significant effect of the temperature on the bond strength in that the bond strength increases with increasing welding temperature. The bond strength of about 16%-18% of the material yield strength could be obtained at 300°C for both materials and at this temperature level, the increase in deformation (i.e., thickness reduction) does not have significant impact in terms of improving the bond strength. However, at a lower temperature level of 150°C, the level of deformation appeared to improve the bond strength as shown in Figure 5-8b. The effect of temperature on the bonding mechanisms is investigated in the next section.

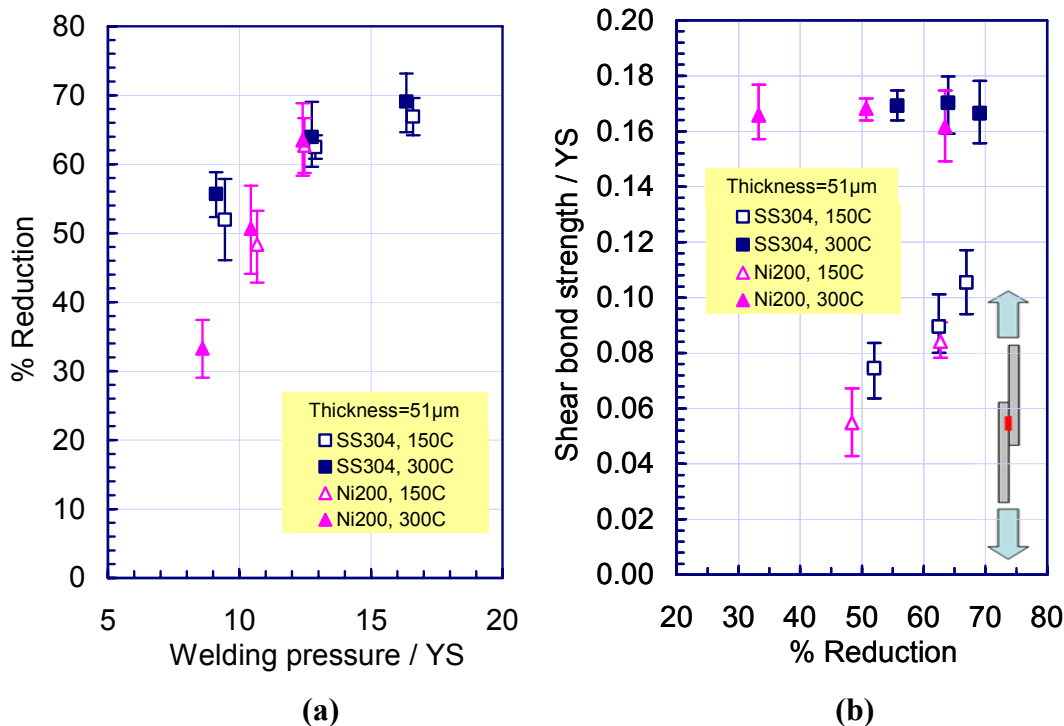
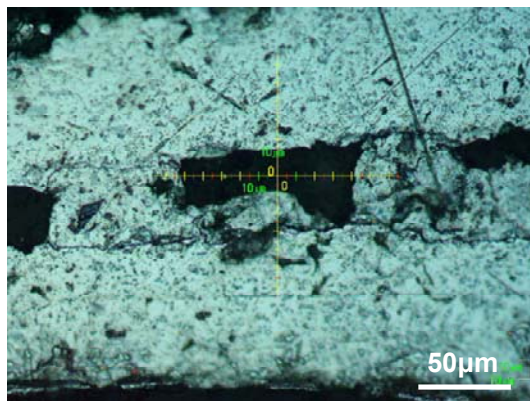


Figure 5-8: Effect of welding temperature on thickness reduction and bond strength

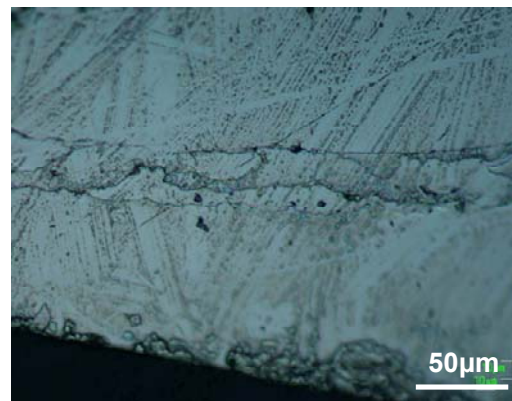
5.3.6 Microstructure of Bond Formation

The microstructure of the bond formation area is shown in Figure 5-9 for both Al3003 ($t_0 = 158 \mu\text{m}$) and Ni201 ($t_0 = 127 \mu\text{m}$) specimens which were bonded at a room temperature, and for Ni200 ($t_0 = 51 \mu\text{m}$) and SS304 ($t_0 = 51 \mu\text{m}$) specimens which were bonded at elevated temperatures. In the case of aluminum (Figure 5-9a), bonding was found to take place at certain locations where the oxide layers fractured. The dark spots (voids) represented the sections where the oxide layers did not fracture. On the other hand, bonding of Ni201 (Figure 5-9b) was shown to occur throughout the contact interface with no sign of contaminant layer. Only the use of compressive force/pressure was shown to be sufficient to break up the oxide layers and bond aluminum-to-aluminum and nickel-to-nickel blanks at the room temperature. However, for thinner gauge of

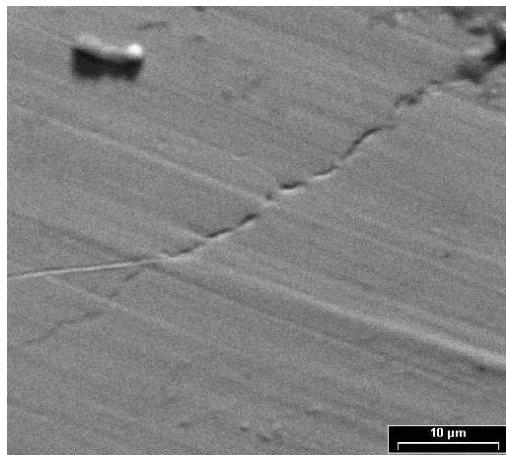
nickel (thickness < 100 μm) and stainless steel, the use of heat was required to bond the samples. At elevated temperatures, the plastic deformation at the contact interface is enhanced through softening mechanism of the contaminant layers as well as the base material. Scanning electron microscope (SEM) images of the bonding regions for both Ni200 and SS304 samples at elevated temperature levels are shown in Figure 5-9c-d. These images showed the bonding mechanism at the contact surfaces to still be based on the plastic deformation and not by melting or diffusion process.



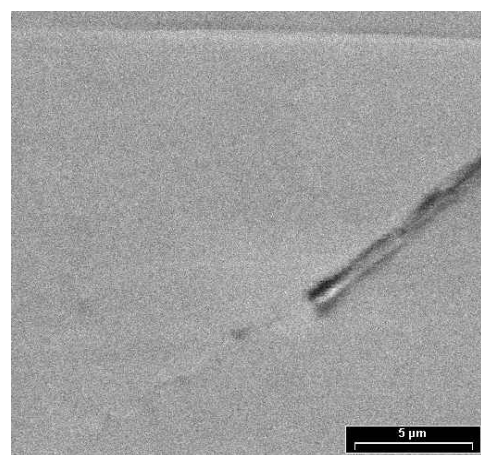
(a) Al3003 at room temperature



(b) Ni201 at room temperature



(c) Ni200 at 150°C



(d) SS304 at 300°C

Figure 5-9: Optical microscope images at the bonding sites for (a) Al3003 and (b) Ni201 at room temperature, and SEM images for (c) Ni200 and (d) SS304 at elevated temperature levels

5.4 Summary and Conclusions

The effects of various material and process conditions on the minimum welding pressure and bond strength were investigated and characterized in this study. A summary of the results and findings is presented as follows:

1. Copper, aluminum, and nickel blanks with the sheet thickness in sub-millimeter range (51 – 254 micrometers) can be cold welded, while stainless steel blanks cannot be bonded by cold welding even at the high pressure level.
2. Thinner blanks have been shown to require more welding pressure than thicker ones. When the sheet thickness is reduced, especially below 100 micrometers, the material response is dominated by the grain size and orientation as can be seen from the large scattering of the data.
3. There exists an optimal value of the welding pressure where the maximum bond strength could be obtained. This value is material and process dependent.
4. Brushed surface condition helps decreasing the minimum welding pressure while increasing the bond strength. Wet condition does the opposite.
5. Bonding of thin nickel ($t_0 < 100 \mu\text{m}$) and stainless steel blanks is possible at elevated temperature levels between 150-300°C. The bond strength was found to increase with an increase in welding temperature. Thickness reduction

amount of 50%, 35%, and 55% are required to bond nickel blanks at 150°C, 300°C, and stainless steel blanks at both 150°C or 300°C, respectively.

6. A small difference in minimum welding pressure values was observed when two different indenter sizes were used. Narrower indenter appears to require slightly less welding pressure than a wider indenter.
7. For two metal blanks to bond under compressive pressure, it is imperative that the covering layers on the specimen surfaces have to be fractured or better yet completely removed to allow fresh material underneath to flow through to create the metallic bonding. One of the common ways to fracture these contaminant layers is by using conventional scratch brushing technique. Heating of the specimens was shown to facilitate the material flow as well as weaken the contaminant layers at the surfaces.
8. Microstructure analyses of the bonding mechanisms both at cold and warm temperature conditions showed that the bond formation in the pressure welding process of sheet metal blanks to be based on the plastic deformation of the two metal blanks, and not by melting or diffusion process.

These findings will be utilized in the next chapter to design the process for making double bipolar plates in a single-step and single-die operation.

CHAPTER 6: NUMERICAL AND EXPERIMENTAL INVESTIGATIONS OF THE HYBRID MANUFACTURING PROCESS

6.1 Introduction

In the previous chapters, successful hydroforming of micro-channels and mechanical bonding of thin stainless steel 304 blanks of 0.051 mm-thick have been experimentally demonstrated and characterized in two separate test setups. In this chapter, the understanding and findings from those experiments are utilized in the design and development of a new test setup that can perform both hydroforming and mechanical bonding in a single-die and single-step operation. Nevertheless, prior to the finalization of the new die design, FEA of the hybrid process is performed to evaluate the producibility of the double bipolar plates with selected micro-channel geometries and flow field configuration as suggested in the parametric study (Chapter 4) and in the literature. Furthermore, effects of different process parameters, such as forming pressure and punch velocity profiles, on the overall formability and bond strength of the double bipolar plates are also characterized using the FE tool. Finally, the new set of tooling is developed and tested as will be discussed at the end of the chapter.

In the following section, a review of existing designs for the micro-channel geometries and the flow field configurations on the fuel cell bipolar plates is presented. Based on this review and the results from the parametric study in Chapter 4, a set of channel geometries and flow field design is selected and used for the process feasibility

study in the FEA. In addition, the effect of pressure and punch stroke as well as their synchronization is considered in the FEA. The FE models of the hybrid process that are developed in this study can be used to evaluate the producibility of different designs of the bipolar plates. In the last section of this chapter, a new tooling design for the hybrid manufacturing process is discussed with some preliminary results that show the promising potential of this proposed hybrid manufacturing process as a solution to reduce the cost of bipolar plate fabrication, while improving the dimensional accuracy and assuring the consistent contact resistant throughout the plates.

6.2 Literature Review on Micro-channel and Flow Field Configuration

Micro-channel and flow field configuration design is another on-going research topic in the field of fuel cell development. The size of the micro-channels and the design of the flow field configuration have been reported in a number of literatures to significantly affect the fuel cell performance, durability, and reliability [*Kumar, 2003; Cha, 2004; Feser, 2006*]. In general, the two main concerns involved with the design of the micro-channel and flow field configuration in the PEMFCs are (1) the convection mass transport rate of the reactants at the contact surface between the bipolar plates and the gas diffusion layers (GDL), and (2) the water removal rate on the cathode side of the bipolar plates. High convection mass transfer and effective water removal on the cathode side can be achieved by increasing the velocity and pressure of the reactant flows. One way to increase the flow velocity is by simply down-scaling the micro-channel dimensions [*Cha, 2004*]. However, there is one major issue concerning with the down-scaling of these micro-channels. That is a significant drop in pressure near the flow outlet is observed with the miniaturization of the micro-channels, leading to a flooding

problem at the diffusion layer in this area.

The range of the micro-channel geometries (width and height) for the bipolar plates for both lab-scale testing and pilot fuel cell units in the industry is between 0.1 and 1.5 mm on a plate size between 14 x 14 mm [Cha, 2004] and 40 x 40 mm [Kumar, 2003]. Different flow field configurations have been designed and tested to evaluate the cell performance. Notable configurations include serpentine, interdigitated, and parallel. Each design has its pros and cons. For examples, serpentine, a widely used flow channel configuration for modern fuel cells (also known as “industry standard” [Feser, 2006; Li, 2007], has a single flow routing which is good for the reactants and water removal purpose, but a very long channel length of this configuration would lead to a significant drop in pressure at the outlet [Cha, 2004]. Nonetheless, the large pressure differences between the adjacent channels may improve the performance by “channel bypass” mechanism as discussed in [Feser, 2006]. The channel bypass occurs when the reactants move from one channel to the next through the porous gas diffusion layers (GDL) under the lands of the bipolar plates. Interdigitated channel configuration, on the other hand, provides better performance (i.e., power density) as compared to the serpentine because of the higher forced convection mass transfer at the gas diffusion layers. However, some channels might not be functioning because of the unstable flow routing and flooding associated with this type of flow field configuration.

Kumar and Reddy [Kumar, 2003] studied the effect of channel geometries (e.g., width, height, and spacing/land width) and shape (e.g., rectangular, triangular, and hemispherical) on the pressure drop value to reflect on the hydrogen consumption at the anode, and thus, the cell performance of different channel designs. They found that for

a rectangular channel shape, the optimal channel width (W), channel depth (H), and land width (W_L) were found to be 1.5 mm, 1.5 mm, and 0.5 mm, respectively, within the studied range between 0.5 and 4.0 mm for each dimensional parameter. In fact, they suggested the use of even smaller land width to obtain higher hydrogen consumption at the anode. However, small land width would increase manufacturing cost (machining or casting). In addition, the study showed that the maximum pressure drop in the case of the hemispherical, triangular, and rectangular channels were 92.9%, 92.5%, and 84.8%, respectively. These values were obtained from the simulations with the channel geometries given in Table 6-1.

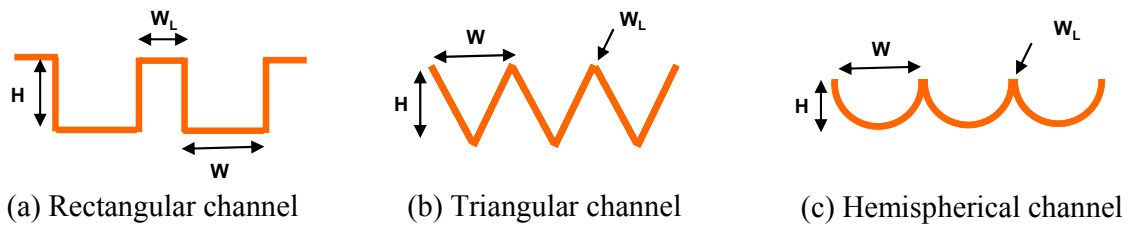


Figure 6-1: Different channel shapes

unit [mm]	Rectangle	Triangle	Hemisphere
Channel width, W	1.5	1.5	1.5
Channel depth, H	1.5	1.5	0.75
Land width, W_L	0.5	~0	~0

Table 6-1: Optimal channel geometries for maximum hydrogen consumption at anode [Kumar, 2003]

Another performance study was conducted by Cha et al. [Cha, 2004] on square-channel with the channel size between 0.005 and 1.0 mm. The results showed the optimal power density at the channel size of about 0.5 mm. Further down-scaling of the channel size for all three flow field configurations studied in their work (i.e., interdigitated, serpentine, spiral-interdigitated) did not improve the cell performance, and

a significant pressure drop was observed which would lead to the flooding problem.

Combining above design suggestions for the micro-channel geometry and flow field configuration with the results learned from the parametric study in Chapter 4, a design of bipolar plate geometry for the feasibility and characterization study in FEA is chosen to have a *parallel flow field* configuration with a 0.5 mm channel width and height as suggested in [Cha, 2004] for a maximum power density as well as according to the design guidelines to choose a channel width, W , between 5-10 times of the sheet thickness, t_0 (0.051 mm). The land width (W_L) was suggested to be made as small as possible [Kumar, 2003], however due to issues in manufacturability and die life, the *land width of 0.5 mm with a corner radius of 0.125 mm* are chosen in this study. In addition, for the pressure welding purpose and according to the suggested shape of the micro-channel by [Kumar, 2003], the shape of the channel at the *valley area is selected to be hemi-spherical with a radius of 0.25 mm*. A draft angle (α) of 0° is selected based on results from the parametric study that is recommended to make as small as possible to maximize the cross-sectional area of the channels in order to avoid a large pressure drop across the plate.

Combining these channel geometries as discussed above, the final shape of the bipolar plates is illustrated in Figure 6-2. In the FEA study, a square active area of $10 \times 10 \text{ mm}$ is chosen for the demonstration purpose in order to shorten the simulation time. However, the FEA results could be applied to the process design of a larger plate size by scaling up the process parameters (e.g., forming pressure, holder/clamping force, heating time, welding force, etc.) that are involved with the hybrid manufacturing process accordingly.

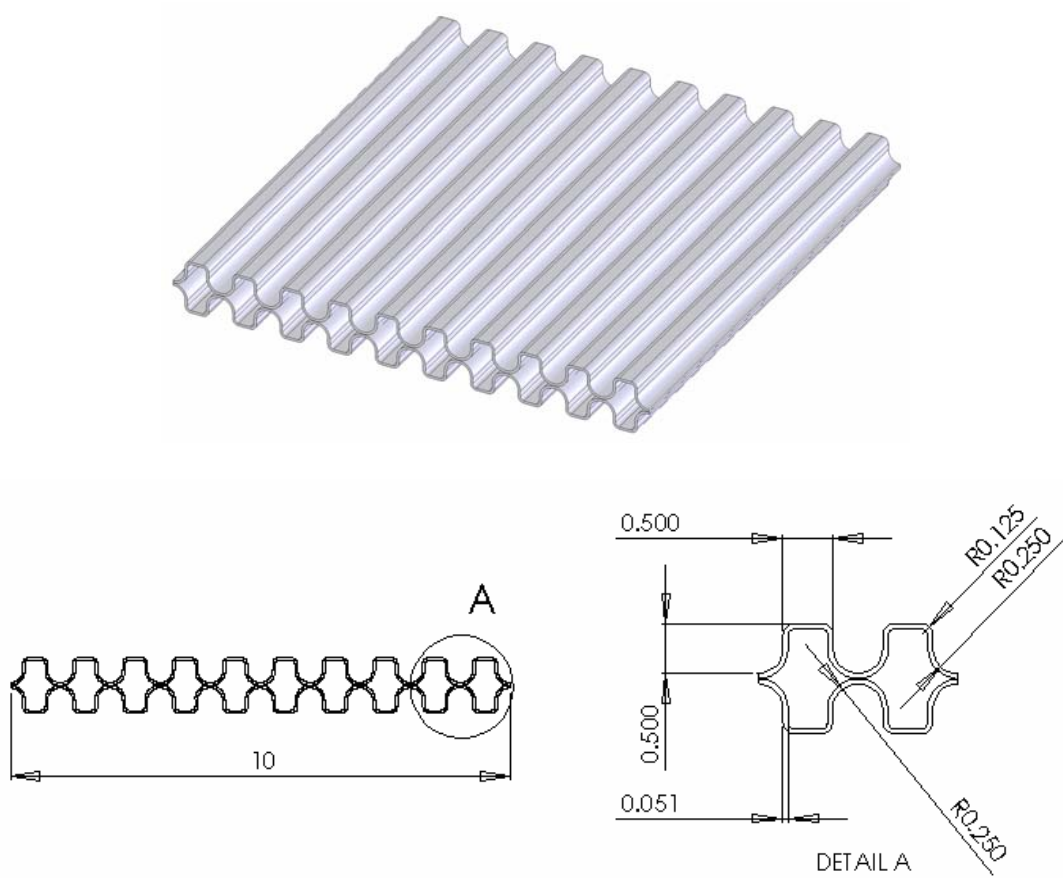


Figure 6-2: Selected micro-channel array design of double bipolar plates

6.3 FE Modeling of the Hybrid Process

This section describes the criteria and modeling steps that are taken during the construction of the FE models of the hybrid process. First, the mechanical bonding criteria of thin SS304 blanks are presented. Second, since the pressure welding of SS304 blanks are only successful at elevated temperature levels, a new warm hydraulic bulge testing setup is developed for the material testing at elevated temperature levels. Finally, the welding criteria and material properties at elevated temperature are used in

the FE models. The boundary and loading conditions of the process are then discussed at the end of this section.

6.3.1 Pressure Welding Criteria

Pressure welding of thin SS304 blanks (thickness below 100 micrometers) was found to be successful only at elevated temperatures as discussed in Chapter 5. Two temperature levels of 150 and 300°C were used and the test results are recaptured in Figure 6-3. The effect of welding temperature was shown to significantly increase the quality of the bond (i.e., bond strength). For example, bond strength of 6-9% of the material yield strength (YS of SS304 = 215 MPa) could be obtained when welding was carried out at 150°C. This value increased to be about 15-18% when the test is performed at 300°C. However, the increase in the welding temperature did not suggest any reduction in the minimum welding pressure (i.e., the threshold reduction) value. At both temperature levels, about 55% deformation (i.e., thickness reduction) was shown to be the threshold reduction value for bonding the thin SS304 blanks. As a result, this *55% threshold reduction* will be used in the simulation as the criteria for the bond formation.

In addition, since there is no moving component inside the fuel cell stack and the whole stack is held and clamped tightly together by the two end plates to prevent any leaking of the reactants or water, the bonding between the two bipolar plates would not undergo a very high loading. The purpose of the bond between the two plates is therefore to assure the high dimensional accuracy and the consistent contact resistant, leading to improvement in cell performance. With this reason, the welding temperature

of 150°C is selected to be modeled in the FEA in order to simulate a more difficult-to-form with moderate bond strength as compared to the 300°C that would require an undesirable longer heating time. Nonetheless, in order to accurately model this process in the FEA, the material properties at the elevated temperatures should be used. Therefore, in the following section, a warm hydraulic bulge test setup is developed to conduct the test on thin SS304 blanks in order to obtain the material flow curves at the elevated temperature levels of 150 and 300°C.

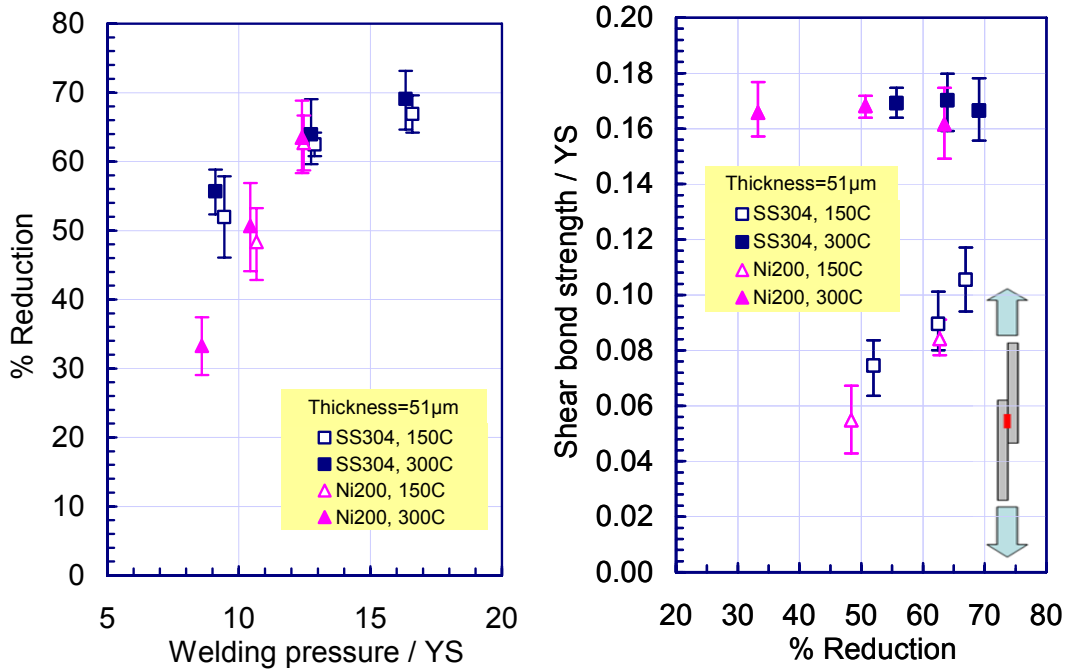


Figure 6-3: Effect of welding temperature on thickness reduction and bond strength

6.3.2 Material Flow Curves at Elevated Temperatures

In this section, additional bulge tests are conducted at the elevated temperature levels (150 and 300°C) in order to obtain accurate material flow curves to be used in the FEA of the hybrid process. As discussed in Chapter 4, the flow curves obtained from the bulge size at the macro/meso-scale (2.5 – 100 mm) failed to provide accurate

predictions in terms of the channel formability at the room temperature. However, due to the limited resource of the experimental dies and equipment, the 100 mm bulge diameter, which is made out of H13 tool steels rather than a D2 material as in the case of the smaller die setup with 2.5, 5, 10 and 20 mm bulge diameters, is selected to be used to conduct the warm bulging tests in this section.

The warm hydraulic bulge test apparatus developed in this study is illustrated in Figure 6-4. The setup is composed of four major systems which are (1) a pneumatic/hydraulic system: pump (Hydratron AZ-2-180HPU-LW), pressure controller (Marsh Bellofram Type 3510), and pressure transducer (OMEGA PX605), (2) a set of bulging die: upper and lower die with a bulge diameter of 100 mm, clamping and sealing mechanism (silicone based O-ring), (3) heating system: cartridge heaters, temperature controller (OMEGA CN616tc1), and thermocouples (Type K), and (4) in-die non-contact measurement systems: laser sensor (Keyence LK-G402). The non-contact measurement system is used rather than a contact type to avoid any temperature gradient due to the heat transfer at the contact location at the dome apex, and to prevent the equipment damages from hot pressurized oil (Marlotherm SH) at bursting. With this setup, the temperature is monitored and controlled independently at the upper and lower die halves by using two separate sets of cartridge heaters and thermocouples (t/c) as shown in the setup/control diagram in Figure 6-5. The temperature variation during the test was found to be below 5°C with respect to the set value. In addition, with the use of LabView program, DAQ (Data Acquisition), and PID controller, the strain rate (SR or $\bar{\dot{\epsilon}}$) is also controlled and maintained at a constant value during the tests. The effect of the strain rate on the material response is critical, especially at elevated temperature levels, and thus, the strain

rate is carefully controlled in this study. A feedback control loop is developed in the LabView program for this purpose. The program receives instantaneous dome height reading from the laser sensor as the input signal to the control loop, and uses the pre-calculated dome height profile as the reference values. Based on the difference between the input and reference signals, the PID controller in the loop sends control signals to the pressure controller in order to regulate the air pressure and flow rate that will be supplied to the pump (i.e., intensifier). The connection loop between the pneumatic/hydraulic system and the non-contact measurement system (laser sensor) is also shown in Figure 6-5.

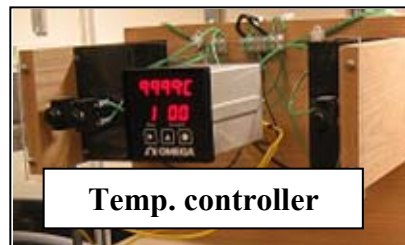
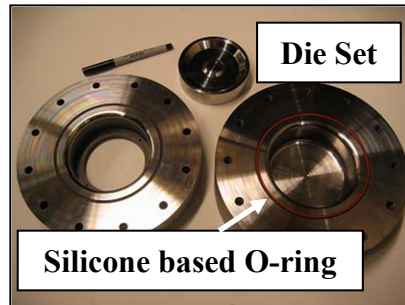
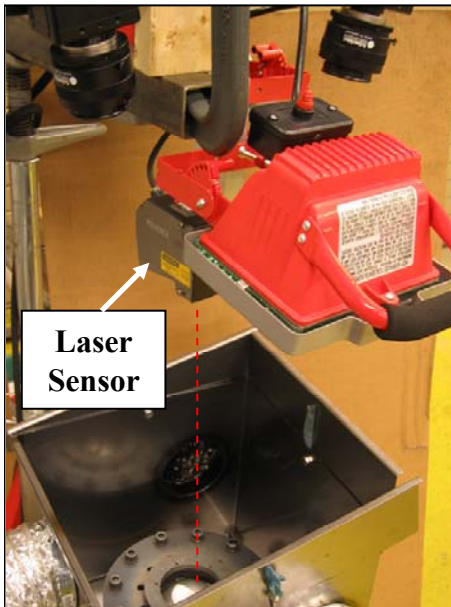
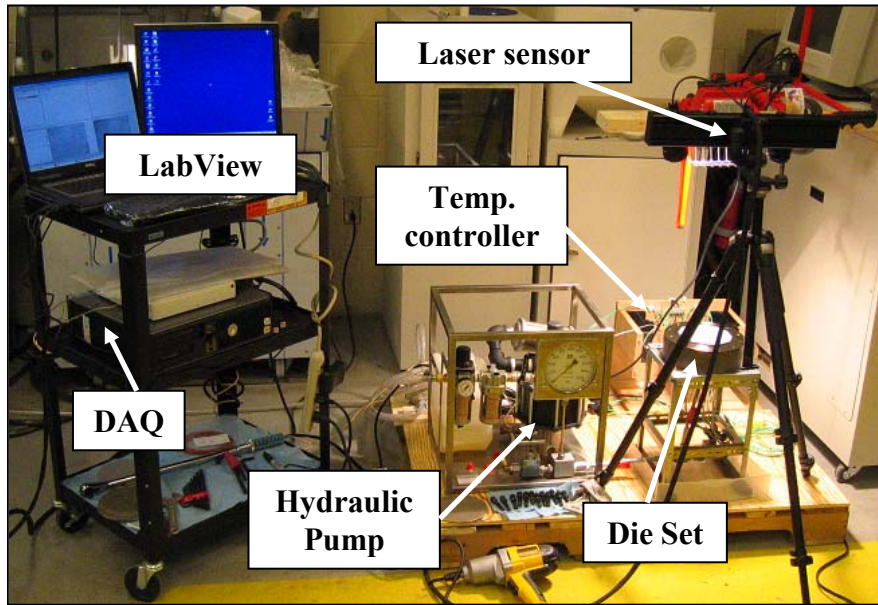


Figure 6-4: Warm hydraulic bulge testing setup

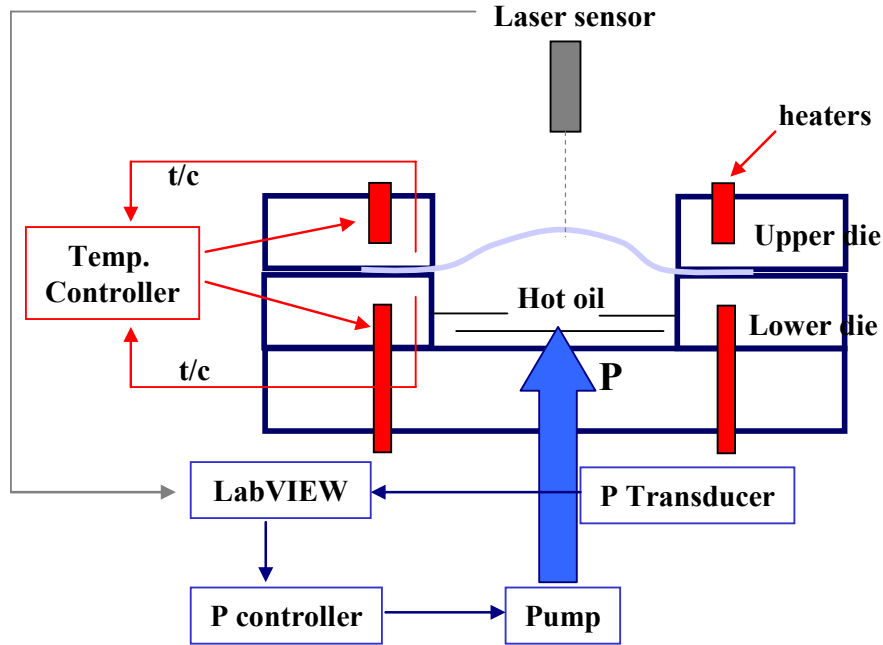


Figure 6-5: Schematic diagram of the warm bulge test setup

The pre-calculated dome height (h_d) profile for a constant strain rate control was derived based on the geometrical relationships in a circular bulge testing of thin sheet blanks as follows [Hill, 1950]:

$$\bar{\varepsilon} = \ln\left(\frac{t_0}{t_d}\right) \quad \dots (6-1)$$

$$t_d = t_0 \left(\frac{d_c^2}{d_c^2 + 4h_d^2} \right)^2 \quad \dots (6-2)$$

where $\bar{\varepsilon}$ is the equivalent strain, t_0 is the initial sheet thickness, t_d is the instantaneous apex thickness, d_c is the bulge diameter, and h_d is the instantaneous dome height. In addition, since strain rate ($\dot{\bar{\varepsilon}}$) is the rate of change in strain, we can write:

$$\bar{\varepsilon} = \dot{\bar{\varepsilon}} \cdot t \quad \dots (6-3)$$

where t is time. Combining equation (6-1) – (6-3), we obtained a relationship between

the instantaneous dome height (h_d) and the strain rate ($\dot{\epsilon}$) as:

$$h_d = \frac{d_c}{2} \sqrt{e^{\dot{\epsilon} t / 2} - 1} \quad \dots (6-4)$$

Typical dome height profiles at various strain rate levels were plotted as a function of time and shown in Figure 6-6. These profiles were used as the reference input of the dome height (h_d) in the feedback control loop. In this study, a relatively slow strain rate ($\dot{\epsilon}$) of 0.002 s^{-1} is used for all of the tests.

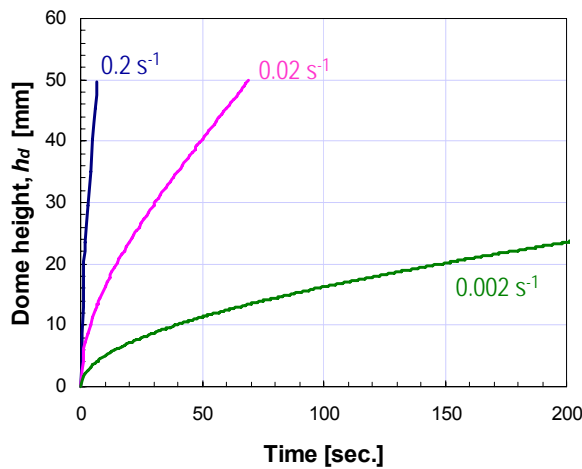


Figure 6-6: Typical dome height profiles for different strain rate levels

During each test, the bulging pressure was continuously measured using a pressure transducer, while the dome height was continuously recorded using the laser sensor. These pressure and dome height data were synchronized together by the time stamp during the test, and later used for the flow curve calculation based on the methodology discussed in Chapter 3. Material properties obtained from different testing temperature levels are presented in Table 6-2 and the plots of these flow curves are shown in Figure 6-7. The flow curves were shown to be lower at the elevated temperatures.

SS304, $t_0=51\mu\text{m}$, $d=10.6\mu\text{m}$	100 mm bulge diameter: $\sigma = K \epsilon^n$		
	Room	150°C	300°C
K [MPa]	1,266	1,052	1,043
n	0.47	0.46	0.49

Table 6-2: Material properties at elevated temperatures

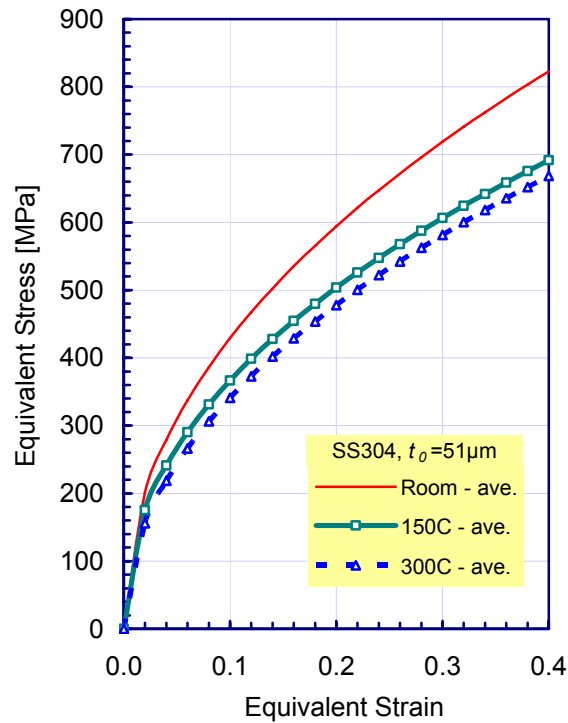


Figure 6-7: Flow curves of thin SS304 sheet (51 μm-thick) at different temperature levels

6.3.3 FE Models – 2D Isothermal Simulations

Based on the selected micro-channel geometries and flow field configuration in section 6.2, the bonding criteria discussed in section 6.3.1, and the material flow curves at elevated temperatures obtained in section 6.3.2, a full 2D isothermal simulation model of the hybrid process is constructed and shown in Figure 6-8.

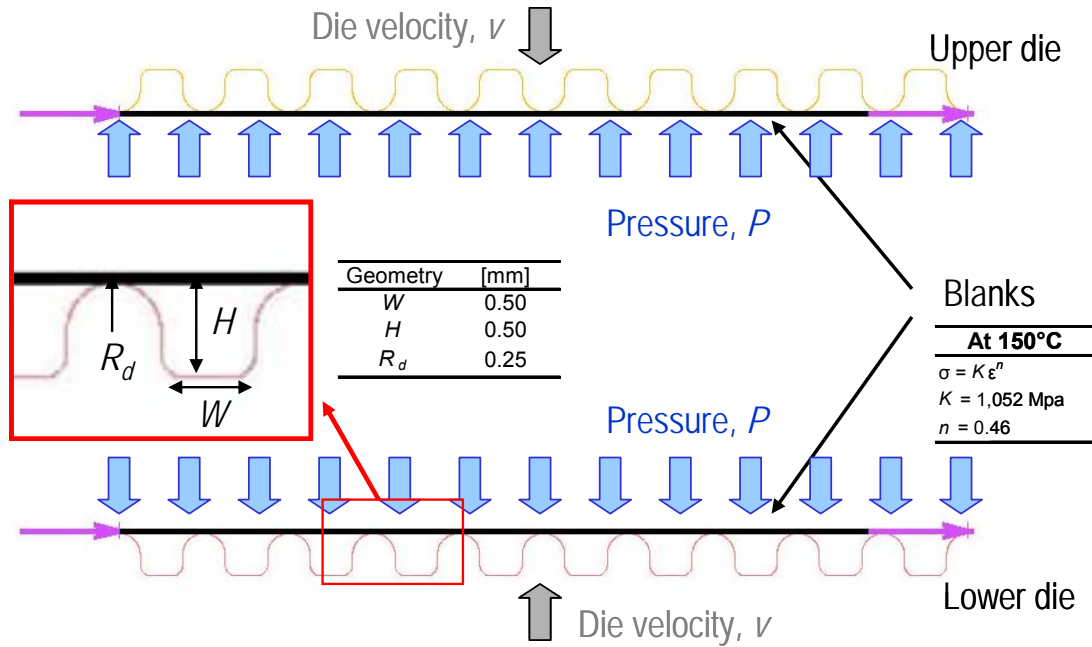


Figure 6-8: FE Models of the hybrid process

The upper and lower dies are modeled as rigid bodies. Solid elements are used to model the deformable blanks with four elements across the thickness. The displacements at the nodes at both ends of the blanks are fixed in the X- and Z-directions; thus, the blanks can only move in the vertical direction (Y-direction). The material flow curve obtained from the warm bulge tests at 150°C is assigned to all deformable elements. Coulomb friction condition with the friction coefficient of 0.03 is assumed at the contact surfaces. The hydrostatic pressure with prescribed pressure profiles (using table input) is applied at the edge of the deformable elements from the inner sides as shown in Figure 6-8. The die velocity profiles are also prescribed by using table input. The pressure and die velocity profiles that are used will be discussed in the following section.

6.3.4 Hybrid Process Characterization

In this section, the effect of different loading profiles (pressure and die stroke/speed) on the micro-channel hydroformability and the bond strength between the two metal plates are investigated. Three different profiles of pressure and die velocity (Figure 6-9) are used in a design of experiment (DOE) study with the full factorial method. The DOE matrix can be found in Table 6-3. In addition, since the current simulation problem is axisymmetric, in order to save simulation time only the bottom half of the models is simulated as shown in Figure 6-10.

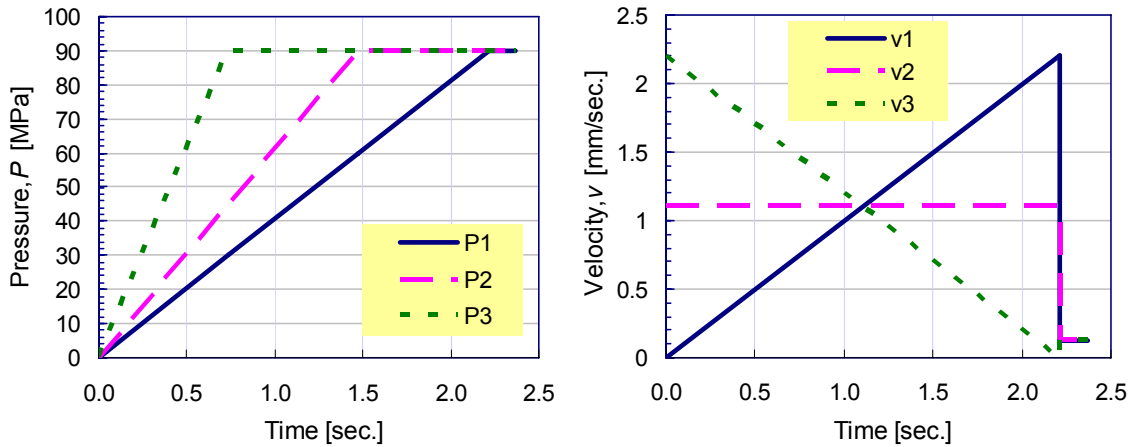


Figure 6-9: Pressure and velocity profiles

case	P	v
1	1	1
2	1	2
3	1	3
4	2	1
5	2	2
6	2	3
7	3	1
8	3	2
9	3	3

Table 6-3: DOE matrix for simulation runs

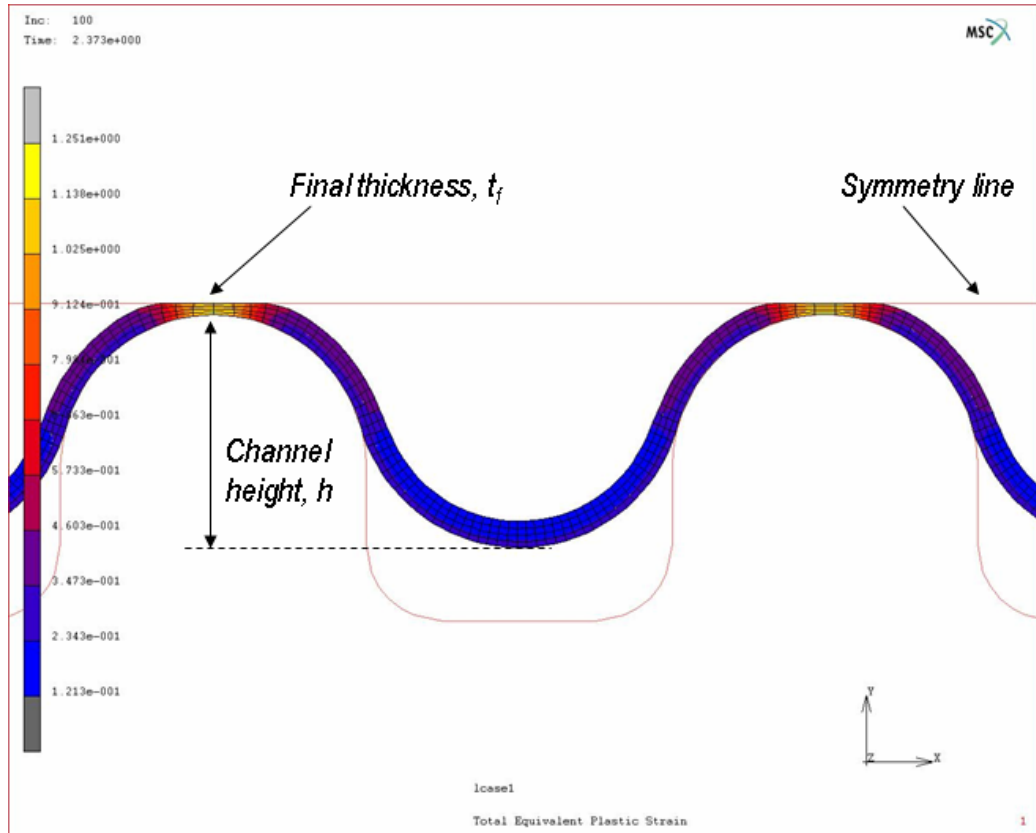


Figure 6-10: Axisymmetric model of the hybrid process

The output parameters of interest are the channel height (h) as the measure of the channel formability, and the final thickness (t_f) value at the contact locations as the measure of the percentage reduction of the blank thickness, and thus, the bond strength. The results from the nine simulation cases are presented in Figure 6-11.

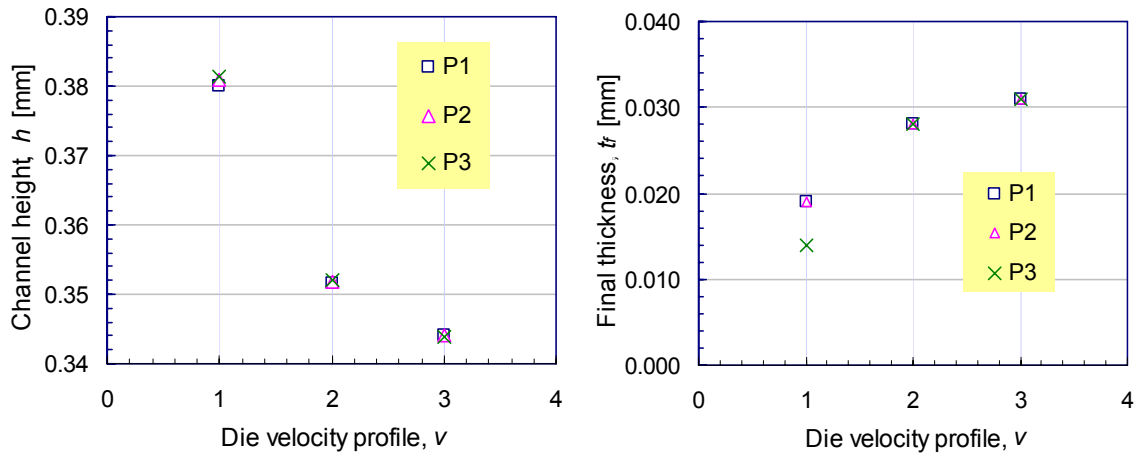


Figure 6-11: Effects of pressure and die velocity profiles

Due to the relatively short process cycle time of about 2.4 seconds in the simulation, the effect of the forming pressure (P) slope (i.e., forming rate) was found to be insignificant on the channel formability for all three velocity profiles (i.e., increasing, constant, and decreasing profiles). On the other hand, the effect of the die velocity profile (v) was found to be critical to both formability and bond strength. That is with increasing die velocity profile (v_I), both channel height (formability) and thickness reduction (bond strength) values were found to increase significantly. No interaction effect between the two process parameters (P and v) was observed. The preliminary investigations conducted here to characterize the effect of the process conditions showed that with properly selected forming pressure and die velocity profiles, both channel formability and bond strength could be further enhanced. Since this current study is focused on the producibility issue, the process optimization study is not included here. Nonetheless, the profiles of the pressure and velocity of the punch strokes used in the FEA in this section, which were shown to be legitimate, will be implemented in the actual experimental tests of the hybrid process in the following section.

6.4 Hybrid Process Development

In this section, all of the experimental and simulation results and findings so far in this study are used to finalize the experimental design setup for the proposed hybrid manufacturing process in a single-die and single-step operation. Since in the previous section, it was shown that a typical ramp-up pressure profile is legitimate for the hydroforming of micro-channel arrays, the setup that is developed in this section is designed without the necessary use of a high pressure pump. Instead, the pressure is designed to build up due to the compressive loading that is supplied by the stamping press. Nonetheless, later on if different pressure profiles should be used, a high pressure pump could easily be attached on the side of the die as illustrated in Figure 6-12.

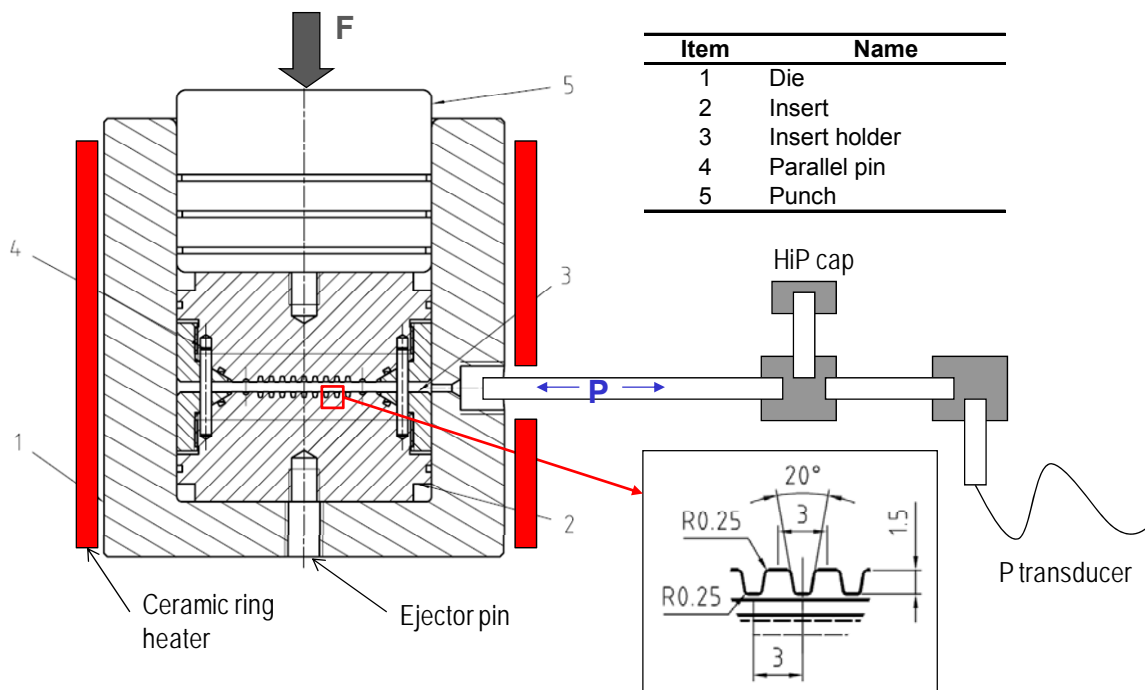


Figure 6-12: Development of hybrid die – setup

The hybrid process setup is composed of six major die pieces – one die (#1), two inserts (#2), two insert holders (#3), and one punch (#5) as shown in Figure 6-12. A set of ceramic ring heater, capable of heating up to 600°C, is attached to the die, which also has a hole of one inch size in diameter on the side to allow high fluid pressure to be supplied into the die chamber. A handheld temperature meter with a K-type thermocouple is used to measure the temperature of the die setup. The fluid pressure is measured using a pressure transducer (OMEGA PX605 – 20K), which is attached at the end of the hosing system, away from the warm region of the die. A high pressure cap (HiP cap) is used for the filling and draining purpose of the fluid media (Marlotherm SH oil) in the die chamber. The challenging design aspect lies in the clamping of the thin blank on the surface of the die insert without allowing the fluid media to flow behind it (i.e., between the blank and the die insert). This challenge is tackled by using an insert holder that acts as a cap to clamp the sheet blanks on top of the insert face, and to prevent the fluid media to flow behind the blanks. The two sets of insert and insert holders are aligned to each other using two alignment pins as shown in Figure 6-13. Notice that less aggressive channel design is selected here for the demonstration purpose. However, smaller channel dimensions with more complex flow field configurations could also be tested with this die set by simply changing the insert pieces. The image of the die components and the actual experimental setup on the stamping press are shown in Figure 6-14 and Figure 6-15, respectively. A typical pressure profile that is recorded during the test is shown in Figure 6-16.

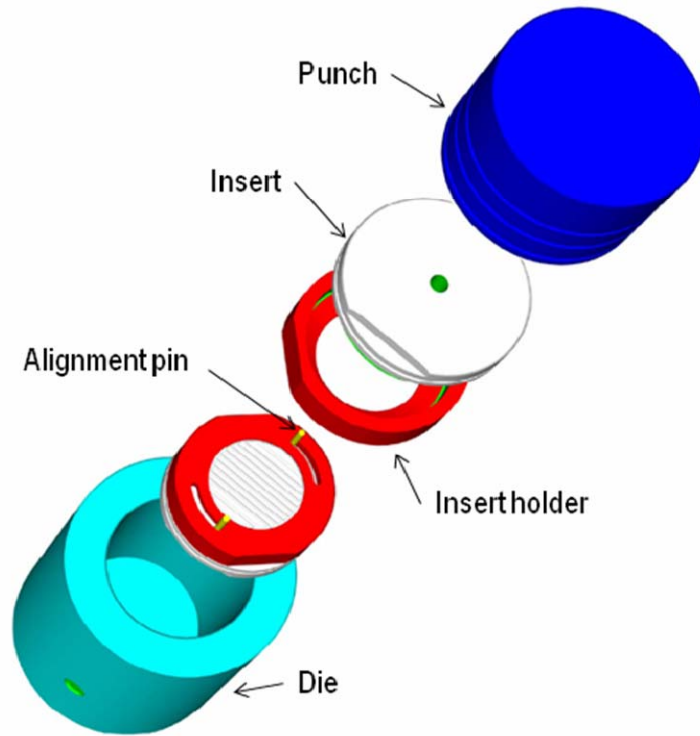


Figure 6-13: Die assembly



Figure 6-14: Die components

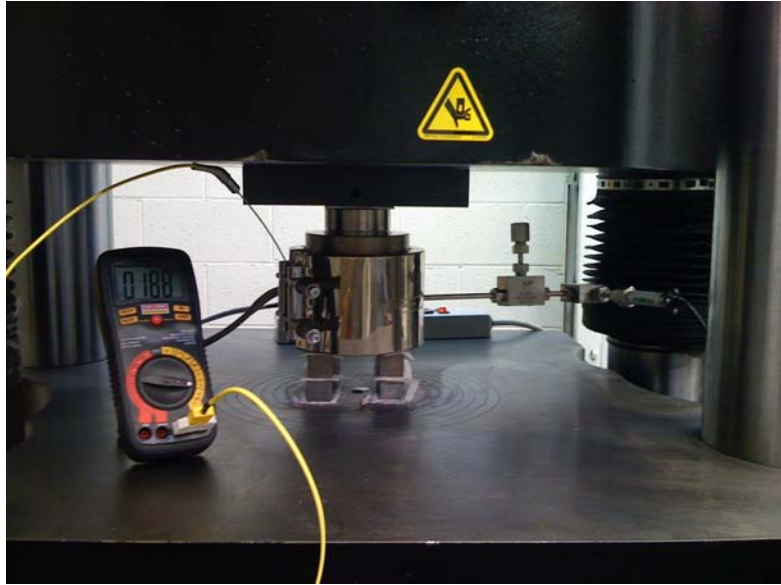


Figure 6-15: Experiment setup

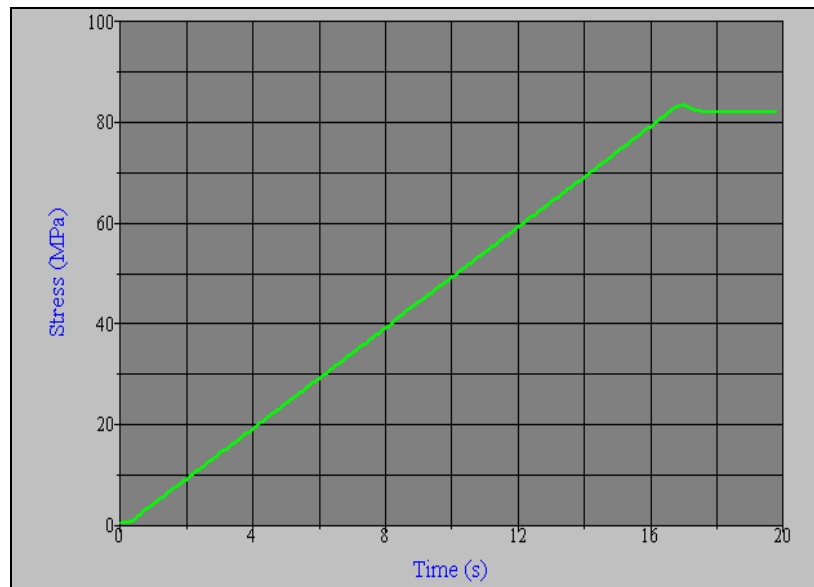


Figure 6-16: A typical pressure profile used in the test

The experimental results showed successful forming of micro-channels on both sides (the upper and the lower blanks), Figure 6-17a. Therefore, two bipolar plates could be formed in a single-step and single-die operation with this process design setup

by using the ramp-up pressure profile that was generated by pure compressive loading (i.e., no pump). In addition, a small variation in terms of the channel height between the channels from the left to the right of the arrays is shown to be less than 30 micrometers (Figure 6-17b).

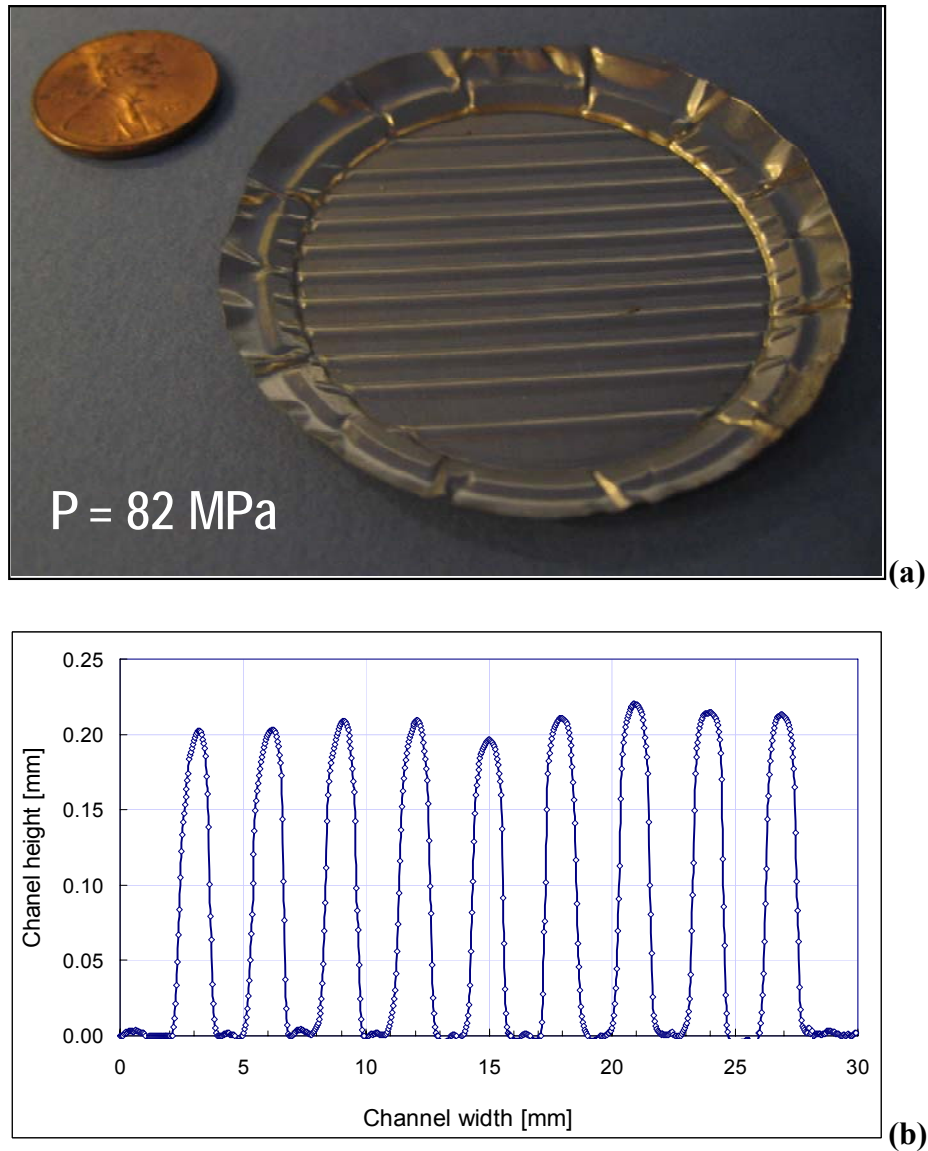


Figure 6-17: (a) hydroformed channels on SS304, 51 μm -thick, and (b) channel profile at 82MPa

Unfortunately, even though the welding spots were created at the location of the two welding pins/indenters, due to a minor design mistake the removal of the specimens cannot be done without damaging the weld spots. Nonetheless, this tooling design is shown to be capable of creating double bipolar plates with micro-channel arrays on both sides and bonding the two blanks together at the end of the stroke in a single-step and single-die operation, proving the conceptualized manufacturing process to be valid and feasible. In the future, the assembly of the insert and insert holder should be modified so that the insert can be removed vertically without having to rotate (i.e., unthread). After one of the insert pieces is disassembled from its insert holder, a trimming operation can be used to trim out the double bipolar plate that is produced at the middle between the two inserts.

6.5 Summary and Conclusions

In this chapter, a review of the micro-channel geometry and flow field design for the PEMFC bipolar plates is presented. Based on the recommendations in the review for optimum cell performance, along with the micro-channel design guidelines suggested in Chapter 4 which considered the manufacturability of the hydroforming process, a set of micro-channel geometries was selected and modeled using an FEA tool (MSC.Marc). Since the pressure welding of thin SS304 plates could only be obtained at elevated temperature levels, additional bulge tests were carried out to obtain the material properties of the thin SS304 blanks at the elevated temperatures (150 and 300°C). The material flow curve obtained at 150°C was used as the material model in the FE simulation to illustrate the more challenging (i.e., harder to form and weld) problem.

The threshold reduction of 55% was used as the bonding criteria in the simulation. This value was selected based on the warm pressure welding results of SS304 blanks as discussed in Chapter 5. A 10 x 10 mm plate size was selected for the demonstration purpose of the process producibility. Micro-channel arrays of 0.5 x 0.5 mm in channel width (W) and channel height (H) with the parallel flow filed configuration were modeled in the FE tool. The channel valley was modeled using the hemispherical shape with a radius of 0.25 mm, and served as indenters for the welding purpose. Draft angle of zero degree (straight wall channel) was also selected to maximize the cross-sectional area, and thus, minimize the pressure drop across the plate.

The FE models were used to characterize process parameters, specifically, the pressure and the die velocity profiles. Three different pressure and die velocity profiles were used in a DOE matrix, resulting in a total of nine simulation cases. Based on the simulation results, the effect of the ramp-up rate of the forming pressure was found to be insignificant on the channel hydroformability. However, this might be due to the relatively short cycle time of about 2.4 seconds that makes the differences between the three pressure profiles rather small. Nevertheless, the effect of the die velocity profile (punch stroke) was shown to have considerable impact on both the channel height and the final thickness value of the blanks. Increasing velocity profile was recommended for higher formability and bond strength.

Finally, the experimental test setup of the proposed manufacturing process was developed based on the understandings and results from the previous chapters. The results from this tooling design showed successful forming of double bipolar plates in a single-step and single-die operation, validating the conceptualized hybrid manufacturing

process to be feasible in a real production line. Unfortunately, a design modification is required in order to allow an appropriate removal of the hydroformed-bonded metal pairs from the die insert and the insert holder.

CHAPTER 7: CONCLUSIONS AND FUTURE WORK

7.1 Contributions

In this research, an innovative hybrid manufacturing process is proposed and developed for making of fuel cell bipolar plates. The premise of the proposed method is the use of hydroforming process of thin sheet metals combined with mechanical joining in a single-step and single-die operation to result in thin, lightweight, and flexible bipolar plates where internal cooling channels at the middle and flow fields on both sides are formed, eliminating further welding, assembly and sealing operations otherwise required with the existing methods. The research is aimed to address different fundamental technical and scientific issues that are relevant to the development of the proposed manufacturing process, which are: (1) Characterization of material behavior of thin sheet metals at micro/meso-scales, (2) Characterization of deformation mechanics of thin sheet metals in micro-feature fabrication under complex loading conditions, (3) Understanding of mechanical joining process, and its characterization, and (4) Development of predictive process models for evaluation of process producibility. These issues were investigated and their results were discussed in details in Chapters 3-6, respectively. The research contributions from Chapters 3-6 are summarized as follows:

In Chapter 3, a new way of categorizing the so-called “size effects” was discussed, three distinctive size effects, namely, the “grain size effect”, the “specimen

size effect”, and the “feature size effect”, were pointed out as different effects as compared to the previous studies of the size effects that usually combine the specimen and feature size effects together. Two characteristic ratios, N and M , were proposed to represent and quantify the size effects from the grain, the specimen, and the part feature. By using these N and M ratios, the study of the coupling effects between the grain, the specimen, and the feature sizes is also possible. In addition, based on the literature reviews, the critical value of N (i.e., $N_c \approx 2-4$), defined as the value of t_0/d at which the inverse effect of N on the flow stress is observed, was pointed out.

Unlike other size effect studies in the literature that usually utilized material with low strength and easy-to-reveal grain boundaries, such as Al and CuZn alloys, in this study, SS304, one of the most widely used alloys in sheet stamping, and one of the hardest alloys for grain structure analysis, was selected as the material of interest due mainly to the ultimate application in the fuel cell environment. Material grain size of the SS304 blanks was varied through heat treating process. In order to study the feature size effect on the material flow stress, five different bulge diameters ($D_c = 2.5 - 100$ mm) were used. A reliable and systematic approach for determination of the material flow curve based on the bulge test results was developed to include the effect of the die corner radius (R_d) and strain-hardening (n -value) into the calculation of the flow stress. An iterative computation loop was required to identify the n -value that best describes the material response.

The calculation results of the flow curves for different material grain sizes (d) and bulge diameters (D_c) clearly revealed the effects of the grain and feature sizes. While the grain size effect observed in this study simply agreed with the Hall-Petch

relation, the feature size effect, on the other hand, disclosed an interesting phenomenon where an inverse effect of the feature size on the flow stress was observed at the M values (i.e., $M = D_c/t_0$) between 100 and 200. For $M > 200$, the results in this study agreed well with the one reported by Michel and Picart [Michel, 2003] in their bulge testing of CuZn36 sheets; that is the material flow stress decreases with decreasing bulge diameter. However, up to now the effect of the feature size below M value of 100 has not been reported in any open literature. This observed phenomenon would play an important role in material modeling for the eventual numerical study of the microforming processes since each side of this critical M value would require a correlation between the material flow stress and the M value separately.

As a result, in this study, two material models were proposed to explain the phenomena that were observed on both sides of the critical M value. On the right hand side (i.e., $M > 200$), a qualitative material model was put forward to explain the decrease in flow stress with decreasing M value using the ratio between the grain boundary length and the volume (GB_L/Volume) as the material strength index (i.e., the higher the ratio, the stronger the material). On the left hand side (i.e., $M < 100$), a quantitative material model was proposed by relating the characteristic parameters of the size effects (N and M) as well as the strain-hardening exponent (n) to the material flow stress (σ_f) based on the Hall-Petch relation, the Hill's theory, and the Power law, yielding the correlation as shown in equation (3-15). Finally, this equation (3-15) was used to predict the material flow curves that were obtained from the bulge test results conducted in this study as well as in the literature by Michel [Michel, 2003]. The results showed good comparison with the experiments, and thus, it is reasonable to state that equation (3-15) represents a

legitimate correlation between N , M , n , and σ_f . Nonetheless, the material constants that are associated with equation (3-15), i.e., a , b , c , and n , will need to be identified based on a set of material testing before it can be used to predict the flow curve of the same material within the similar range of the N and M values that the material testing is conducted.

In Chapter 4, the focus of the study was placed on the manufacturability of the micro-feature arrays on thin SS304 by using internal fluid pressure. The effects of the grain size, the channel geometries, and the forming pressure on the channel formability (i.e., channel height) were investigated. Based on the experimental results of the micro-channel hydroforming using different channel geometries, the effect of the channel width (W) was pointed out as the dominating dimension that influence the maximum attainable channel height; and thus, the aspect ratio. The effect of the channel spacing (i.e., infinite spacing in the case of 1-channel die and 0.82 mm in the case of 3-channel die) was clearly shown on the channel height when comparing the two specimens formed at the same pressure from the 1-channel and 3-channel dies; that is, higher channel height was obtained in the case of 1-channel die because of less constrain on the material flow. On the other hand, the effect of the grain size ($d = 9.3 - 17.0 \mu\text{m}$) on the channel formability was found to be inconclusive in this study due to the unclear trend that was observed. Finally, higher channel height could be obtained when higher forming pressure was applied as expected.

The channel profiles from the experiments were then used for comparisons with the results from the simulations that used the material flow curves and model that were obtained and proposed in Chapter 3. The result comparisons showed poor prediction of

the channel formability based on all the material flow curves obtained from the bulge tests and the proposed model. All of the material flow curves over-predicted the channel height measured from the experiments. Nonetheless, the proposed material model provided better predictions when compared to the material flow curves obtained from the bulge tests, except for the case of $D_c = 2.5$ mm. The over-predictions of the channel height may come from the large difference between the size of the smallest bulge diameter (2.5 mm) and the channel width (0.5 mm), which in turn, causing the errors during the determination of the material constants in the proposed model. As a result, these material constants should be calculated based on the bulge test data from the bulge diameters that are in the similar range with the channel size (0.5 mm).

In the second part of the chapter, a parametric study was conducted to study the effect of different channel geometries as well as the material response (n -value) on the overall channel formability. The studied parameters include channel width (W), draft angle (α), die corner radius (R_d), channel spacing (W_{int}), channel number, and strain-hardening exponent (n). The maximum aspect ratio (AR) was used as the measure of the channel formability, and defined as the ratio between channel height (h) and channel width (W) at the 25% thinning of the blank.

The results from the parametric study showed that higher AR could be obtained when smaller channel width (W) was used. This is due to the fact that when the simulation was stopped at the 25% thinning, the similar stretching/thinning profile would be expected at the die corner radius area for all channel width sizes (i.e., die corner radius was fixed at 0.125 mm). Therefore, the wider channels (higher W value) would yield a smaller AR value. In addition, a significant increase in forming pressure was observed

when attempting to form small channel width (W). The increase in die corner radius (R_d) also leads to higher AR. The draft angle, on the other hand, showed only a slight impact on the channel formability, and thus, should be made as small as possible to maximize the cross-sectional area. By increasing channel spacing (W_{int}) and using less number of channels, the maximum aspect ratio was also shown to increase, but both are also not desirable from the performance stand point. The material with lower n -value (i.e., stronger material) requires higher pressure to form as expected. The effects of W , α , and R_d on the channel formability are rather consistent for all n -values used in this study (i.e., $n = 0.12 - 0.60$), except when $W/t_0 = 2.5$ or smaller where the effect of W is the dominant variable. The results from the parametric study could be used as the design guidelines for micro-channel geometries, considering from the manufacturing point of view. Nevertheless, the final design of the micro-channel arrays would need to be considered not only from the manufacturing point of view, but also the performance issue in order to obtain such a design that would meet the performance requirements but still within the manufacturing limitations.

In Chapter 5, the pressure welding process, one of the oldest welding techniques, was revisited and investigated for its potential use in the hybrid process to bond two thin sheet metals (i.e., stainless steel and nickel). To gain a full understanding of the process, different process conditions and parameters were studied which include the surface conditions (wet, dry, and brushed), the material type and thickness, the indenter size, the welding pressure and temperature, and the microstructure analysis of the weld region.

The results from the investigations showed that it is possible to bond thin blanks of aluminum with the present of fluid media (water) at a room temperature. However,

under this condition, higher welding pressure would be required, while relatively lower bond strength should be expected as compared to the dry and brushed surface conditions. The material with higher yield strength was shown to require higher pressure to initiate the bond. The initial thickness of the blanks was also found to be a crucial factor that directly affects the minimum welding pressure. Thinner blanks were shown to require higher welding pressure than thicker ones or in some cases the bond could not be formed at all when the thickness was reduced below 100 micrometers (e.g., Ni200 with initial thickness of 51 micrometers). As for stainless steel 304, the specimens could not be bonded at a room temperature even at a very high level of welding pressure. In order to bond SS304 and Ni200 with thickness below 100 micrometers, heating of the die and the specimen blanks was required prior to the welding. Successful bonds between SS304 to SS304 blanks and Ni200 to Ni200 blanks with initial thickness of 51 micrometers were obtained at both 150 and 300°C.

To quantify the bond quality, the bonded specimens were tested under both shear and normal loading to measure the bond strength. The bond strength was found to be enhanced by scratch brushing of the surfaces or by increasing the welding temperature. Increasing welding pressure was also shown to improve the bond strength, however, there exists an optimal value of the welding pressure (i.e., % deformation) after which the bond strength would decrease with further increase in the welding pressure. The effect of the indenter size was shown to have a slight effect on the welding pressure.

Finally, the mechanism of the bond formation at the cold condition was shown to agree with the *film theory* as proposed by Bay and Zhang [Bay, 1986; Zhang, 1996] which states that in order to create a bond between the two blanks, it is imperative that

the contaminant layers at the contact surfaces are fractured, and the underlying base material is extruded through the cracks of these broken layers. On the other hand, in the case of warm pressure welding, localized diffusion along the weld line was observed. Therefore, in the development of the hybrid process, bonding of thin stainless steel or nickel blanks would require both pressure and heat.

Finally, Chapter 6 studied the combined hybrid process both numerically and experimentally. The predictive process models were developed for rapid evaluation of process producibility and characterization of process parameters, such as forming pressure and die velocity profiles, to improve the formability and bond strength. Since the welding of thin SS304 could only be achieved at elevated temperature, a warm hydraulic bulge test was developed in order to obtain the material properties at the elevated temperature levels. This material data was used in the FE models of the hybrid process. The FEA results showed that the ramp-up profile of the pressure and the increasing die velocity profile were suitable for the hybrid process to obtain the desired channel geometries and the adequate bond strength (i.e., % deformation).

Based on these FEA results, a set of experimental tooling was developed and tested. The experimental results showed successful forming of double bipolar plates by using pure compressive loading (i.e., no pump) that was generated by a stamping press. However, due to a minor design mistake with this tooling, the double bipolar plates could not be removed from the die assembly without damaging the bond between the two blanks. Design recommendation to overcome this problem was given at the end of the chapter. Nonetheless, the simulation and experimental results showed in this chapter have reinforced the potential of the proposed hybrid manufacturing process as an

alternative fabrication process for thin metallic double bipolar plates.

7.2 Recommendation for Future Work

The results showed the feasibility of the proposed hybrid manufacturing process for fabrication of the double bipolar plates from initially flat thin stainless steel sheets in a single-die and single-step operation. In the future, to increase the accuracy of the predictive process models and to bring this process to the full implementation, following research tasks are recommended:

Task 1: Improvement on material modeling considering both size and temperature effects

Based on the results in Chapter 4, all material flow curves from the bulge tests and the proposed model still over-predicted the channel height in the simulations. Therefore, the material properties that obtained from the bulge tests at the macro/meso-scale may not provide the most accurate material data for the FEA. Since the top-down approach does not seem to fulfill the goal of the study, in the future a bottom-up approach should be considered for obtaining the more accurate material data. For example, one of the reliable and relatively simple material testing methods is the hardness test. With the advancement in the development of the micro-hardness tester and nano-indenter machine, perhaps we could relate the material data that will be obtained from these tests at the micro/nano-scales to the meso/micro-forming processes, such as the one in this study. In addition, since the bonding of the thin blanks is only successful at elevated temperatures, the material properties that will be used in the FE models should also include the effect of the temperature on the material response.

Task 2: Improvement on design guidelines of micro-channel arrays

Both manufacturing and performance aspects should be considered together when designing the final geometry of the bipolar plates. In this study, only the manufacturing aspect was considered. In the future, the performance aspect should also be considered simultaneously. This can be done by the use of computational fluid dynamic (CFD) simulations to predict the flow rate and pressure drop for different designs of micro-channel arrays and flow field configurations.

Task 3: Improvement on hybrid process design for mass production

With the current hybrid process design, the hydroformed and bonded double bipolar plates could not be removed successfully. Thus, a new tooling design is required to overcome this problem. There are also other concerns about the process design that has to be carefully addressed before this process can be used for a large-scale production. One of them concerns the handling and removing of the plates, especially after the double bipolar plates are fully formed and bonded. Since the process involves heating of the blanks for bonding purpose and hot fluid media for hydroforming, the human interaction with the process should be kept at the minimum level. Therefore, it is unavoidable that a large number of automations would be required for this process, especially for the mass production scale.

Task 4: Performance test of double bipolar plates

Finally, without the performance test of the double bipolar plates that will be produced by the proposed hybrid manufacturing process, all of the claims in terms of the

superiority of the proposed process, such as consistent contact resistance, low dimensional variations, etc., would still be questionable when compare to other types of bipolar plates, or to the same type (metallic) of bipolar plates that are fabricated by other manufacturing processes (e.g., stamping, machining, etc.). Thus, the performance test is highly critical to justify the potential use of this proposed manufacturing process.

BIBLIOGRAPHY

1. M. Abdelhamid, Y. Mikhail, (2002) “Stainless Steel as a Bipolar Plate Material in PEM Fuel Cell Environments: Stability Issues”, Proc. Of Annual Conf. American Institute of Chemical Eng., March 13, New Orleans, LA.
2. J.P. Allen, (2000), “Bipolar Separator and Current Collector Design and Manufacture”, 2000 Fuel Cell Seminar Abstracts, pp 55-58.
3. J.P. Allen, et al., (2004), “Nested stamped sheet metal plates to make an internal chamber”, US Patent # 6,777,126.
4. M.P. Allen, (2004), “Introduction to Molecular Dynamics Simulation”, NIC Series, v. 23, ISBN 3-00-012641-4, pp. 1-28, www.fz-juelich.de/nic-series/volume23.
5. R.W. Armstrong, (1961), “On Size Effects in Polycrystal Plasticity”, Journal of the Mechanics and Physics of Solids, 9, pp. 196-199.
6. R.W. Armstrong, (1983), “The Yield and Flow Stress Dependence on Polycrystal Grain Size”, in Yield, Flow and Fracture of Polycrystals, T.N. Baker, Ed. London: Applied Science Publishers, pp. 1-31.
7. R. Bar-On, R. Kirchain, R. Roth, (2002), “Technical cost analysis for PEM fuel cells”, Journal of Power Sources, v. 109, n. 1, Jun 15, pp. 71-75.
8. N. Bay, (1986), “Cold Welding: Part 1. Characteristics, Bonding Mechanisms, Bond Strength”, Metal Construction Journal, v. 18, n. 6, pp. 369-372.

9. T. Bessman, et al., (2003), "Optimization of a carbon composite bipolar plate for PEM fuel cells", Materials Research Society Symposium - Proceedings, v. 756, pp. 415-422.
10. R.H. Blunk, D.J. Lisi, Y.E. Yoo, C.L. Tucker, (2003), "Enhanced conductivity of fuel cell plates through controlled fiber orientation", AIChE Journal, v. 49, pp. 18-29.
11. J. Bohm, A. Schubert, T. Otto, T. Burkhardt, (2001), "Micro-metalforming with silicon dies", Microsystem Technologies, v. 7, n.4, pp. 191-195.
12. M.P. Brady, B. Yang, H. Wang, J.A. Turner, K.L. More, M. Wilson, F. Garzon, (2006), "Formation of protective nitride surfaces for PEM fuel cell metallic bipolar plates", JOM, v. 58, n. 8, Aug. 2006, pp. 50-57.
13. K. Butcher, et al., (2002), "Scale-up of Carbon/Carbon Composite Bipolar Plates", Proc. of Annual Conf. American Institute of Chemical Eng., March 13, New Orleans, LA.
14. J. Cao, et al., (2004), "Microforming – Experimental Investigation of the Extrusion Process for Micropins and its Numerical Simulation Using RKEM", ASME, v. 126, Nov.
15. S.W. Cha, R. O'Hayre, Y. Saito, F.B. Prinz, (2004), "The scaling behavior of flow patterns: a model investigation", Journal of Power Sources, v. 134, pp. 57-71.
16. E.A. Cho, U.-S. Jeon, H.Y. Ha, S.-A. Hong, I.-H. Oh, (2004), "Characteristics of composite bipolar plates for polymer electrolyte membrane fuel cells", Journal of Power Sources, v. 125, pp. 178-182.
17. J. Chakrabarty, J.M. Alexander, (1970), "Hydrostatic Bulging of Circular Diaphragms", Journal of Strain Analysis, v. 5, issue 3, pp. 155-161.
18. N. Cunningham, et al., (2002), "New materials and procedures to protect metallic PEM fuel cell bipolar plates", Journal of the Electrochemical Society, v. 149, n. 7, July, pp. A905-A911.

19. B. Cunningham, D.G. Baird, (2006), "The development of economical bipolar plates for fuel cells", *Journal of Materials Chemistry*, v. 16, pp. 4385-4388.
20. J.A. Donelan, (1959), "Industrial practice in cold pressure welding", *British Welding Journal*, Jan. 1959, pp.5-12.
21. D. Dudderar, F.B. Koch, E.M. Doerries, (1977), "Measurement of the shapes of foil bulge-test samples", *Experimental Mechanics*, v. 17, issue 4, pp. 133-140.
22. U. Engel, R. Eckstein, (2002), "Microforming – from basics to its realization", *Journal of Materials Processing Technology*, v. 125-126, pp.35-44.
23. U. Engel, E. Egerer, (2003), "Basic research on cold and warm forging of microparts", *Key Engineering Material*, v. 233-236, pp. 449-456.
24. J.P. Feser, A.K. Prasad, S.G. Advani, (2006), "On the relative influence of convection in serpentine flow fields of PEM fuel cells", *Journal of Power Sources*, v. 161, pp. 404-412.
25. N. Garland, (2002), "Stack components- materials and manufacturing", DOE Presentation, www.nerl.doe.gov.
26. M. Geiger, A. MeBner, U. Engel, (1997), "Production of microparts-size effects in bulk metal forming, similarity theory", *Product. Eng.*, v. 4, n.1, pp. 55-58.
27. M. Geiger, E. Egerer, U. Engel, (2001), "Cross Transport in a Multi-Station Former for Microparts", *Production Engineering*, pp. 101-104.
28. M. Geiger, M. Kleiner, R. Eckstein, N. Tiesler, U. Engel, (2001), "Microforming", *Annals of CIRP*, v. 50, n.2, Keynote paper, pp. 445-462.
29. L. Gladczyk, C. Joshi, A. Patel, J. Gurheen, Jim; Z. Iqbal, M. Sosnowski, (2003), "Corrosion-resistant tantalum coatings for PEM fuel cell bipolar plates", *Materials Research Society Symposium - Proceedings*, v. 756, pp. 423-428.

30. G. Gutscher, H. Wu, G. Ngaile, T. Altan, (2004), "Determination of flow stress for sheet metal forming using the viscous pressure bulge (VPB) test", *Journal of Materials Processing Technology*, v. 146, pp. 1-7.
31. E.O. Hall, (1951), "Deformation and Ageing of Mild Steel", *Physical Society – Proc.*,v. 64, pp. 747-753.
32. N. Hansen, (1977), "The Effect of Grain Size and Strain on the Tensile Flow Stress of Aluminium at Room Temperature", *Acta Metallurgica*, v. 25, pp. 863-869.
33. A. Heinzl, F. Mahlendorf, O. Niemzig, C. Kreuz, (2004), "Injection moulded low cost bipolar plates for PEM fuel cells", *Journal of Power Sources*, v. 131, pp. 35-40.
34. A. Hermann, T. Chaudhuri, P. Spagnol, (2005), "Bipolar plate for PEM fuel cells: A review", *Int. Journal of Hydrogen Energy*, v. 30, pp. 1297-1302.
35. R. Hill, (1950), "A theory of the plastic bulging of a metal diaphragm by lateral pressure", *Philosophical Magazine*, series 7, vol. 41, 1113-1142.
36. M.F. Horstemeyer, M.I. Baskes, S.J. Plimpton, (2001), "Computational nanoscale plasticity simulations using embedded atom potentials", *Theoretical and applied fracture mechanics*, v. 37, pp. 49-98.
37. K. Jayakumar, S. Pandiyan, N. Rajalakshmi, K.S. Dhathathreyan, (2006), "Cost-benefit analysis of commercial bipolar plates for PEMFC's", *Journal of Power Sources*, v. 161, pp. 454-459.
38. B.Y. Joo, S.I. Oh, Y.K. Son, (2004), "Forming of micro channels with ultra thin metal foils", *CIRP Ann* 53 (1), pp. 243-246.
39. R. Kals, F. Vollertsen, M. Geiger, (1996), "Scaling effects in sheet metal forming", *Proceedings of the Fourth International Conference on Sheet Metal (SheMet)*, v. 2, Enschede, pp. 65-75.
40. R.T. A. Kals, (1999), "Fundamentals on the Miniaturization of Sheet Metal Working Processes", *Meisenbach*.

41. T.A. Kals, R. Eckstein, (2000), "Miniaturization in sheet metal working", *Journal of Material sProcessing Technology*, v. 103, pp. 95-101.
42. M. Karplus, (2003), "Molecular Dynamics of Biological Macromolecules: A Brief History and Perspective", *Biopolymers*, v. 68, pp. 350-358.
43. G. Kim, M. Koç, J. Ni, (2007), "Modeling of the Size Effects on the Behavior of Metals in Micro-scale Deformation Processes", *Journal of Manufacturing Science and Engineering*, v. 129, pp. 470-476.
44. M. Koç, S. Mahabunphachai, (2007), "Feasibility investigations on a novel micro-manufacturing process for fabrication of fuel cell bipolar plates: Internal pressure-assisted embossing of micro-channels with in-die mechanical bonding", *Journal of Power Sources*, v. 172, n. 2, 25 Oct. 2007, pp. 725-33
45. H. Kuan, C.M. Ma, K. Chen, S. Chen, (2004), "Preparation, electrical, mechanical and thermal properties of composite bipolar plate for a fuel cell", *Journal of Power Sources*, v. 134, pp. 7-17.
46. R.G. Kumar, G. Reddy, (2003), "Effect of channel dimensions and shape in the flow-field distributor on the performance of polymer electrolyte membrane fuel cells", *Journal of Power Sources*, v. 113, pp. 11-18.
47. Y.H. Lai, D. Miller, C. Ji, T. Trabold, (2004), "Stack compression pf PEM fuel cells", *Proc. 2nd Int'l Conf. on Fuel Cell Science, Eng. and Tech.*
48. Shuo-Jen Lee, Yu-Pang Chen, Ching-Han Huang, (2005), "Electroforming of metallic bipolar plates with micro-featured flow field", *Journal of Power Sources*, v. 145, pp. 369-375.
49. W. Lehrheuer, (1993), "High-Temperature Solid-State Welding", *ASM Handbook*, v. 6, *Welding, Brazing, and Soldering*, Dec., 1993, pp. 297-299.
50. M.C. Li, C.L. Zeng, S.Z. Luo, J.N. Shen, H.C. Lin, C.N. Cao, (2003), "Electrochemical corrosion characteristics of type 316 stainless steel in simulated

- anode environment for PEMFC”, *Electrochimica Acta*, v. 48, n. 12, May 30, pp. 1735-1741.
51. X. Li, I. Sabir, (2005), “Review of bipolar plates in PEM fuel cells: Flow-field designs”, *International Journal of Hydrogen Energy*, v. 30, pp. 359-371.
52. X. Li, I. Sabir, J. Park, (2007), “A flow channel design procedure for PEM fuel cells with effective water removal”, *Journal of Power Sources*, v. 163, pp. 933-942.
53. Y. Li, Z. Du, Y. Tao, (2003), “Interfacial bonding state on different metals Ag, Ni in cold pressure welding”, *Transactions of Nonferrous Metals Society of China (English Edition)*, v. 13, n. 2, Apr., 2003, pp. 276-279.
54. T.E. Lipman, J.L. Edwards, D. M. Kammen, (2004), “Fuel cell system economics: comparing the costs of generating power with stationary and motor vehicle PEM fuel cell systems”, *Energy Policy*, v. 32, pp.101-125.
55. N.D. Lukaschkin, A.P. Borissow, (1996), “Interface surface behaviour in the upsetting of sandwich metal sheets”, *Journal of Materials Processing Technology*, v. 61, pp. 292-297.
56. H.R. Madaah-Hosseini, A.H. Kokabi, (2002), “Cold roll bonding of 5754-aluminum strips”, *Materials Science and Engineering A335*, pp. 186-190.
57. S. Mahabunphachai, M. Koç, (2008), “Fabrication of micro-channel arrays on thin metallic sheet using internal fluid pressure: investigations on size effects and development of design guidelines”, *Journal of Power Sources*, v. 175, n. 1, 3 Jan. 2008, pp. 363-371.
58. S. Mahabunphachai, M. Koç, (2008), “Investigation of size effects on material behavior of thin sheet metals using hydraulic bulge testing at micro/meso-scales”, *Journal of Machine Tools and Manufacture*, accepted: ref. no. IJMACTOOL-D-07-00344R2.

59. V. Mehta, J.S. Cooper, (2003), "Review and analysis of PEM fuel cell design and manufacturing", *Journal of Power Sources*, v. 114, n. 1, Feb 25, pp. 32-53.
60. S. Mepsted, (2002), "Cold pressure welding", *Wire Industry*, June 2002, pp. 329-332.
61. J.F. Michel, P. Picart, (2003), "Size effects on the constitutive behaviour for brass in sheet metal forming", *Journal of Materials Processing Technology*, v. 141, pp. 439-446.
62. E. Middelma, W. Kout, B. Vogelaar, J. Lenssen, E. De Waal, (2003), "Bipolar plates for PEM fuel cells", *Journal of Power Sources*, v. 118, n. 1-2, May 25, pp. 44-46.
63. S. Miyazaki, H. Fujita, H. Hiraoka, (1979), "Effect of specimen size on the flow stress of rod specimens of polycrystalline Cu-Al alloy", *Scripta Metallurgica*, v. 13 pp. 447-449.
64. M.H. Oh, Y.S. Yoon, S.G. Park, (2004), "The electrical and physical properties of alternative material bipolar plate for PEM fuel cell system", *Electrochimica Acta*, v. 50, pp. 777-780.
65. R.M. Onyancha, B.L. Kinsey, (2006), "Investigation of size effects on process models for plane strain microbending", *Proceedings of the International Conference on Manufacturing Science and Engineering (MSEC)*, Oct. 8-11, 2006, Ypsilanti, MI.
66. T. Otto, A. Schubert, J. Bohm, T. Gessner, (2000), "Fabrication of micro optical components by high precision embossing", *Proceedings of SPIE the International Society for Optical Engineering*, v. 4179, pp. 96-106.
67. R.C. Pendrous, A.N. Bramley, G. Pollard, (1984), "Cold roll and indent welding of some metals", *The Metals Society*, v. 11, pp. 280-289.
68. N.J. Petch, (1953), "Cleavage Strength of Polycrystals," *Iron and Steel Institute*, v. 174, May, pp. 25-28.

69. L.V. Raulea, A.M Goijaerts, L.E. Govaert, F.P.T. Baaijens, (2001), "Size effects in the processing of thin metals", *Journal of Materials Processing Technology*, v. 115, pp. 44-48.
70. Y. Saotome, I. Akihisa, (1994), "Superplastic Micro-Forming of Microstructures", *Proc. 7th IEEE Workshop on Micro Electro Mechanical Systems*, pp. 343-347.
71. Y. Saotome, Y. Kaname, K. Hiroshi, (2001), "Microdeep drawability of very thin sheet steels", *Journal of Materials Processing Technology*, v. 113, pp. 641-647.
72. Y. Saotome, et al., (2002), "The micro-nanoformability of Pt-based metallic glass and the nanoforming of three-Dimensional structures", *Intermetallics*, v. 10, pp. 1241-1247.
73. J. Scholta, et al., (1999), "Investigations on novel low-cost graphite composite bipolar plates", *Journal of Power Sources*, v. 84, n. 2, Dec, pp. 231-234.
74. K. Sim, Y. Lee, (2005), "A bonding map for Cu and Al plates by pressure welding at cold and warm temperatures", *Materials Science Forum*, v. 475-479, pp. 2667-2670.
75. A.B. Sowter, (1949), "Materials joined by new cold welding process", *The Welding Journal*, Feb., 1949, pp. 149-152.
76. K. Thomas, M. Petri, (1993), "Cold Welding", *ASM Handbook*, 10th Ed., Welding, Brazing and Soldering, v. 6, pp. 307-310.
77. N. Tiesler, U. Engel, (2000), "Microforming-Effects of Miniaturization", presented at *Proceedings of the Eighth International Conference on Metal Forming*, Balkema, Rotterdam.
78. A.A. Tseng, (1990), "Material characterization and finite element simulation for forming miniature metal parts", *Finite Elements in Analysis and Design*, v. 6, pp. 251-265.
79. L. R. Vaidyanath, M. G. Nicholas, D. R. Milner, (1959), "Pressure Welding by Rolling", *British Welding Journal*, v. 6, pp. 13-28.

80. F. Vollertsen, Z. Hu, H. Schulze Niehoff, C. Theiler, (2004), "State of the art in micro forming and investigations into micro deep drawing", *Journal of Materials Processing Technology*, v. 151, pp. 70-79.
81. H. Wang, M.A. Sweikart, J.A. Turner, (2003), "Stainless steel as bipolar plate material for polymer electrolyte membrane fuel cells", *Journal of Power Sources*, v. 115, n. 2, Apr 10, pp. 243-251.
82. H. Weule, (1995), "Neue Antriebe und Energieträger- Chancen für den Automobilbau", 16. Internationales Wiener Motorensymposium, Mar.
83. J.D. Williams, B. Crossland, (1976), "Part 1 Cold pressure welding", *I Mech E*, pp. 65-67.
84. J. Wind, R. Spah, W. Kaiser, G. Boehm, (2002), "Metallic bipolar plates for PEM fuel cells", *Journal of Power Sources*, v 105, 2002, pp. 256-260.
85. N. Witulski, H. Justinger, G. Hirt, (2004), "Validation of FEM-Simulation for Micro Deep Drawing Process Modeling", NUMIFORM.
86. P.K. Wright, D.A. Snow, C.K. Tay, (1978), "Interfacial conditions and bond strength in cold pressure welding by rolling", *Metals Technology*, v. 5, n. 1, Jan, pp. 24-31.
87. W. Zhang, N. Bay, (1996), "A numerical model for cold welding of metals", *CIRP Annals-Manufacturing Technology*, v. 45, n.1, pp. 215-220.